REFERENCE ONLY

UNIVERSITY OF LONDON THESIS

Degree PhD Year 2006 Name of Author K. M. KNIGHT

COPYRIGHT
This is a thesis accepted for a Higher Degree of the University of London. It is an unpublished typescript and the copyright is held by the author. All persons consulting the thesis must read and abide by the Copyright Declaration below.

COPYRIGHT DECLARATION
I recognise that the copyright of the above-described thesis rests with the author and that no quotation from it or information derived from it may be published without the prior written consent of the author.

LOAN
Theses may not be lent to individuals, but the University Library may lend a copy to approved libraries within the United Kingdom, for consultation solely on the premises of those libraries. Application should be made to: The Theses Section, University of London Library, Senate House, Malet Street, London WC1E 7HU.

REPRODUCTON
University of London theses may not be reproduced without explicit written permission from the University of London Library. Enquiries should be addressed to the Theses Section of the Library. Regulations concerning reproduction vary according to the date of acceptance of the thesis and are listed below as guidelines.

A. Before 1962. Permission granted only upon the prior written consent of the author. (The University Library will provide addresses where possible).

B. 1962 - 1974. In many cases the author has agreed to permit copying upon completion of a Copyright Declaration.

C. 1975 - 1988. Most theses may be copied upon completion of a Copyright Declaration.

D. 1989 onwards. Most theses may be copied.

This thesis comes within category D.

☑ This copy has been deposited in the Library of UCL

☐ This copy has been deposited in the University of London Library, Senate House, Malet Street, London WC1E 7HU.

P:\Office\Standard forms\Copyright - thesis.doc

A Surfactantless Emulsion as a Model for the Liquid–Liquid Interface

Katherine Mary Knight

A thesis submitted in
partial fulfilment for
the degree of
Doctor of Philosophy

University College London
University of London
December 2005

ProQuest LLC
789 East Eisenhower Parkway
P.O. Box 1346
Ann Arbor, MI 48106-1346

For my

Mum and Dad

Acknowledgments

Firstly I'd like to thank Dr. Daren Caruana for all his support and encouragement over the last 4 years. He has so much enthusiasm for his work that sometimes it's hard not to admire and respect him. Without his endless patience I don't think this would have ever been written and I cannot thank him enough for always being there to help.

I would also like to thank Richard Heenan at ISIS for his help analysing the SANS data and always being ready and able to answer my questions about neutrons. The day he told me we might actually have a 'wiggle' will probably be one of the happiest days of my PhD.

I'd also like to say a big thank you to Dick Waymark for his amazing electronic skills, and to the rest of UCL technical support. Thanks must also go to Jim Stevenson in the technical workshop, and to John Hughes for the consistently perfect glassware he made, especially considering the quality of some of my drawings.

I was very lucky to be able to visit the Helsinki University of Technology in Finland during my PhD and I would like to thank Köpi and Anna Kontturi for making this possible. Also thank you to Christoffer Johans for teaching me all about potential determining ions and helping with the electrodeposition, and to Lasse Murtomäki, Mari Aaltonen and Kirsi Mansikkamäki, for making my stay so enjoyable.

I must also thank the wonderful people that I have worked with in G16 over the past 4 years: Emina Hadzifejzovic for supplying me with pretzels and fruit and never letting the lab get too quiet, thank you for being such a dear friend; Jorge Sanchez for working on the emulsions with me, especially the D11 experiment, and renewing my faith in the deposition experiments, seeing the pictures of his particles was a day I'll never forget. Also thank you to Bushra Chaudhry, Zeshan Iqbal, Jun Yao, Estelle

Bernard and Camilla Forssten, all of whom I've had the pleasure of working with at some point during my time at UCL.

I would like to thank the following as well for their help along the way: David Williams at Unipath, Dame Julia Higgins and Imperial Analytical Services. Kevin Reeves and Andrew Wills at UCL, Bruno Demé at the ILL, Steven King at ISIS, the Beckmann Coulter Particle Characterisation Group, Jonathon Lovick in Chemical Engineering and Supti Sarkar in Biochemical Engineering at UCL, and for funding I would like to thank the EPSRC, RAL and ILL.

A special thank you must go to my friends and family; in particular to my parents for all their unconditional love and support. I can never thank you enough for all you have done for me in my life and so I am dedicating my thesis to you both.

I would also like to thank Sarah Robbie, Julia Tomlinson, Sarah Chinchen and Annabel Rein for being such fantastic friends and always being there for me.

Finally I thank my wonderful husband Russell for all his love and showing me that I am capable doing anything, a little bit of this is also dedicated to you.

A Surfactantless Emulsion as a Model for the Liquid–Liquid Interface

Katherine Mary Knight
University College London, 2005

Abstract

An electrochemically polarised liquid–liquid interface in the form of a surfactantless oil–in–water emulsion has been developed, and its creation, stabilisation and use as a model liquid–liquid system for structural characterisation using Small Angle Neutron Scattering (SANS) are described.

The emulsion, composed of 1,2–dichloroethane (DCE)–in–D_2O, was created using a condensation method and the two main processes of destabilisation, sedimentation and coalescence, were minimised using density–matching and electrochemistry. The stabilised emulsion interface was then studied with SANS, using the D11 and D22 diffractometers at the ILL and LOQ at ISIS. This was to determine structural information regarding a layer of adsorbed Bovine Serum Albumin (BSA) protein at the interface with and without stabilising salts and the only analysable results were obtained using D11, due to the lower *Q*–range accessible. The BSA layer thickness was determined to be 40 and 48 Å for emulsions with and without salts respectively, and this was comparable with the literature thickness of 40 Å.

Another use for the surfactantless emulsion would be for electrodeless electrodeposition of metals at the interface, utilising the interfacial potential, and preliminary experiments were carried out using both oil–in–water and water–in–oil emulsions.

Table of Contents

1 Introduction

2 Experimental Materials, Methods and Equipment

3 Creation and Characterisation of an Oil–in–Water Emulsion

4 Stabilisation of an Oil–in–Water Emulsion

5 Small Angle Neutron Scattering Analysis of Protein Adsorption at the Oil–in–Water Emulsion Interface

6 Characterisation and Stabilisation of a Water–in–Oil Emulsion and its Comparison with an Oil–in–Water System

7 Concluding Remarks

Table of Figures

Table of Tables

Index of Abbreviations

$AgNO_3$ = Silver nitrate

BAM = Brewster Angle Microscopy

BSA = Bovine Serum Albumin

BTPPA = Bis(triphenylphosphoranylidene)ammonium

BuFc = Butylferrocene

$C_2D_4Cl_2$ = Deuterated 1,2–dichloroethane

Cl = Chloride

CV = Cyclic Voltammetry

D_2O = Deuterium oxide

DCE = 1,2–Dichloroethane

DLVO = Deryagin–Landau–Verwey–Overbeek theory

DmFc = Dimethylferrocene

EDAX = X–ray diffraction

EMXA = Electron Microscopy X–ray Analysis

Fc = Ferrocene

FFFS = Front Face Fluorescence Spectroscopy

H_2O = Water

H_2SO_4 = Sulphuric acid

ILL = Institute Laue–Langevin

ISI = Integrated Scattering Intensity

ITIES = Interface between Two Immiscible Electrolyte Solutions

LiCl = Lithium chloride

Li_2SO_4 = Lithium sulphate

LiTPFB = Lithium Tetrakis(pentafluorophenyl)borate

NaCl = Sodium chloride

NaTPB = Sodium tetraphenylborate

$(NH_4)_2PdCl_4$ = Ammonium tetrachloropalladate (II)

ORM = Optical Reflectance Measurement

QELS = Quasi–Elastic Laser Light Scattering

RDE = Rotating Disc Electrode

SANS = Small Angle Neutron Scattering

SCE = Standard Calomel Electrode

SECM = Scanning Electrochemical Microscopy

SEM = Scanning Electron Microscopy

SLD = Scattering Length Density

SSHG = Surface Second Harmonic Generation

TBuA = Tetrabutylammonium

TBuACl = Tetrabutylammonium chloride

TBuATPB = Tetrabutylammonium tetraphenylborate

TEA = Tetraethylammonium

TEACl = Tetraethylammonium chloride

TEATPB = Tetraethylammonium tetraphenylborate

THxA = Tetrahexylammonium

THpABr = Tetraheptylammonium bromide

TIRFS = Total Internal Reflection Fluorescence Spectroscopy

TIR–RLS = Total Internal–Reflected Resonance Light Scattering

TMA = Tetramethylammonium

TPAs = Tetraphenylarsonium

TPB = Tetraphenylborate

TPeA = Tetrapentylammonium

TPFB = Tetrakis(pentafluorophenyl)borate

TPrA = Tetrapropylammonium

TTF = Tetrathiafulvalene

TXACl = Tetraalkylammonium chloride

TXATPB = Tetraalkylammonium tetraphenylborate

VSFS = Vibrational Sum–Frequency Spectroscopy

Chapter 1: Introduction

1.1 The Liquid–Liquid Interface

The liquid–liquid interface with and without adsorbed protein is of central importance to many fundamental processes; for example, the cell membrane is a lipid bilayer between two aqueous liquids, with protein molecules embedded into and spanning across the layer, aiding in the transfer of chemicals into and out of the cell. This could be modelled by adsorbed proteins at an oil–water interface and investigated to gain knowledge of the molecular structure of this layer.

A possible technique that could be used to gain this structural information is that of Small Angle Neutron Scattering (SANS), which has been used successfully to look at adsorbed surfactant layers at the liquid–liquid interface, because this method overcomes some of the technical difficulties encountered using other investigative techniques. For many of the previous SANS experiments reported, surfactant–stabilised liquid–liquid emulsions were widely used and it was proposed that if a surfactantless emulsion was developed, then information could be obtained about the structure of the 'clean' interface. Investigations of protein adsorption could then also be undertaken using the surfactantless emulsion, hence preventing problems from competitive adsorption between the protein and surfactant.

In this chapter, recent advances into the study of the liquid–liquid interfacial dynamics and structure are described, as are emulsions stabilised with and without surfactants. Proteins are also introduced and a summary of relevant SANS experiments is reported.

1.1.1 Investigations into the Structure and Dynamics of the Liquid–Liquid Interface

There has been much recent interest into the investigation of the liquid–liquid interface due to the development of successful experimental surface techniques [1], that either specifically probe the interfacial molecules or have been adapted from traditional 'bulk' techniques to study the interface. Unlike the air–liquid and liquid–solid interface, the liquid–liquid interface has a buried nature and the structure and properties of the molecules at the interface are generally very different from molecules within the bulk liquids. When using 'bulk' experimental techniques, i.e. spectroscopy, to investigate the interface, both bulk and interfacial molecules are analysed but any information from the interface is overwhelmed by the information from the bulk liquid. Therefore, until recently, most of the information regarding the structure and dynamics of the liquid–liquid interface was from theoretical predictions; such as molecular dynamics computations and Monte Carlo simulations [2–20]. Monte Carlo simulations suggest that the interface is molecularly sharp with a dynamic roughness caused by thermal fluctuations, modelled as capillary waves, and these produce a finite thickness of the interface. Another suggested structure is that the interface is made up of 3 phases, where the middle phase is a mixture of molecules of the two liquids [21]. These two structures are illustrated in Figure **1.1**. Results from the theoretical simulations suggest an interfacial thickness in the order of 10 Å for the 1,2–dichloroethane (DCE)–water interface, with a molecularly sharp interface roughened by thermally excited fingerlike water structures penetrating into the oil phase [7]. These are able to form due to the inefficient packing of the DCE molecules in the vicinity of the interface, and the polarity of the liquid. The model does, however, significantly overestimate the difference in conformational population in the bulk to that found at the interface.

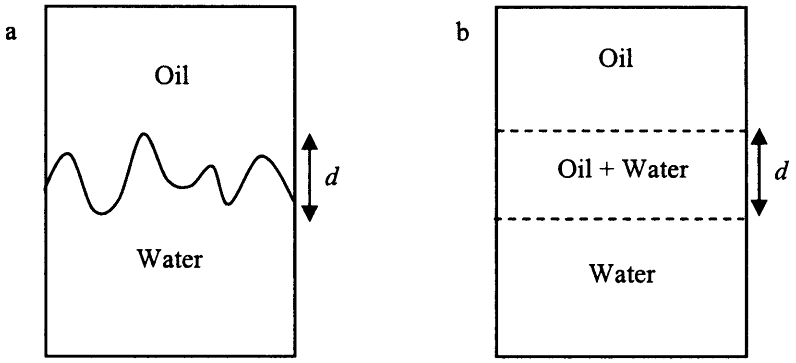

Figure 1.1: Schematic diagram showing the two main proposed molecular structures for the liquid–liquid interface; (a) where the interface is molecularly sharp with capillary wave–like distortions, and (b) where the interface is a separate 'mixing region' of the two liquids; both with a finite thickness *d*.

Recent work by Benjamin has studied the dynamics of hydrogen bonds at the interface [2] and has shown, that due to these fingerlike structures, there is a high probability of the adjacent water molecules being hydrogen–bonded, and that these interfacial hydrogen bonds have a longer lifetime, due to the strong intermolecular DCE–water interactions, than those found in the bulk liquid. Jedlovszky *et al* have reported that there are two markedly different orientations of the water molecules at the DCE–water interface [20]; a parallel alignment of the molecular plane with the interface, present over the entire interfacial surface and also in the subsurface water layer adjacent to the interface, and a perpendicular alignment of the water molecules penetrated deepest into the DCE phase, where one of the O–H bonds points straight towards the DCE layer, as also described by Benjamin [7]. The two orientations are linked via a hydrogen bond and correspond to the alignment of a hydrogen bonded pair of water molecules.

Much of the experimental work investigating the structure and dynamics of the liquid–liquid interface has used spectroscopic techniques; for example, Surface Second Harmonic Generation (SSHG) [22–26], Vibrational Sum–Frequency Spectroscopy (VSFS) [27–30], Front Face Fluorescence Spectroscopy (FFFS) [31], Reflection Spectrometry [32&33], EPR spin probe spectroscopy [34] and Total Internal Reflection Fluorescence Spectroscopy (TIRFS) [35–39]; and optical, reflection and scattering methods; e.g. Ellipsometry [40&41], Brewster Angle Microscopy (BAM) [42], Quasi–Elastic Laser Light Scattering (QELS) [43–45], Total Internal–Reflected Resonance Light Scattering (TIR–RLS) [46&47], and X–Ray [48–53] and neutron [54–67] reflectivity or scattering. Electrochemical techniques; including Voltammetry [68–73], Scanning Electrochemical Microscopy (SECM) [74] and Potentiometry [75], and Interfacial Tension measurements [76], have also been used to study charge transfer reactions at the liquid–liquid interface.

It can be seen that, due to the recent advances in technology, there are a wide range of techniques available but many of these are difficult to perform and analyse. For example, much of the experimental work on the DCE–water interface uses a continuous interface between the two liquids that is held apart by their differing densities. This is difficult to control experimentally though, due to the volatile nature of the DCE and the sometimes lengthy timescales of the experiments. There is however, a wealth of literature concerning the structure and dynamics of the liquid–liquid interface, due to the advances in technology available for use at the molecular level, and a summary of some of the recent work is presented in Table **1.1** (the literature regarding neutron scattering experiments is described in **1.3.2**).

In conclusion, the liquid–liquid interface is central to many biological processes, and knowledge of the interfacial molecular structure and bonding can give important information regarding kinetic and thermodynamic processes. Such information becoming obtainable is the thickness of the interface and how the molecules are orientated, the adsorption of molecules at the interface e.g. surfactants, proteins and electrolytes, including the effects of these adsorbed molecules on the structure and orientation of the interfacial water molecules, the interaction of the interface with the adsorbates and also of the adsorbates with each other, and the nature of the adsorbed layer. Also available, is information regarding the interface between two immiscible electrolyte solutions (ITIES), such as the interfacial potential and the interfacial dynamics including ion and electron transfer reactions.

Liquid–Liquid Interface Investigated	Technique Used	Observed Results	Ref
Cyclohexane–Water and 1–Octanol–Water	SHG with Molecular Rulers	The dipolar width across the interface, i.e. the distance needed for the dielectric environment to change between phases: >9 Å and molecularly sharp for weakly associating cyclohexane–water. For strongly associating 1–octanol–water, the interface appeared as a hydrophobic barrier between the two polar liquids, i.e. a 'mixing' region.	[23]
DCE–Water	SHG	Electrostatic coadsorption of poly–L–glutamic acid and *trans*–4–[4–(dibutylamino)styrl]–1–methylpyridinium iodide at the interface.	[24]
Heptane–Water	SHG	Structural information concerning rhodamine dyes adsorbed at the liquid–liquid interface compared with the solid–liquid interface.	[26]
Carbontetrachloride–Water	VSFS	Effect of an isolated surfactant, compared with a saturated monolayer, on the hydrogen bonding at the interface. Suggests that an accumulation of surface charge induces structural changes in the solvating water.	[28]
DCE–Water	VSFS	Evidence of a diffuse 'mixing' layer at the interface compared with the molecularly sharp CCl_4–water interfacial structure, due to the polarity of the DCE.	[29]
d_{34}–Hexadecane–D_2O	VSFS	Monolayer structure of adsorbed surfactant hexadecyltrimethylammonium bromide at the interface.	[30]
n–Hexadecane–Water	FFFS	Comparing information regarding the molecular environment of BSA in emulsions stabilised with different concentrations of Tween 20.	[31]
Dodecane–Aqueous Sulphuric Acid	Partial Reflection Spectrometry	Semi–quantitative molecular orientation analysis of the adsorption of *meso*–tetraphenylporphyrin at the interface.	[33]
Carbontetrachloride–Water	TIRFS	Molecular recognition mediated by hydrogen bonding at the interface using riboflavin in the aqueous phase with and without *N,N*–dioctadecyl–[1,3,5]triazine–2,4,6–triamine.	[35]
Heptane–Water	TIRFS	The solvation dynamics of the fluorophores 12–(9–anthroyloxy)stearic acid and 4–(9–anthroyloxy)butanoic acid at the interface. Showing that the polarity of the interface was in–between that of the bulk phases and dependent on the polarity of the fluorescence probe.	[36]
Decane–Water/D_2O	Ellipsometry	Using H_2O or D_2O as the aqueous phase, the amount of adsorption of two types of $C_nH_{2n+1}(OC_2H_4)_m$, where n and m were 12 and 5 in the oil and 18 and 50 in the water phase. Values of 1.38 and 0.93 mg m^{-2} were obtained for the organic and aqueous concentrations respectively and agree with theoretical values.	[40]
Toluene–Water	Ellipsometry	Determining the contact angles and structural information of monodisperse silica particles at the interface with good agreement with theoretical values.	[41]

Hexane–Water	BAM	Studying temperature–induced phase transitions in interfacial monolayers of octadecanol and 1,1,2,2–tetrahydroperfluorododecanol.	[42]
DCE–Water	QELS	Investigating the dynamics of the polarised interface in the presence of different concentrations of adsorbed DL–α–dipalmitoylphosphatidylcholine, and showing the behaviour to be consistent with theoretical predictions of a sharp interface.	[43]
Tetracloromethane–Water	TIR–RLS	Determination of formation constants of penicillin–berberine ion associates adsorbed at the interface.	[46]
Nitrobenzene–Water and 2–Heptanone–Water	X–Ray Reflectivity	Measurements of the 'clean' interfacial thickness; in the order of 5 and 7 Å for the nitrobenzene– and 2–heptanone–water interfaces respectively. These are shown to be consistent with theoretical values and also the interfacial sensitivity to temperature and electrolyte distribution is presented.	[49]
Hexane–Water	X–Ray Reflectivity	Showing that the adsorbed surfactants, 1–eicosanol and 1,1,2,2–tetrahydroheptadecafluorodecanol, are present in different monolayer phases depending on the surfactant concentration and system temperature.	[50]
Hexane–Water	X–Ray Scattering	Studying the size and distribution of the interfacial domains in monolayers of the surfactant $F(CF_2)_{10}(CH_2)_2OH$ adsorbed at the interface, over a range of temperatures.	[51]
Glycerol–Water	X–Ray Scattering	Measurements of the interfacial roughness were found to follow the capillary wave model, and these were unaffected by viscosity and temperature.	[52]
Laurylamine–Tetraethoxysilane	X–Ray Scattering	Describing the formation process and mesostructure ordering of silica at the interface.	[53]
Hexadecane–Water	Neutron Reflectivity	The adsorption of tetradecyltrimethylammonium bromide and Pluronic L64 was investigated, with the surfactant being seen to reside mainly in the oil phase and the polymer to adsorb on both sides of the interface.	[54]
Hexadecane–Water	Neutron Reflectivity	The interface structure was analysed with and without the block copolymer polybutadiene–poly(ethylene oxide) and the 'clean' interface was found to be rougher than that predicted by theory simulations. The polymer was then seen to segregate at the interface, forming layers 20 and 50 Å thick.	[64]
DCE–Aqueous Potassium Hydroxide	Neutron Reflectivity	The interface was determined to be smooth and 10 Å thick, in agreement with theoretical simulations.	[65]

Table 1.1: Listing some of the recent literature detailing the structure and dynamics of the liquid–liquid interface.

1.1.2 Electrochemical Potentials at the Liquid–Liquid Interface

When a salt is dissolved in a solution containing two immiscible liquids, i.e. oil (*O*) and water (*W*), an electrical potential difference is set–up across the interface when the partition equilibrium is reached. This can be measured as the *external* or *internal* potential and are termed the *Volta* or *Galvani potential* respectively [74]. The Volta potential, ψ^W, is produced by the surface charge of phase *W*, and is measured in a vacuum in the vicinity of the surface. The Galvani potential, ϕ^W, is produced in the bulk of the water phase, *W*, and is calculated from infinity in a vacuum. These two potentials are linked by the surface potential drop, χ^W, calculated from $\psi^W - \phi^W$. The difference in the Galvani potentials, $\Delta_O^W\phi = \phi^O - \phi^W$, of the two liquids is used in the study of the ITIES and is determined by the distribution of charged particles near the interface. These equilibrium potentials, which are found at reversible or non–polarisable interfaces, can then be separated into three different types according to what species can pass between the two phases.

Distribution potentials – These are potentials that arise when all the ions are able to pass from one phase to the other in an equilibrium system.

Donnan potentials – These occur when two phases contain ions, some of which can cross the interface whilst some cannot.

Nernst potentials – Similar to Donnan potentials, these occur when the transfer of ions of only one kind are allowed across.

Redox potentials – These occur when equilibrium is caused by the two solutions exchanging electrons across the interface.

It is possible to calculate the change in potential between the two phases using knowledge of the electrochemical properties of the ions used in the system. The ions dissolved in both phases have an electrochemical potential and at equilibrium, these potentials must be equal,

$$\bar{\mu}_i^O = \bar{\mu}_i^W \qquad 1.1$$

Where $\bar{\mu}_i^\alpha$ is the electrochemical potential of the ion, i, dissolved in phase α, and α is either the oil (O) or the water (W) phase. As ions are charged, the electrostatic part of this potential is separated [75] and is written as,

$$\bar{\mu}_i^\alpha = \mu_i^\alpha + \mu_i^{\alpha,el} \qquad 1.2$$

Here μ_i^α and $\mu_i^{\alpha,el}$ represent the 'chemical' and the 'electrical' energy terms respectively. As these terms cannot actually be separated into two entities, the calculation is an approximation and $\mu_i^{\alpha,el}$ can be replaced with $z_iF\phi^\alpha$. This is the work needed to bring a test particle, with a charge z_ie, in a vacuum from infinity to the inside of phase α. This charge is assumed to have no 'chemical' interaction with the phase and Equation **1.2** becomes,

$$\bar{\mu}_i^\alpha = \mu_i^\alpha + z_iF\phi^\alpha \qquad 1.3$$

The chemical potential, μ_i^{α}, is related to the standard chemical potential, $\mu_i^{\alpha,o}$, using,

$$\mu_i^{\alpha} = \mu_i^{\alpha,o} + RT \ln a_i^{\alpha} \qquad \mathbf{1.4}$$

Where R is the gas constant and T is the absolute temperature. a_i is equal to $\gamma_i c_i$; where γ_i and c_i are the activity coefficient and concentration of i, respectively.

When the two phases first come into contact, the ions are dissolved in one phase and are free to move into the other until thermodynamic equilibrium is reached, and the electrochemical potential is set–up. After this, there is no further movement of ions between the phases and there is an inhomogeneous distribution of ions in the area of the interface, causing the distribution potential. Using Equation **1.4** and the relation in Equation **1.1**, the potential difference can be determined and expressed as,

$$\Delta_O^W \phi = \frac{1}{z_i F}\left(\mu_i^{O,o} - \mu_i^{W,o}\right) + \frac{RT}{z_i F} \ln \frac{\gamma_i^O c_i^O}{\gamma_i^W c_i^W} \qquad \mathbf{1.5}$$

This shows the Galvani potential difference in terms of the chemical part of the electrochemical potential of i in oil and water. Equation **1.5** allows for the dependence of the chemical potential of the ion, i, on the concentration of the liquids and uses the standard chemical potentials of i in either phase, $\mu_i^{O,o}$ or $\mu_i^{W,o}$. The superscripts O and W refer to the oil and water phases respectively.

The Gibbs energy of transfer of the ion, *i*, from the water to the oil phase, $\Delta G_i^{W\rightarrow O,o}$, is equal to the difference in chemical potentials $\mu_i^{O,o} - \mu_i^{W,o}$. This is related to the standard ion–transfer potential $\Delta_O^W\phi_i^o$ using Equation **1.6**,

$$\Delta_O^W\phi_i^o = \frac{1}{z_iF}\Delta G_i^{W\rightarrow O,o} \qquad \mathbf{1.6}$$

and gives Equation **1.7**,

$$\Delta_O^W\phi = \Delta_O^W\phi_i^o + \frac{RT}{z_iF}\ln\frac{\gamma_i^O c_i^O}{\gamma_i^W c_i^W} \qquad \mathbf{1.7}$$

This is similar to the Nernst equation for redox reactions and is used to describe the potential at the ITIES where there is a 'common ion' dissolved in both emulsion phases. Because of this similarity, it is thought that the energetics at the ITIES follow the same laws as those for redox reactions, and this relationship has been shown, and used in the understanding of the electrochemistry of the ITIES, when studying electron transfer between immiscible liquids with the use of ions to fix the Galvani potential.

The standard ion transfer potential, $\Delta_O^W\phi_i^o$, can be used quantitatively to measure the relative affinity of the two ions in both phases when they are fully saturated. It cannot, however, be measured thermodynamically and is instead determined by measuring the distribution ratio of its salt, with the already known Gibbs free energy of transfer of its counterion. Tables have been calculated of the individual Gibbs energies of transfer for many ions in different solvents [76–79] using the assumption that the ions tetraphenylarsonium (TPAs$^+$) and tetraphenylborate (TPB$^-$) partition in the same ratio in any pair of solvents [80]. The Galvani potential, $\Delta_O^W\phi$, can also be measured thermodynamically using conventional electrochemical techniques [80–86].

A single–salt only can also be used to establish an interfacial potential by partitioning in both liquid phases and this is known as a distribution potential [74,87&88]. The general case for a monovalent 1:1 electrolyte partitioned in both phases is given by Equation **1.8** [74&88].

$$\Delta_O^W\phi = \frac{\Delta_O^W\phi_+^o + \Delta_O^W\phi_-^o}{2} + \frac{RT}{2F}\ln\frac{\gamma_+^O\gamma_-^W}{\gamma_+^W\gamma_-^O} \qquad \textbf{1.8}$$

When calculating the potential, for a 'common ion' or single-salt, the activity coefficient also needs to be determined. This would usually be assumed to be 1, i.e. for an ideal system, but DCE has a low relative dielectric permittivity, and therefore ion–association is likely to occur [88&89]. Ion–association is the formation of ion pairs of oppositely charged ions, and the degree of association in an electrolyte solution will result in the mean activity coefficient having a value less than unity. The activity coefficient for electrolytes in solution can be estimated using the Debye–Hückel Extended Law in Equation **1.9** [90].

$$-\log\gamma_\pm = \frac{|z_+z_-|A\sqrt{I}}{1+Ba\sqrt{I}} \qquad \textbf{1.9}$$

Where $\gamma_{\pm}$ is the mean activity coefficient for the electrolyte in solution, a is the distance of closest approach of the ions, and I is the ionic strength of the solution, determined using Equation **1.10**.

$$I = \frac{1}{2}\sum_i m_i z_i^2 \qquad \mathbf{1.10}$$

Where, m_i is the concentration of the cation or anion with valence z_i. In Equation **1.9**, A and B are solvent and temperature dependent constants,

$$A = \frac{e^2 N_\mathrm{A}}{2.3RT(8\pi\varepsilon_0\varepsilon)}\left(\frac{2\times10^3 N_\mathrm{A}{}^2 e^2}{\varepsilon_0\varepsilon RT}\right)^{\frac{1}{2}} \qquad \mathbf{1.11}$$

$$B = \left(\frac{2\times10^3 N_\mathrm{A}{}^2 e^2}{\varepsilon_0\varepsilon RT}\right)^{\frac{1}{2}} \qquad \mathbf{1.12}$$

Where N_A is the Avogadro number (6.0221 x10^{23} mol^{-1} [91]), R is the molar gas constant (8.3145 J mol^{-1} K^{-1} [91]), e is the elementary charge constant (1.6022 x10^{-19} C [91]), ε_0 is the dielectric permittivity in a vacuum (8.8542 x10^{-12} F m^{-1} [91]), ε is the relative dielectric permittivity of the solvent and T is the absolute temperature. The parameter a in Equation **1.9**, is the distance of closest approach of the ions in solution and can be calculated from the sum of the effective ionic radii. A schematic diagram linking a with the Debye Length is shown in Figure **1.2**.

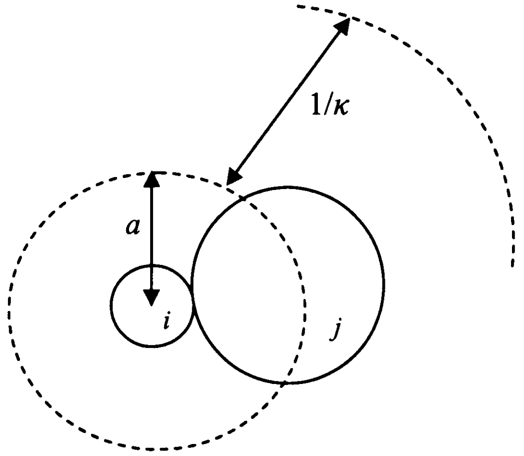

Figure 1.2: Schematic diagram showing the distance of closest approach, a, for an ion *i*, to an atmosphere ion *j*, and the corresponding Debye Length, 1/κ, for ion *i* [90].

The Debye Length ($1/\kappa$) can be calculated using Equation **1.13**,

$$\kappa = \left(\frac{2x10^3 e^2 N_A}{\varepsilon_0 \varepsilon kT} \right)^{\frac{1}{2}} \sqrt{I} \qquad \mathbf{1.13}$$

Where k is the Boltzmann constant ($1.3807 \text{ x}10^{-23}$ J K^{-1} [91]), and using the value for κ from Equation **1.13**, the Debye Length can be approximated to be the radius of the ion atmosphere, $r_a = 1/\kappa + a \sim 1/\kappa$ when $1/\kappa >> a$.

Due to the occurrence of ion association in solutions with low dielectric permittivity, the associated species will have a lower charge in solution, and hence a lower ionic strength, than the non–associated ions and the Debye–Hückel Extended Law does not account for this. Bjerrum's Theory [90] can be used to estimate the degree of ion association by calculating a critical distance, q, in the solution, below which the ions will form pairs. The basis of the Bjerrum Equation (Equation **1.14**) is that the Debye–Hückel theory can be used to calculate the activity coefficient, as long as the distance of closest approach of the ions, a, is greater than the critical Bjerrum distance q.

$$q=\frac{z_+z_-e^2}{8\pi\varepsilon_0\varepsilon kT} \qquad \mathbf{1.14}$$

A schematic diagram relating a to q is shown in Figure **1.3**.

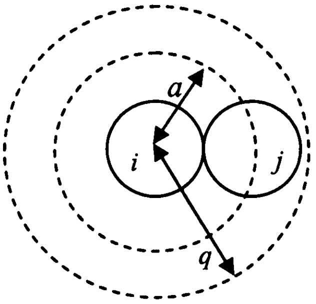

Figure 1.3: Schematic diagram showing the relationship between the distance of closest approach a, and the Bjerrum distance q, below which ion association will occur and the Debye–Hückel Extended Law will not hold true for calculations of the activity coefficient [90].

The values calculated from Equation **1.14** for the Bjerrum distance in the solution phases, can then be compared to the distance a for the ions, and it can be determined if the Debye–Hückel Extended Law is valid for the calculations of the activity coefficients.

1.1.3 Electrodeposition at the Liquid–Liquid Interface.

The interfacial potential, set–up by the potential–determining salts, can be utilised to electrodeposit metal at the liquid–liquid interface [92–111]. Electron transfer, between redox species present in immiscible liquid phases, can be induced by applying an interfacial Galvani potential difference using conventional electrochemical methods. This potential will drive an electron transfer reaction across the interface, providing there is a redox reagent in the organic liquid, and a metal ion or complex in the aqueous phase and this will follow the redox reaction in Equation **1.15**.

$$M^{+}_{(aq)} + Red_{(org)} \rightarrow Ox_{(org)} + M^{0}_{(m)} \qquad \textbf{1.15}$$

Recent literature on metal electrodeposited at the liquid–liquid interface, using a system of potential–determining salts, is summarised in Table **1.2**.

Liquid–Liquid Interface and Metal Deposited	Potential Determining Salts Used	Redox Couple Used	Experimental Investigations	Ref
Water–DCE Platinum and Palladium	Bis(triphenylphosphoranylidene) ammonium (BTPPA) chloride$_{(aq)}$ BTPPA tetrakis(pentafluorophenyl) borate$_{(org)}$ (Pd) BTPPA tetraphenylborate$_{(org)}$ (Pt)	Ammonium tetrachloropalladate$_{(aq)}$ Butylferrocene$_{(org)}$ or Ammonium tetrachloroplatinate$_{(aq)}$ Dimethylferrocene$_{(org)}$	Structural and electrochemical characterisation of the nanoparticles formed at the interface using 4–electrode cyclic voltammetry.	[92&93]
Water–DCE Palladium	Lithium perchlorate$_{(aq)}$ Tetrabutylammonium (TBuA) perclorate$_{(org)}$	Ammonium tetrachloropalladate$_{(aq)}$ Decamethylferrocene$_{(org)}$	Electrodeposition at bare and templated liquid–liquid interfaces.	[94]
Water–DCE Gold coated with tyramine	Tetraphenylarsonium (TPhAs) chloride$_{(aq)}$ TPhAs tetrakis(pentafluorophenyl)borate$_{(org)}$	Tetraoctylammonium tetrachloroaurate$_{(org)}$ Tyramine$_{(aq)}$	Simultaneous nucleation of gold and polymerisation of tyramine via the electron transfer reaction across the interface.	[96]
Water–DCE Silver	TBuA chloride$_{(aq)}$ TBuA tetrakis(pentafluorophenyl) borate$_{(org)}$	Silver Sulphate$_{(aq)}$ Butylferrocene$_{(org)}$	The mesoscopic particles are formed at nano liquid–liquid interfaces supported on micro– and nano–pipettes.	[104]
Water–DCE Palladium	TPhAs chloride$_{(aq)}$ TPhAs tetrakis(pentafluorophenyl)borate$_{(org)}$	Ammonium tetrachloropalladate$_{(aq)}$ Dimethylferrocene$_{(org)}$	Studying the influence of surfactants on the electrodeposition using cyclic voltammetry and chronoamperometry	[108]
Water–DCE Silver coated with polyphenylpyrrole	TPhAs chloride$_{(aq)}$ TPhAs tetrakis(pentafluorophenyl)borate$_{(org)}$	Silver Sulphate$_{(aq)}$ *N*–Phenylpyrrole$_{(org)}$	Electrodeposition of silver followed by the polymerisation of polyphenylpyrrole onto the particles.	[109]
Water–DCE Palladium	TBuA cloride$_{(aq)}$ TBuA tetrakis(pentafluorophenyl) borate$_{(org)}$	Ammonium tetrachloropalladate$_{(aq)}$ Butylferrocene$_{(org)}$	Describing a model for the diffusion controlled electrodeposition of metallic particles at the liquid–liquid interface.	[110]
Water–Toluene Gold	TPhAs tetrakis(4–chlorophenyl) borate$_{(org)}$ Tetrahexylammonium tetrakis(4–chlorophenyl) borate$_{(org)}$	Hydrogen tetrachloroaurate$_{(aq)}$ Tetraoctylammonium bromide$_{(org)}$	Describing the electrodeposition of gold clusters at the interface.	[111]

Table 1.2: Summarising the recent literature regarding electrodeposition at the liquid–liquid interface.

1.2 The Liquid–Liquid Interface in the form of an Emulsion

1.2.1 An Introduction to Colloids

The main area of interest in colloids is that of liquid–liquid systems, or emulsions, because this interface poses a more challenging experimental and technical problem to study than the solid–liquid and liquid–gas interfaces. This was shown in **1.1.1** and is due to the lack of appropriate *in situ* techniques that can be used to prepare and look at a stable, continuous liquid–liquid interface and also to give structural detail with a high resolution on a molecular scale. It has been proposed, therefore, that a colloidal emulsion system could be studied using Small Angle Neutron Scattering (SANS) to give this information.

A colloidal system can be defined as a small amount of one substance scattered finely and evenly in a large amount of another, and these substances are termed the *discontinuous phase* and the *continuous phase* respectively. There are many different types of systems and either phase can be a solid, liquid or a gas. Some of the different classes are *Disperse systems*, *Association colloids*, *Biocolloids*, *Macromolecular colloids* or *Multiple colloids* (three–phase systems). These are explained further in Table **1.3**, and examples of some dispersed systems seen everyday are fog, a liquid–gas aerosol, milk, a liquid–liquid emulsion, or even paint, a solid–liquid colloid.

The class of a particular colloid is determined by the nature and size of the phases present and all colloids need to have at least one of their phases in the size range of 1–10000 nm to show colloidal properties [112]. This small size causes a high surface–to–volume ratio and therefore an increase in surface chemistry effects. It is these surface interactions that are the main cause of the properties seen as the system destabilises.

Class	Example	Discontinuous Phase	Continuous Phase	
Disperse Systems *A dispersion of a fine substance in another*	Milk – an emulsion	Liquid	Liquid	
	Aerosol sprays	Liquid	Gas	
	Toothpaste	Solid	Liquid	
	Pearls	Solid	Solid	
	Foams	Gas	Liquid	
	Industrial smokes	Solid	Gas	
Association Colloids *Where molecules of soap or surfactants are associated together to form micelles in a liquid*	Soap/water	Micelles	Solvent	
	Dye solutions	Micelles	Solvent	
Biocolloids *Any biological structure that has a colloidal nature*	Blood	Corpuscles	Serum	
	Bone	Hydroxyapatite	Collagen	
Macromolecular Colloids *A dispersion of macromolecules in a liquid*	Jellies	Macromolecules	Solvent	
	Glue	Macromolecules	Solvent	
Multiple Colloids *Three phase systems that coexist together with two phases finely divided*		**Coexisting Phases**		
	Oil–bearing rock	Porous rock	Oil	Water
	Mineral flotation	Mineral	Water	Air bubbles or Oil drops

Table 1.3: Showing different classes and examples of colloid systems and their constituent phases [112].

1.2.2 Emulsion Destabilisation

The main factors that affect the stability of colloids are gravity and the surface energy of the system. It is these two factors that cause the four main processes that lead to the phase separation of a colloid. These processes are *sedimentation* [112], *creaming* [112–116], *flocculation* [116–120] and *coalescence* [17&119,121–124]. The formation of a colloid causes an increase in the entropy of the system but also, due to the high surface–to–volume ratio, an increase in the surface energy. This makes the system unstable and likely to separate into two phases unless the surface energy, or interfacial tension, can be lowered. Flocculation and coalescence are caused by this high surface energy of the discontinuous phase. As the particles in the sub–phase group together, the surface energy is lowered and the colloid becomes more stable. Flocculation is when the particles group together as small clumps or *flocs*, with the original particles still defined within the new cluster. Coalescence is when they join to form larger particles and here the original particles fuse together to form a larger unit. This can be seen in Figure 1.4.

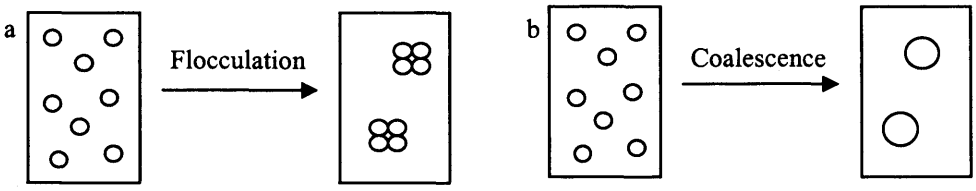

Figure 1.4: Schematic diagram showing the processes of (a) Flocculation – where the particles cluster together, and (b) Coalescence – where the particles fuse to form a larger unit.

The processes of coalescence and flocculation can be prevented if the surface energy of the drops can be reduced. This is most commonly achieved using a surfactant adsorbed onto the interface between the two liquids. A liquid–liquid colloid is commonly termed an 'emulsion' and flocculation would not be seen to occur in such a system unless there was adsorption at the interface.

Sedimentation and creaming, however, are both caused by gravity and the difference in density between the two phases. This is seen by the separation of the two phases with the discontinuous phase either sinking to the bottom or rising to the top, respectively, Figure **1.5**.

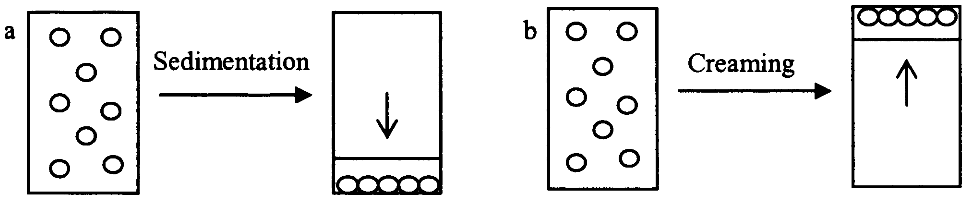

Figure 1.5: Schematic diagram showing the processes of (a) Sedimentation – where the discontinuous phase is more dense than the continuous phase and therefore falls to the bottom, and (b) Creaming – where the discontinuous phase is less dense and rises to the top.

The effects of gravity can be reduced or prevented by matching the densities of the two phases. This could be achieved by dissolving a density–increasing species into the phase with the lower density, using a concentration that would match them.

Another factor that can affect the stability of emulsion systems is that of *Ostwald ripening* or *molecular diffusion* [124–134]. This occurs when there is a liquid–liquid system made up of non–uniform sized drops and the larger drops are seen to grow at the expense of the smaller ones due to the differences in their chemical potential. The growth of the drops is via a process of molecular diffusion where molecules of the discontinuous phase move through the continuous phase to add to larger drops.

1.2.3 Emulsion Creation

Emulsions can be created either by dispersion – breaking down the bulk material via shaking or stirring; or condensation of the discontinuous phase – building up the drops [112]. Dispersion methods generally form emulsions with an inhomogeneous and uncontrolled size distribution, with the discontinuous phase maintained with the use of surfactants. Condensation methods, however, allow for molecular clusters to form which grow via molecular diffusion to produce drops with a homogeneous size distribution. Emulsions can be made using this method by heating a mixture of oil and water, where the solubility of the dispersed phase, e.g. oil, in the continuous liquid, e.g. water, will increase, creating a saturated solution. This is then cooled rapidly, thereby decreasing the solubility and causing the oil to condense from the water as small homogeneous drops [135]. The drops form initially via a process of nucleation where a cluster of molecules aggregate to make a critical nucleus of dimensions 1–10 nm, where the change in Gibb's free–energy with respect to cluster size is zero.

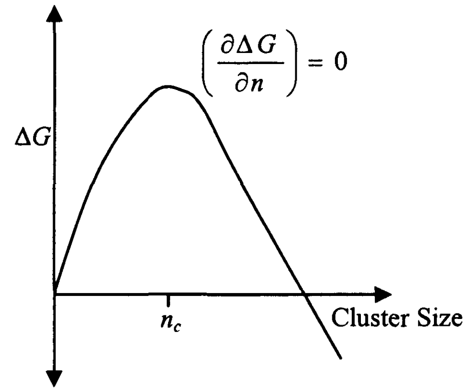

Figure 1.6: Showing the change in free–energy with increasing cluster size [112]. The formation of the critical nucleus, n_c, occurs when $\left(\frac{\partial \Delta G}{\partial n}\right) = 0$.

This is illustrated in Figure **1.6** and the cluster size of the critical nucleus (n_c) has been shown to be in the order of 4 molecules for the nucleation of water [136].

The extent of nucleation depends on the saturation of the oil in water; when the temperature of the system is decreased rapidly, this causes the concentration of the aqueous dissolved oil to suddenly go above the critical supersaturation point, causing the oil to spontaneously nucleate to reduce the concentration to below the critical point. Once this concentration is reached, no more nucleation will occur and instead the existing clusters will grow via molecular diffusion until the excess aqueous dissolved oil is depleted [112]. This is illustrated in Figure **1.7**.

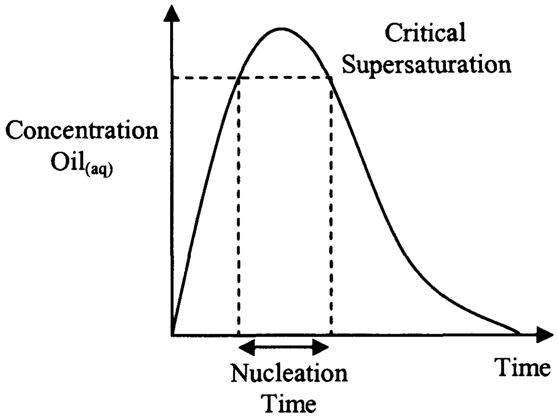

Figure 1.7: Showing the Critical Supersaturation point and corresponding Nucleation Time, after which the drops grow via molecular diffusion [112].

Because the nucleation is spontaneous and the nucleation rate very fast, the resulting emulsion will have a monodisperse size distribution.

1.2.4 The DLVO Theory Describing Emulsion Stability

The Deryagin–Landau–Verwey–Overbeek (DLVO) theory describes the stability of liquid–liquid emulsions being controlled by the interaction free–energy as a function of drop separation; i.e. a sum of the contributions from the attractive Van–der–Waals interactions, Ψ_a, and repulsive Coulomb interactions between the double layers of two drops, Ψ_r [112,137&138]. A simplified form is given as Equation **1.16**.

$$\Psi_{tot} = \Psi_a + \Psi_r \qquad \mathbf{1.16}$$

Where Ψ_{tot} is the total interaction potential and Ψ_a is defined by Equation **1.17**.

$$\Psi_a = -\frac{Ar}{12d} \qquad \mathbf{1.17}$$

Where A is the Hamaker constant determined from the materials forming the two emulsion phases (~ 10^{-20} J), r is the drop radius, and d is the separation distance between two drops.

The Coulomb interactions, Ψ_r, arise due to the presence of an electrical double–layer at the liquid–liquid interface, and the widely accepted model is the Gouy–Chapman approximation [139], which describes the layer of charge on the surface of a particle to be balanced by a region of opposite charge in the surrounding medium. In a liquid–liquid emulsion system containing potential–determining ions, this would be seen as two diffuse regions either side of the interface and this is illustrated in a schematic diagram, Figure **1.8**.

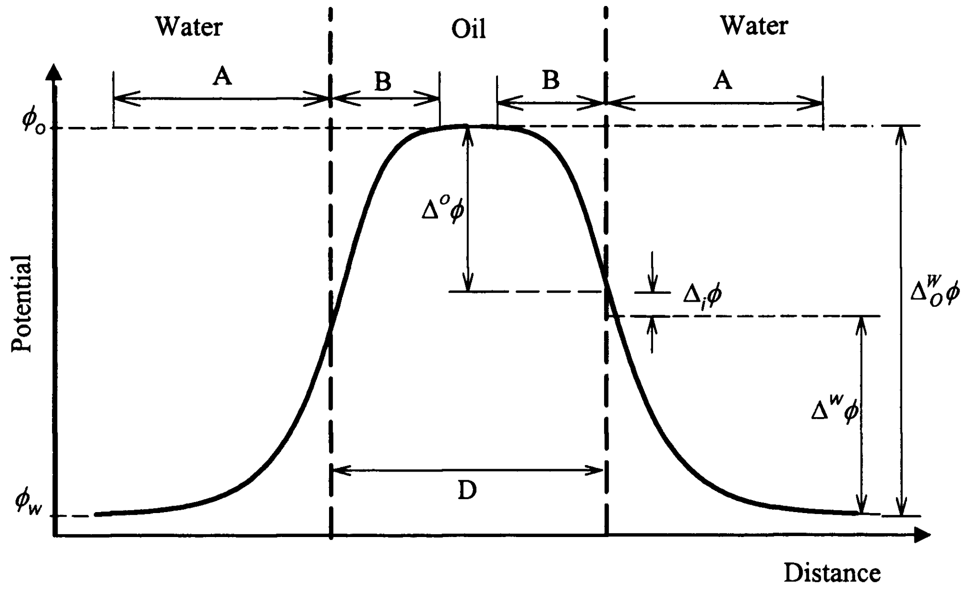

Figure 1.8: Schematic diagram of the Gouy–Chapman model showing the electrical potential distribution across an oil-in-water emulsion drop. Included is the interfacial potential difference, $\Delta^W_O\phi = \phi_W - \phi_O$, and the layers A and B are the diffuse layer thicknesses in the aqueous and oil phases respectively. D is the drop diameter and the vertical dashed lines represent the liquid–liquid interface either side of the DCE drop.

Figure **1.8** shows a schematic diagram of the potential drop at the interface of a water-oil-water system, e.g. across an emulsion drop. There are two diffuse layers A and B on either side of the liquid–liquid interface and an indication of the thickness of these layers is given by the Debye length, $1/\kappa$ for each solution phase.

The Coulomb interactions, Ψ_r, can then be calculated using Equation **1.18**.

$$\Psi_r = 2\pi\varepsilon r\zeta^2 \ln[1 + \exp(-\kappa d)] \qquad \textbf{1.18}$$

Where ε is the dielectric permittivity of the continuous phase, κ is the Debye–Hückel parameter or inverse Debye–length, and ξ is the surface zeta–potential. The zeta–

potential is the potential measured at the outer edge of the diffuse layer, termed the Stern, Outer Helmholtz or Shear Plane [139–141], shown in Figure **1.9**.

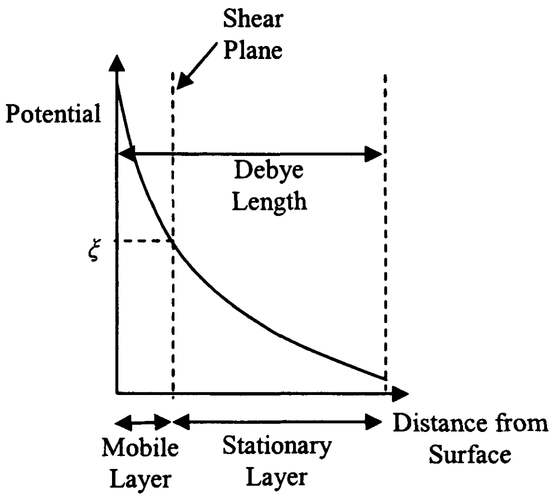

Figure 1.9: Schematic diagram showing the location of the Shear Plane and corresponding zeta–potential, ξ. Also included is the relationship to the double–layer Debye–Length ($1/\kappa$).

For an electrochemical potential established using potential–determining ions, there would be a Shear Plane located either side of the liquid–liquid interface, as described in Figure **1.8**, and hence give rise to positive and negative zeta–potentials of equal magnitude.

1.2.5 Surfactant–Stabilised Emulsions

Once an emulsion has been created without stabilisation, either by dispersion or condensation, the attractive Van–de–Waals forces will be higher than the repulsive Coulomb interactions and this will eventually result in phase separation. Most emulsion systems therefore include a stabilising *surfactant* which acts by partitioning or adsorbing at the interface. This will lower the surface energy between the two phases and an example would be the formation of micelles, a schematic diagram of which is shown in Figure **1.10**.

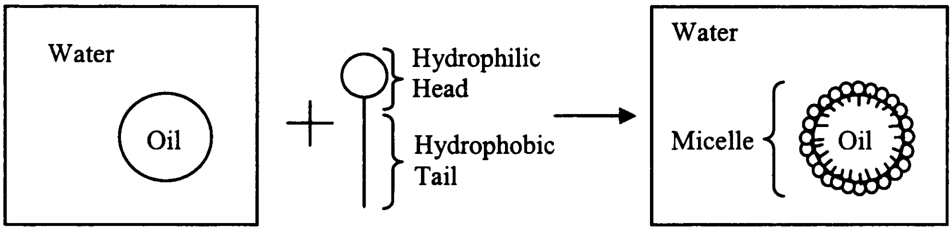

Figure 1.10: Schematic diagram showing a representation of a micelle by surrounding an oil drop with lipid molecules. The hydrophobic tail of the lipid is soluble in the oil and the hydrophilic head is soluble in the surrounding water. This creates a layer around the oil drop allowing it to remain suspended in solution by preventing coalescence.

The addition of surfactants to a simple emulsion system creates an association colloid system, as described in Table **1.3**, and there has been much research on the characterisation of emulsions stabilised using surfactants [117,125,127&128]; namely the interfacial adsorption of surfactant molecules [66], proteins [142] and other macromolecules [24] and their effect on the destabilising processes [128]. This information is useful to the food processing industry as protein stabilised colloids influence such properties as shelf life and foam stability in many food processes. Also enzyme modified oil–water colloids are of interest to the pharmaceutical industry [81]. When surfactants are used in a liquid–liquid system, the surface of the drops is covered with a hydrophilic layer allowing a hydrophobic, discontinuous phase to remain suspended in an aqueous, continuous phase, Figure **1.10**. These studies using such a stabilised emulsion do not, however, give any information on the 'clean' liquid–liquid interface

1.2.6 Research into Surfactantless Emulsions

The lack of structural information about the 'clean' liquid–liquid interface leads to the need for a liquid–liquid emulsion system that can be prepared and stabilised, without the use of surfactants. This would give a 'clean' interface between the two phases that could be studied easily to gain structural details of the interface. Studies into surfactant–less emulsions can be seen in Table **1.4** and, despite the promising work of R.M. Pashley *et al* [149–151] and M. Abe *et al* [118,119,126,143–148], research is still limited in this field.

As can be seen from Table **1.4**, work has primarily been done on stabilising a surfactant–free liquid–liquid emulsion and investigating the destabilising processes that affect them. It can also be seen that the possible use of a surfactantless emulsion as a model liquid–liquid interface has yet to be utilised.

Emulsion System	Preparation Method	Phenomenon Studied and Data Obtained	Ref
Benzene, Cyclohexane and Polystyrene in Water	Agitation followed by Ultrasonication	Investigation of the stabilising effect of added polystyrene using light scattering, turbidity, viscosity, interfacial tension, and zeta–potential measurements of the emulsion.	[143]
n–Decane in Water	Ultrasonication	Coalescence and Ostwald Ripening rates measured using a Single–Droplet detection method from fluorescence–bunching signals.	[144]
Benzene, Fluorobenzene, *n*–Hexane or Cyclohexane and Pyrene in Water.	Ultrasonication	Fluorescence measurements comparing the stability of emulsions containing pyrene dissolved in different hydrocarbon oil phases.	[145]
Hydrocarbon (C_6–C_{16}) in Water	Ultrasonication	Molecular diffusion and droplet size using dynamic light scattering and freeze–fracture microscopy.	[126]
Benzene in Water	Ultrasonication	Flocculation, evolution and growth of the oil drops using freeze–fracture microscopy.	[118&119]
Oleic Acid and its Esters in Water	Ultrasonic Dispersion	Emulsion formation, surface properties and the environment of the oil drops using dynamic light scattering, size distribution, interfacial tension, zeta–potential, Fourier–transform infra–red spectroscopy and fluorescence spectrum measurements.	[146]
Tetralin, Benzene and *n*–Hexadecane in Water	Ultrasonication	Dispersion and stabilising effects of n–Hexadecane using size distribution, dynamic light scattering and interfacial tension measurements.	[147]
Benzene, Hexane, Cyclohexane or Fluorobenzene in Water	Sonication or Mechanical Dispersion	Evolution and growth of the drops using size distribution, light scattering and conductive probe measurements.	[148]
Soybean Oil, Perfluorooctyl bromide, Perfluorohexane, Propofol or Griseofulvin in Water	De–gassing by Freeze–Thaw Cycling followed by Agitation	Particle size, zeta–potential and turbidity measurements, to investigate de–gassing as a method of forming stable surfactantless emulsions containing water insoluble drug–delivery oils.	[149]
Hexane, Octane, Decane, Dodecane, Octadecane, Squalane or 4–fluorotoluene in Water	De–gassing by Freeze–Thaw Cycling followed by Agitation	Particle size, zeta–potential and turbidity measurements, to investigate de–gassing as a method of forming stable surfactantless emulsions containing different hydrocarbon oil phases. The effect of pH on the emulsions was also studied. A mechanism based on the 'fingering' of the oil into the water was proposed.	[150–152]
Hexadecane in NaCl solution	Homogenisation	Electroacoustic measurements to investigate the stabilisation due to hydroxyl ions with changing pH.	[153]

Table 1.4: Summarising research into surfactantless emulsions systems and how they were prepared and studied.

1.3 Protein Adsorption and Small Angle Neutron Scattering

1.3.1 An Introduction to Proteins and Bovine Serum Albumin

Proteins are a very important class of biochemical molecules because they are the basis for the major structural or mechanical components of animal and human tissue and play a role in almost every biological process. They are built from 20 simple amino acids consisting of an amino group, a carboxyl group, a hydrogen atom and a specific R group or side chain. These acids can be hydrophilic, hydrophobic or neutral and are also chiral molecules. Figure **1.11**, shows the basic amino acid unit and the 20 different R groups arranged according to their pH [154]. These amino acids are then linked via peptide bonds to form a polypeptide chain, the linear primary structure of proteins, with each protein being made from a different combination. The amino acid sequence for Bovine Serum Albumin (BSA) is shown in Figure **1.12** [155] derived from complementary DNA data. Also included in the structure, are the positions of 17 disulphide bridges that form between adjacent cysteine amino acids and give rise to the looped configuration of the polypeptide chain. The primary structure has been classified as having 3 domains, as labelled in Figure **1.12**, and the linear pattern of loops with short–range coupling between the cysteine groups, gives BSA a flexible structure and resistance to extreme conditions. This is because the loops can associate together to form a globular structure, but can also separate reversibly.

Figure **1.12** also shows that BSA has a low content of tryptophan, methionine, glycine and isoleucine; and large numbers of cysteine, leucine, glutamic acid and lycine. This causes the protein molecule to have a high total charge, 185 ions per molecule at pH 7, and also a net negative charge of –17, due to there being more acidic amino acids than alkaline. The net charge of the protein is not spread evenly along the whole polypeptide, however, but is instead different for each domain. The calculated net charges, therefore, for each domain are –11, –7, and +1 for domains I, II and III [155]. The isoelectric point has been determined to be at pH 4.7 [155].

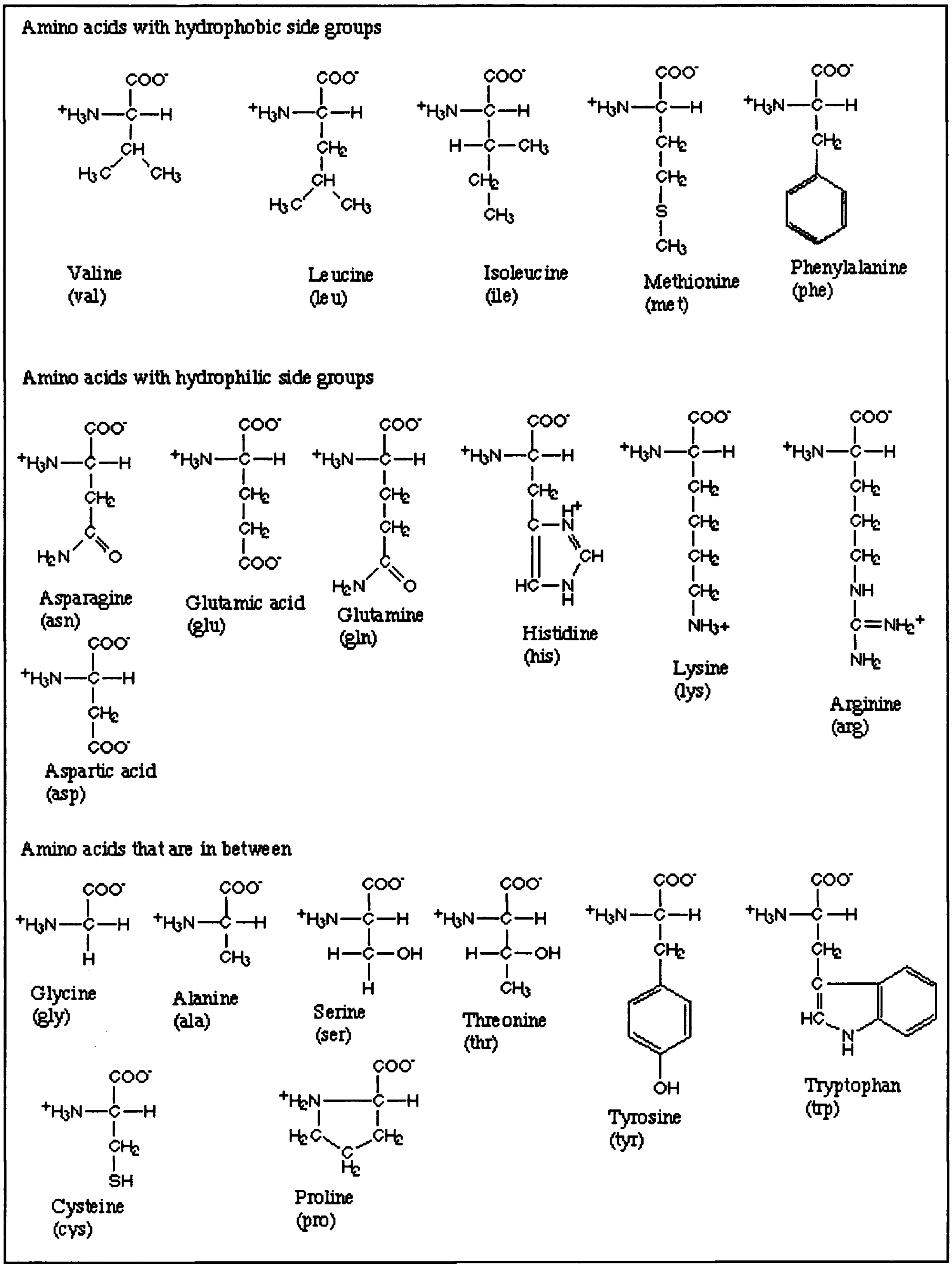

Figure 1.11: Showing the molecular structure of the 20 amino acids arranged according to their pH.

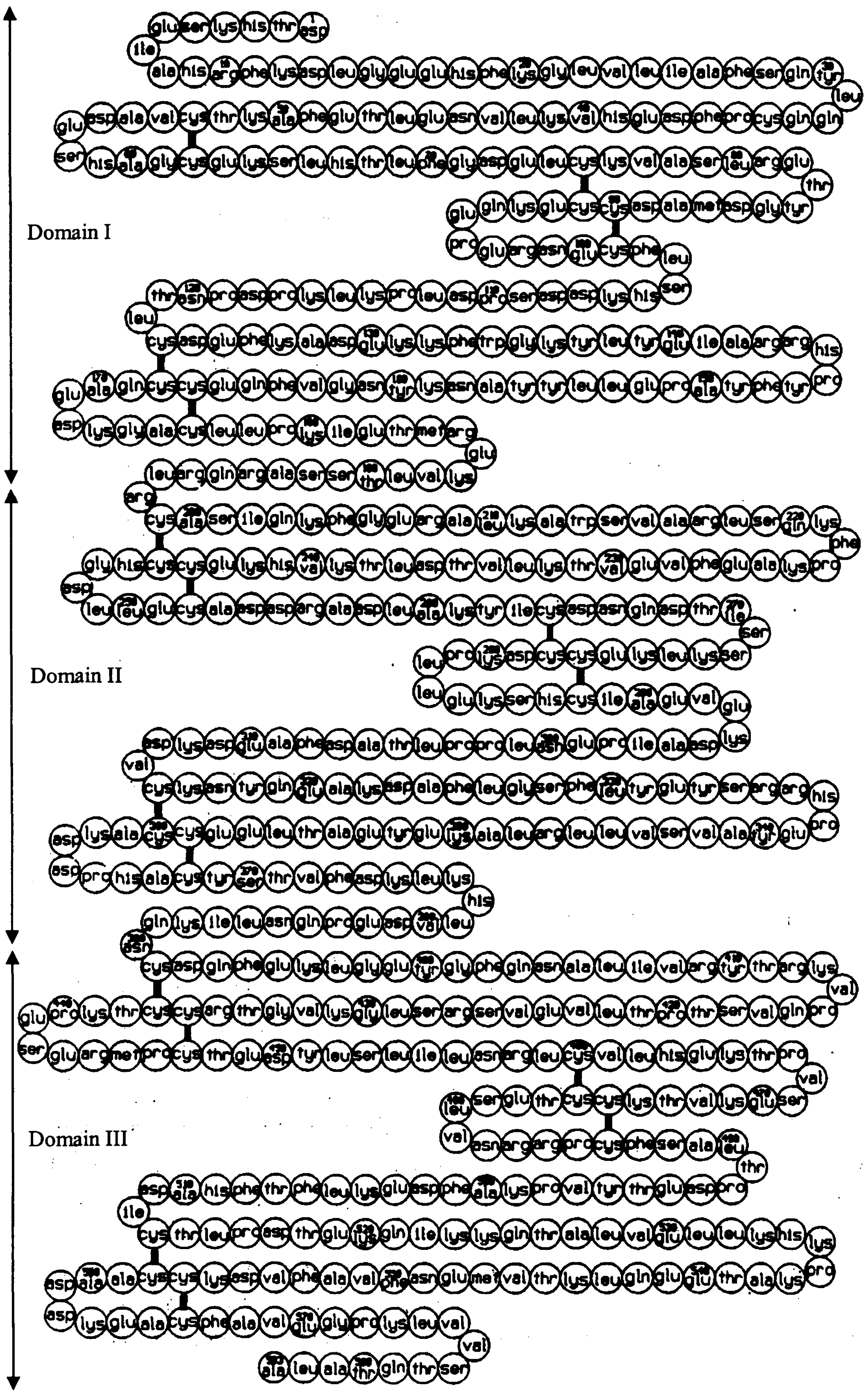

Figure 1.12: The determined amino acid sequence of BSA and the positions of the 17 disulphide bridges and 3 Domains [155].

The secondary structure of a protein details how the polypeptide chain is arranged. This can either be as an α helix – a rod–like structure where the polypeptide chain is tightly coiled, with the amino acid side groups extending outward in a helical array, and is stabilised by hydrogen bonds between all the NH and CO groups on the main chain; or a β pleated sheet – where the polypeptide chain is almost fully extended and is stabilised by hydrogen bonds between NH and CO groups on different polypeptide strands. The polypeptide chain can be present as both structures in the protein molecule and it is the nature of folding and spatial arrangement of the chain that gives rise to the protein tertiary structure. BSA has been shown to have 68 % of the tertiary structure as α helixes, 17 % in the β form, and the remainder being extended peptide chains [155]. The tertiary crystal structure, and native state, of BSA is shown in Figure **1.13** [156&157].

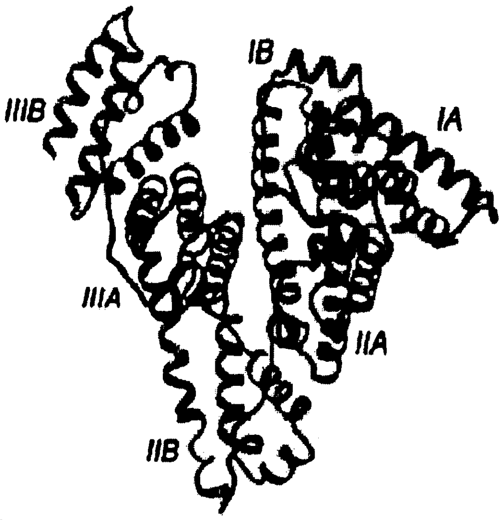

Figure 1.13: Tertiary crystal structure of BSA showing the spatial arrangement of the domains I, II and II. These domains have been further split into two subdomains, A and B, which share common structural features [156].

As mentioned, BSA is a flexible protein that is resistant to moderately harsh conditions, such as extremes of temperature and pH. Under such conditions, the native structure changes conformation due to disruptions of the noncovalent interactions that maintain the globular shape, and BSA has been shown to exist in 5 different isomers according to the pH: **E** (extended) below pH 3, **F** (fast) at pH 4, **N** (normal) around pH 7, **B** (basic) near pH 8, and **A** (aged) near pH 10. Movement between these isomers is reversible and does not result in complete denaturation, or an irreversible loss of structure and function.

In solution, two conformational forms have been suggested for BSA; firstly a heart–shape with dimensions 84 x 84 x 31.5 Å [159], similar to the crystalline, or **N**, form and that of human serum albumin in solution; and secondly an oblate ellipsoid, or cigar shape, with dimensions 140 x 40 x 40 Å [155]. A schematic diagram of the cigar shape showing the 3 domains can be seen in Figure **1.14**.

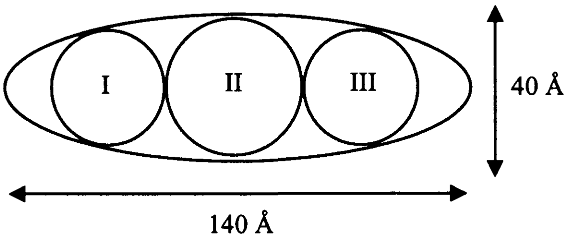

Figure 1.14: Schematic diagram showing the oblate ellipsoid conformation and domain positions, for BSA in solution.

Overall, BSA is a well characterised water soluble protein and its function is as a binding protein that transports chemicals, in the blood, thereby regulating the distribution of water and maintaining the osmotic pressure in the body. Because of these binding properties, BSA has been shown to adsorb at interfaces, via physical adsorption, as a monolayer with dimensions supporting those in Figure **1.14**, without losing any globular structure [160]. Fluorescent X–Ray interference patterns have shown that BSA molecules adsorb with their short axis perpendicular to the interface

[161] with a calculated surface area per BSA molecule of 7070 Å^2 [155]. This value corresponds to a flattening of the BSA molecule at the interface, due to a partial unfolding of the structure, and it has been shown that there is a loss of α helix structure and gain of random coil upon adsorption at equilibrium, with an intermediate β structure [162].

1.3.2 Investigating Adsorption at the Liquid–Liquid Interface using Small Angle Neutron Scattering.

As described, proteins adsorb via physical adsorption – i.e. electrostatic and hydrogen bonding interactions, at the liquid–liquid interface to form a monolayer, resulting in a conformational change in the protein molecule, but not irreversible denaturation [163]. This can happen at an emulsion interface, and the rate of adsorption of BSA has been reported to be very fast once the interface has formed, and acts to give increased stability to the emulsion [164–173].

A technique that has been used to investigate an adsorbed layer is Small Angle Neutron Scattering (SANS). This is a simple diffraction technique that uses the considerable difference in the scattering of a neutron from hydrogen nuclei compared with that from a deuterium nucleus, to determine structural information about the size and shape of molecules, and experiments using SANS to probe an adsorbed interfacial layer are summarised in Table **1.5**. From this table, it can be seen that SANS has primarily been used to study the adsorption of surfactants at the interface, with the adsorption of protein being restricted to solid–liquid or gel–liquid interfaces. There is however, no reason why SANS should not be used to investigate protein adsorption at an emulsion interface.

Interface	Adsorbed Layer Studied	Information Obtained	Ref
Water–Heptane	Blended cationic Didodecyldimethylammonium bromide and Poly(ethylene glycol) monododecyl ethers	The effect of changing size of ether on the emulsion stability, nanostructure and interfacial composition, showing that longer chain ethers partition strongly into the surfactant layer whilst shorter chains adsorb much more weakly.	[56]
Water–*n*–Octane	Coadsorbed 1,2–*n*–Octanoyl–*sn*–glycero–3–phosphocholine and *n*–Pentanol, *n*–Hexanol or *n*–Octanol.	Droplet structure and composition of the adsorbed layer showing interfacial partitioning of the alcohols.	[58]
Hexadecane–Water	Mixed Hexaethylene glycol monododecyl ether and Sodium dodecyl sulphate.	Structure and composition of the adsorbed mixed–surfactant layer with increasing surfactant concentration and the formation of micelles.	[55]
Ethyl octanoate–Water	*N*,*N*–Dimethyldodecylamine–*N*–oxide	Details of the structure and composition of the emulsion interface using contrast variation and model fitting.	[59]
Decane–Water	Pentaethylene glycol dodecylether	The microstructure of the emulsion over a range of surfactant concentrations and the effects of changing temperature on the micellar size and shape.	[174]
Ceramic membranes–Water	Bovine serum albumin and Human serum albumin	Extent of protein deposition at the pore membrane interfaces with changing pH.	[175]
Surfactant–Water	Mixed Pentaethylene glycol *n*–dodecyl ether and Sodium decyl sulphonate	Measurements of the bulk and interfacial properties of lamellar mixtures of surfactants in water.	[67]
Silica gel–Water	Lysozyme crystals	The protein is seen to adsorb on the gel surface and the rate of adsorption increases with increasing protein concentration.	[176]

Table 1.5: Summarising the literature concerning experiments using SANS to probe adsorbed layers at an interface.

1.4 Summary

Overall, it can be seen that there is a need for structural and dynamical information at the molecular level, regarding the 'clean' liquid–liquid interface due to its importance in many fundamental processes, and recent techniques using spectroscopic techniques have shown promising results. Information obtained regarding the DCE–water interface is still mainly from theoretical predictions and experimental results are in disagreement as to whether the interface is molecularly sharp [43] or a diffuse 'mixing' region between the two liquids [29].

It has been proposed that SANS could be used as a technique to probe the liquid–liquid interface with and without adsorbed protein, and to do this a surfactantless emulsion needs to be developed that is stable for the timescales of the experiment. This would therefore need to be resilient to the effects of gravity and have an 'electrified' interface so as to prevent drop coalescence.

Presented in this thesis are results concerning the development and characterisation of such an emulsion, and also data from SANS experiments investigating an adsorbed layer of BSA at the emulsion interface. The utilisation of the established potential to electrodeposit interfacial palladium is also described.

Chapter 2: Experimental Materials, Methods and Equipment

2.1 Materials

The water (H_2O) used in experiments, was HPLC grade (Fluka), whereas the H_2O used for cleaning, was from a Milli–Q Gradient 18.2 MΩ cm (at 25 °C) water system. Sulphuric acid (H_2SO_4) (0.1 M, BDH; Analar grade with a minimum assay of 98.0 %) was also used when cleaning all glassware.

The emulsions were composed of 1,2–dichloroethane (DCE) (Sigma; 99+ % spectrophotometric grade) and deuterium oxide (D_2O) (Aldrich; 99.9 % atom D) and stabilised by dissolving a density–matching species in the aqueous layer and different potential–determining ions in the DCE or D_2O phase. To match the gravimmetric densities of the two phases, both glucose (Aldrich) and sucrose (Aldrich; 99+ % ACS reagent) were investigated. The different salts used were lithium tetrakis(pentafluorophenyl)borate (diethyletherate) (LiTPFB) (Boulder Scientific, CO, 98 % pure), tetraheptylammonium bromide (THpABr) (Sigma), tetraethylammonium chloride (TEACl) (Fluka Biochemika; ≥99 %), tetrabutylammonium chloride (TBuACl) (Fluka Chemika; >97 %), and sodium tetraphenylborate (NaTPB) (Aldrich; 99.5+ % ACS reagent).

For the electrochemistry experiments, tetrathiafulvalene (TTF) (Aldrich; 97 %) was used as the electrochemical probe. This was also used in UV–Vis experiments to determine the organic–ion concentration in the emulsion drops. Other probes tested in the electrochemistry experiments, were ferrocene (Fc) (Fluka; ≥98 %) and butylferrocene (BuFc) (Aldrich; 97 %).

The dyes used in optical microscopy experiments were oil–soluble Sudan Black (Aldrich) and water–soluble Brilliant Blue (Sigma).

For Small Angle Neutron Scattering (SANS) experiments, the protein Bovine Serum Albumin (BSA) (Sigma; ≥97 %) was partitioned at the liquid–liquid interface, and deuterated 1,2–dichloroethane ($C_2D_4Cl_2$) (d–DCE) (Aldrich; 99 atom % D) was used in phase contrasting.

Using a D_2O–in–DCE (water–in–oil) emulsion, the emulsion interfacial potential was manipulated to drive an electrodeposition reaction. Ammonium tetrachloropalladate (II) ($(NH_4)_2PdCl_4$) (Aldrich; $\geq$99.995 %) and dimethylferrocene (DmFc) (Aldrich; 97 %) were used as redox reagents, and lithium sulphate (Li_2SO_4) (Sigma; 99 %) and lithium chloride (LiCl) (Aldrich; 99.99 %) were added to 'salt–out' the solution.

All chemicals were used as received.

2.2 Glassware Cleaning

Glassware was thoroughly cleaned by boil washing in sulphuric acid solution to remove any contamination from detergents, which could possibly act as a surfactant. All glassware was put into a large 2 L glass beaker and this was then filled with deionised water until it covered the glassware by approximately 5–8 cm.

Concentrated H_2SO_4 (0.1 M) was added very slowly to the beaker with a pipette and this was done in a fume cupboard and protective clothing was also worn.

The filled beaker was then heated, to allow the solution to boil, for 2 hours until half the water had evaporated and this was then left to cool. Next, the H_2SO_4 solution was poured away and the glassware rinsed thoroughly with deionised water several times, and then left to dry overnight in an oven at 65 °C.

For equipment that had plastic or metal components, it was first washed in deionised water directly from the water system; water was not used from plastic bottles as these could be contaminated with plasticisers. The equipment was then washed with ethanol and put in the oven to dry. If there was only metal, and no plastic components, then the equipment was also rinsed with acetone before drying.

2.3 Synthesis of Tetraalkylammonium Tetraphenylborate Salts

Firstly equimolar amounts (0.01M) of tetraalkylammonium chloride (TXACl, where X = methyl, ethyl, propyl, butyl etc.) and sodium tetraphenylborate (NaTPB) were dissolved separately in water and in a mixture of 2:1 water to ethanol, respectively. These solutions were then mixed together in an open beaker and left to stand for 2–3 hours.

The solution was filtered and the fine, crystalline precipitate of salt was washed well with water to remove any NaCl. The washings were tested for Cl^- ions using $AgNO_3$, which would turn white if any were present, and the salt was then left to dry overnight in an oven at 65 °C.

To purify by recrystallisation, the crude salt was dissolved in a minimum amount of hot acetone and stirred well. Some drops of ethanol were added and the solution was heated gently, with stirring, to remove the acetone. It was then left to cool and recrystallise. If, after removing the acetone, precipitation instead of recrystallisation occurred, enough hot acetone was re–added to dissolve this precipitate and the solution was then heated again.

When cool, the solution was filtered, washed well with ethanol and oven dried overnight. The filtrate and ethanol washings were also recrystallised as above, filtered, washed and dried separately.

The remaining filtrate and washings were heated to remove any acetone and then left to cool overnight to see if any remaining salt was present.

2.4 Procedure for Creating a DCE–in–D_2O Emulsion

The emulsion was created using a condensation technique and the manipulation of the solubility of DCE in water and its subsequent changes with temperature [135]. Firstly, 10 cm^3 D_2O or H_2O and 1 cm^3 DCE were mixed in a 25 cm^3 stoppered, glass conical flask. A stirrer bar was added and the flask was then put into a 500 cm^3 glass beaker water–bath on a hot–plate. This was heated to 65 °C, with gentle stirring, for 1 hour to ensure that the aqueous phase became fully saturated with the DCE. The flask was then put into a water–bath (Grant LTD 6; Grant Instruments, UK) set at 15 °C and left to cool for 30 mins. This decrease in temperature caused a decrease in the solubility of the DCE in water and resulted in the DCE condensing out of the aqueous phase as emulsion drops.

After the solution had cooled for 30 mins, a sample of the emulsion was taken for analysis using a variable volume pipette (Volac 200–1000 μl) with a modified tip. The pipette tip was cut approximately 5 mm from the end, to increase the surface area of the opening, and so reduce the shear forces when pipetting the solution. Care was also used when the sample was taken, to avoid withdrawing large drops of suspended DCE. These were always present in the bulk solution due to the excess volume of DCE used in the formation of the emulsion.

2.5 Stability Measurements

As a measure of stability with time, the turbidity of the emulsion was monitored using a PC–controlled UV–Vis spectrophotometer (Agilent 8453 UV–Vis Spectroscopy System; Agilent Technologies, Germany) with a thermostatted cell holder set to the emulsion cooling temperature. The absorbance spectra between 190–1100 nm was recorded every 10 secs and, even though the processes of sedimentation and coagulation could not be quantified separately, this gave a qualitative measure of the turbidity of the sample. This is because the UV–Vis spectrophotometer records the light scattering from the emulsion drops and hence its turbidity. As the emulsion destabilises, i.e. the drops change in size or sediment due to gravity, the emulsion slowly clears and hence the turbidity decreases. To compare the obtained data for each emulsion studied, the absorbance or turbidity was taken at 550 nm every 10 secs. This wavelength was chosen because, from a scan of the emulsion across the 190–1100 nm range, there was no measurable absorbance peak at this value, and it was therefore assumed that the spectra was purely emulsion scattering at this wavelength. 10 mm or 2 mm pathlength Far–UV quartz cuvettes (Hellma UK Ltd) were used in the spectrophotometer and were filled to the top to prevent any DCE evaporating out of the emulsion into any headspace at the top of the cuvette.

2.6 Optical Microscope Experiments

The emulsion drop volume and number density were determined using Optical Microscopy (Jenalab; Carl Zeiss, Germany), with bottom illumination, connected to a video camera (TK–1085E; JVC, Japan) with PC data collection (Presto Video Works Ver 4.1 Rev 6; NewSoft Technology Corp, Taiwan). The temperature was maintained and controlled with the use of a peltier device (Thermo Electric Cooler (TEC) Type DT 1069; Marlow Industries Inc., USA), Figure **2.1**, positioned on the stage of the microscope.

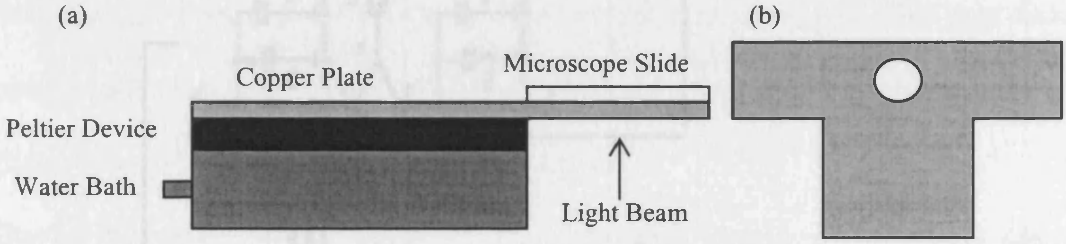

Figure 2.1: Schematic diagram of the microscope platform temperature controller set–up showing (a) side view and (b) top view. Not to scale.

This was connected to a variable current supply temperature selector (built in–house; R. Waymark, Figure **2.2**: circuit diagram) and the copper plate above the peltier device, allowed for efficient heat transfer between the peltier device and the microscope slide.

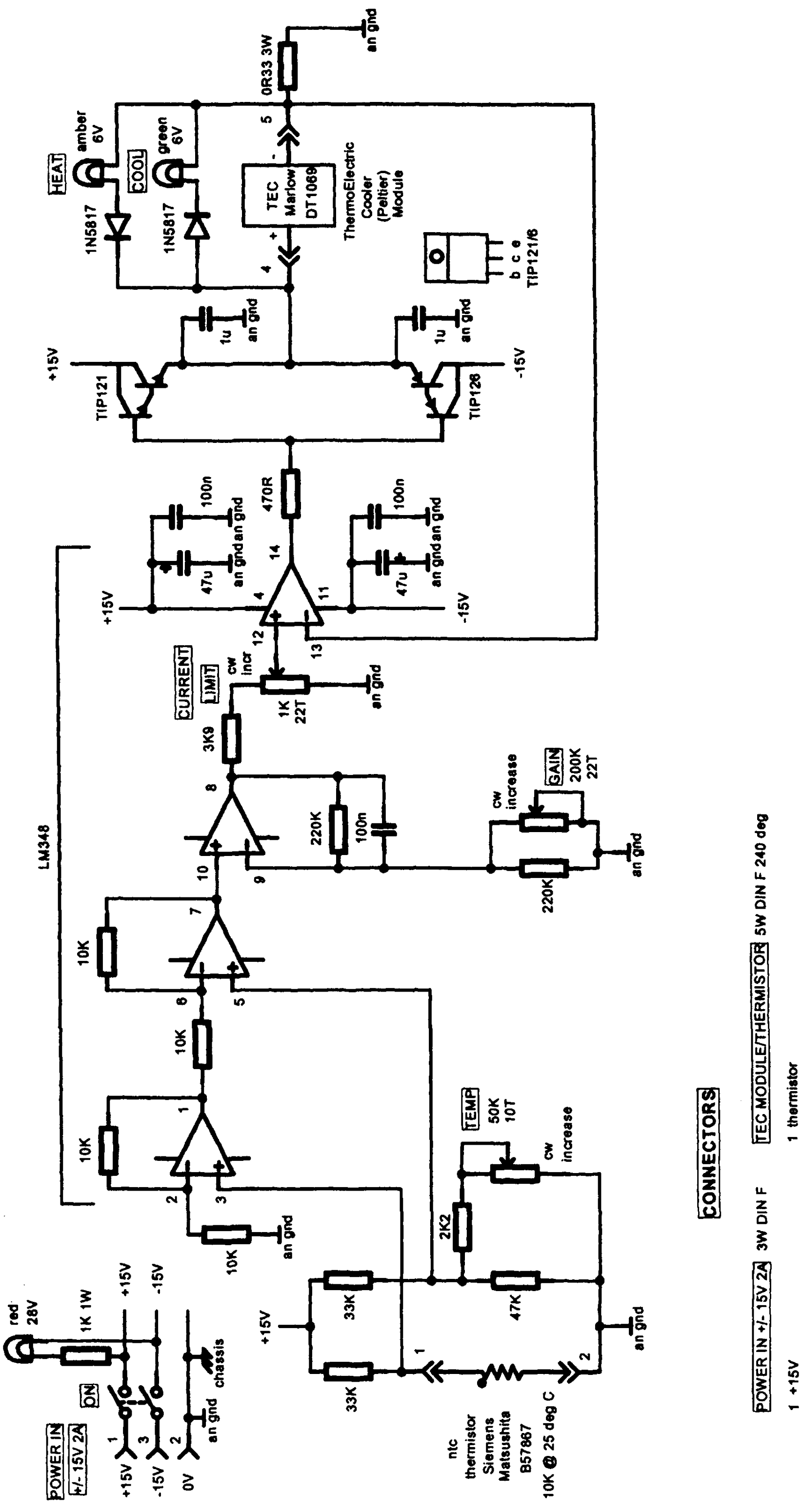

Figure 2.2: Circuit Diagram for the Microscope Temperature Controller.

A sample of the emulsion was put on the microscope slide (all slides and coverslips from Agar Scientific, UK) on the temperature controller and the slide temperature was recorded using a thermocouple at the end of each experiment, allowing for any changes in temperature due to extra heating from the microscope lamp. The thermocouple was also fixed to the top of the slide to compensate for any differences between the temperature selector and the emulsion sample, and for all sizing experiments the selector was set at 15 ± 0.2 °C.

Using the video camera and data capture software, images of the emulsion could be recorded and from these, the average drop volume was calculated. This was done using a calibrated size standard of 5.0 μm ± 0.05 μm Polymer Microspheres in water (Duke Scientific Corporation, USA) (Figure **2.3a**).

Due to the nature of the emulsion, the diffraction pattern of individual drops changed according to the focal plane and so, for accuracy, the sizing images were taken when the drops appeared with the same diffraction pattern. To calculate an average volume and hence error from the standard deviation, three different images of each sample were recorded and analysed. This gave on average 6 individual drops in total for each sample. Figure **2.3b** shows a typical image of the emulsion used to calculate the drop volume.

The number density of the emulsion was determined using a haemocytometer (non–metallised Improved Neubauer; Hawksley & Sons Ltd., UK) with a grid of 1/400 mm^2 x 0.1 mm depth etched onto the surface. By placing a sample of the emulsion on the haemocytometer, the number of drops per square could be counted under the microscope and then scaled to give a value for drops per cm^3. A typical image is shown in Figure **2.3c**. To obtain an average of six values for the number density per cm^3, three images of each sample were taken and the standard deviation was used as the error.

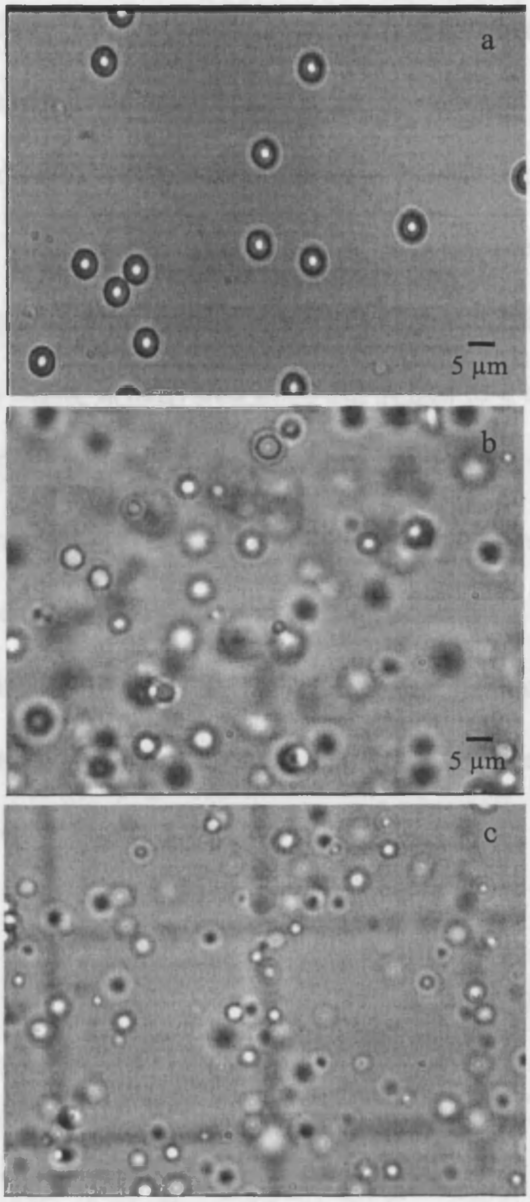

Figure 2.3: Typical images from optical microscopy experiments to measure Drop volume (b) and Number density (c) An image of the calibration polymer microspheres used for size calibration is also included (a). All images were taken with the same magnification.

2.7 Small Angle Neutron Scattering (SANS) Experiments

The SANS experiments were carried out using three different diffractometers; LOQ at the ISIS facility (Didcot, UK) and D22 and D11 at the Institute Laue–Langevin (ILL) (Grenoble, France).

The first set of experiments were done at the ISIS pulsed neutron source (CCLRC Rutherford Appleton Laboratory) using the LOQ diffractometer. The neutrons are produced by using spallation of nuclei in a high atomic number target, i.e. an 800 MeV, 200 μA proton beam, is delivered in 50 Hz pulses to a tantalum target cooled by heavy water [177]. Cryogenic moderators are then used to slow the neutrons. LOQ is a fixed–geometry instrument and so uses pulses of neutrons of wavelengths 2.2 to 10 Å, separated by time–of–flight and recorded at a 64 cm^2 two–dimensional ^{3}He gas detector. This was positioned 4.1 m from the sample and the sample was placed in a thermostatted cell–holder set at 25 ^{o}C. A schematic diagram of the diffractometer is shown in Figure **2.4** [178].

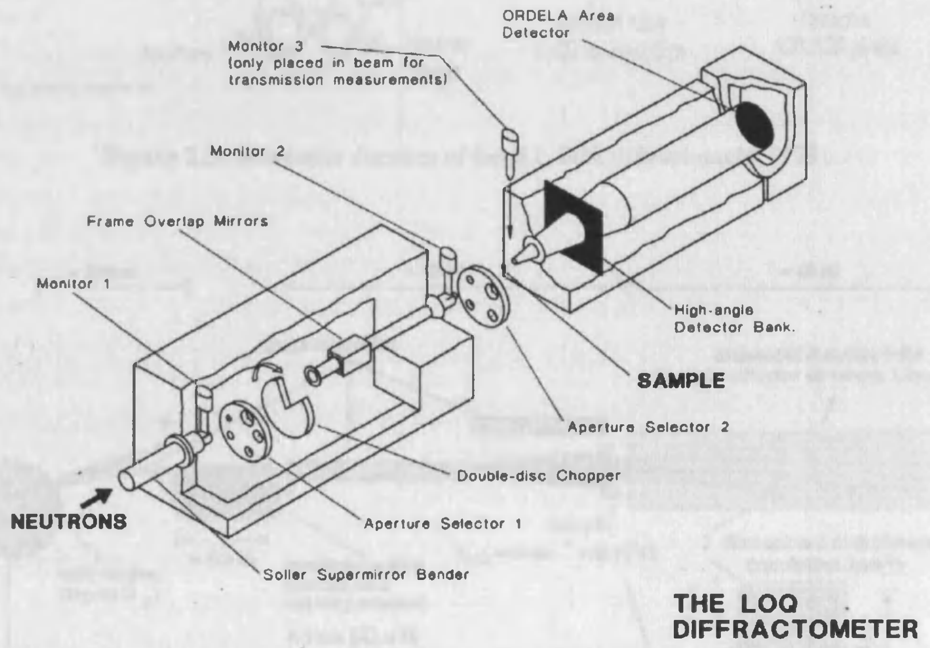

Figure 2.4: Schematic diagram of the ISIS LOQ diffractometer [178].

The scattering vector *Q*–range obtained was 0.008 to 0.22 Å^{-1}, with a 12 mm diameter neutron beam. Once collected, the raw data was reduced by making wavelength–dependent corrections, to allow for the incident spectrum shape, detector efficiencies and measured sample transmissions [177]. Data collection and reduction was done using standard ISIS programs.

The next two sets of SANS experiments were carried out at the ILL D22 and D11 diffractometers respectively. Here the neutron beam is produced from a reactor source with a 93 % ^{235}Uranium fuel element, and cryogenic moderators are again used to slow the neutrons. Schematic diagrams of the two diffractometers are shown in Figure **2.5** and **2.6** [179].

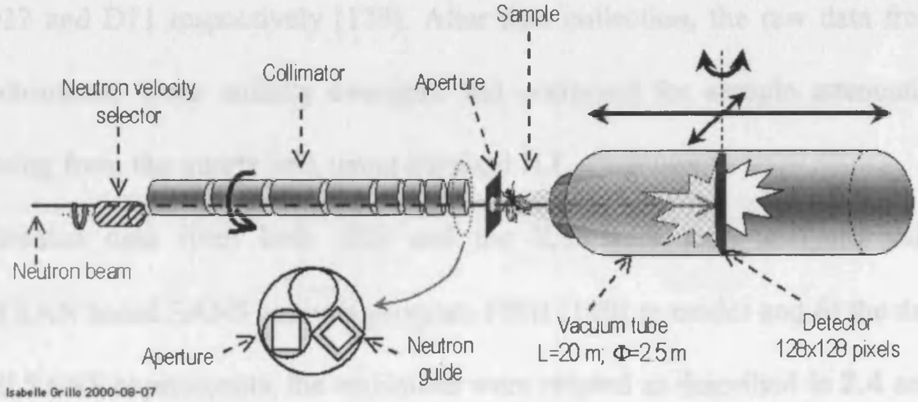

Figure 2.5: Schematic diagram of the ILL D22 diffractometer [179].

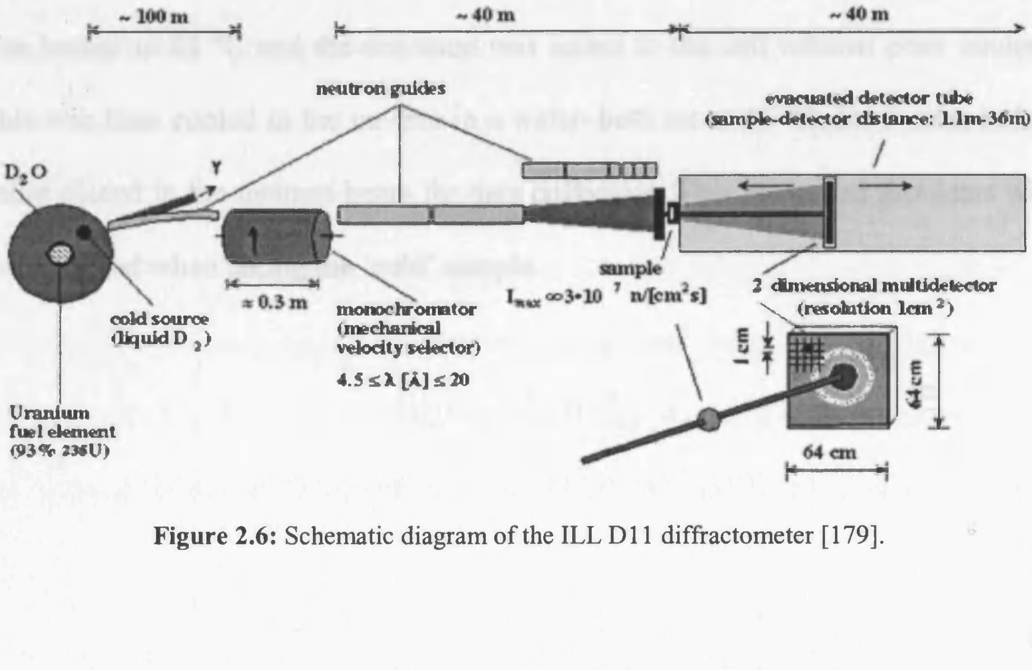

Figure 2.6: Schematic diagram of the ILL D11 diffractometer [179].

Both D22 and D11 are fixed–wavelength instruments and these were set–up at λ_{D22} = 15 Å and λ_{D11} = 13 Å for the experiments. The neutron scattering from the sample was recorded on two–dimensional ^{3}He gas detectors, with D22 having a 96 cm^2 and D11 having a 64 cm^2 detector surface–area [179]. These were mounted on movable stages to allow more than one sample–detector distance to be used and enabled a larger *Q*–range to be measured with each experiment. Two sample–detector distances were used for both diffractometers; 3 m and 17.6 m to give a *Q*–range of 0.001 to 0.125 Å^{-1} for D22 and 8 m and 34 m to give a *Q*–range of 0.0006 to 0.022 Å^{-1} for D11. The samples were placed in a thermostatted cell–holder set at 15 °C for both diffractometers and the circular beam aperture diameters were 16 and 14 mm for D22 and D11 respectively [179]. After data collection, the raw data from both diffractometers were radially averaged and corrected for sample attenuation and scattering from the quartz cell, using standard ILL programs.

The treated data from both ISIS and the ILL were then analysed using the FORTRAN based SANS analysis program FISH [180] to model and fit the data.

For all SANS experiments, the emulsions were created as described in **2.4** and, after cooling for 30 mins (LOQ and D22), a sample was placed in a 2 mm or 1 mm pathlength circular Far–UV quartz cuvette (Hellma UK Ltd). For D11, the cuvette was heated to 65 °C and the emulsion was added to the cell without prior cooling. This was then cooled in the cuvette in a water–bath set at 15 °C, for 5 mins before being placed in the neutron beam for data collection. This prevented problems with shear caused when taking the 'cold' sample.

2.8 Other Equipment

Another method employed to create an emulsion, was done using the 'Avanti Mini–Extruder' (Avanti Polar Lipids Inc., USA) [181] A schematic diagram of the Mini–Extruder is shown in Figure **2.7.**

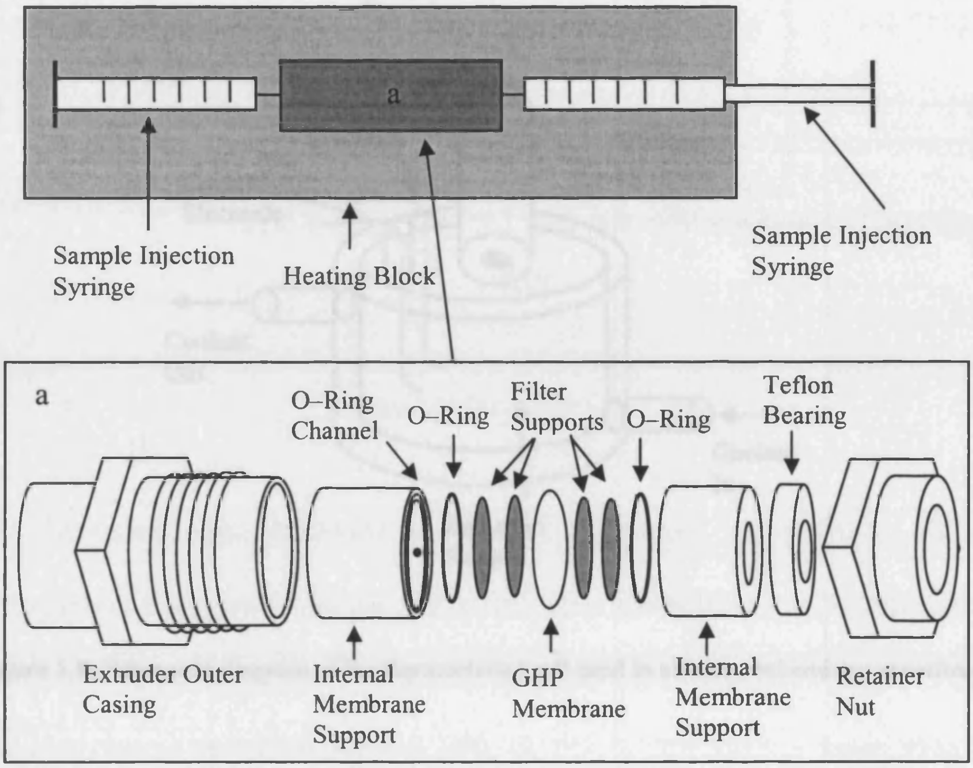

Figure 2.7: Schematic diagram of the 'Avanti Mini–Extruder' [181]

25 mm hydrophilic polypropylene (GHP) membrane filters (Pall Gelman Laboratories, UK) with a pore size of 0.45 µm, were used in the Mini–Extruder to create the emulsion and the filter supports used were those supplied with the Extruder (polyethylene drain discs, 10 mm) (Whatman Nucleopore; UK).

Cyclic Voltammetry (CV) and Rotating Disc Electrode (RDE) (Oxford Electronics, UK) electrochemistry experiments were carried out using a platinum working electrode (Oxford Electronics, UK) with a 0.36 cm^2 working area, platinum wire as the counter electrode (Johnson Mathey; 99.99 %) and a silver/silver chloride electrode (BAS, UK) as the reference. These were connected to a PC software–controlled potentiostat (Autolab; Windsor Scientific, UK) and a thermostatted cell was custom–made (built in–house; J. Hughes, Figure **2.8**: schematic diagram) to accommodate the sample, working, reference and counter electrodes.

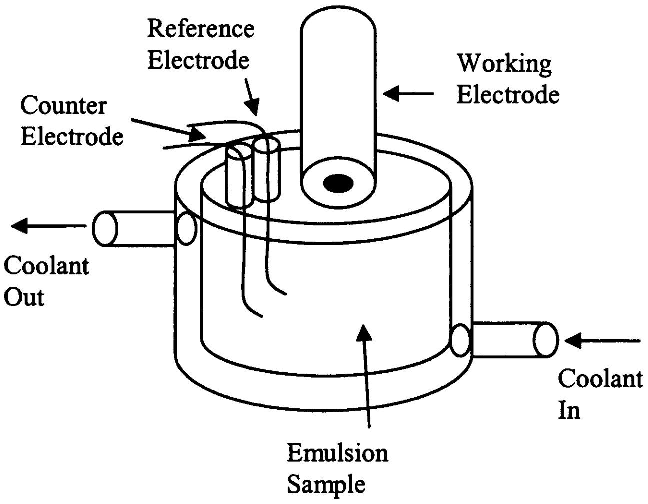

Figure 2.8: Schematic diagram of the thermostatted cell used in all electrochemistry experiments

This was connected to the water bath to maintain the temperature of the emulsion during the experiments.

The electrode was polished using 1.0 μm and then 0.3 μm grade alumina (Buehler, USA) on a polishing pad (Kemet, UK) in a 'figure–of–eight' motion. This was then rinsed with pure H_2O and cleaned using potential cycling in 0.1 M sulphuric acid from –0.3 to +1.3 V. The potential was cycled successively until a defined voltammogram was obtained (Figure **2.9**).

For the acid cycling, the counter electrode was platinum wire and the Standard Calomel Electrode (SCE) was used as the reference.

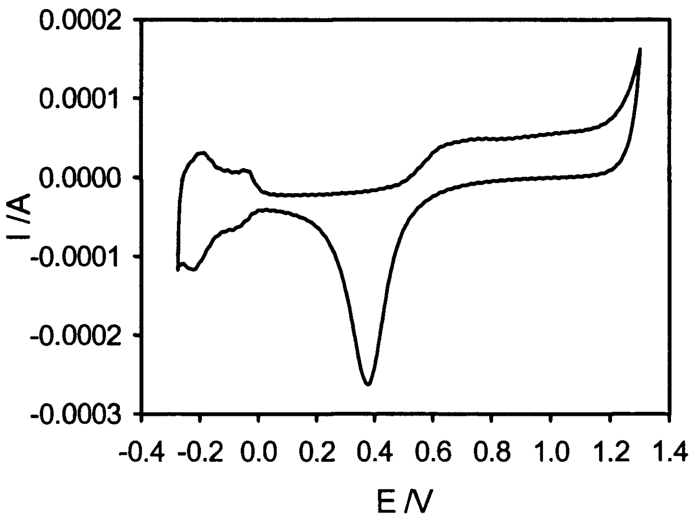

Figure 2.9: Typical cyclic voltammogram for a clean platinum working electrode used in all electrochemistry experiments

Light Scattering was employed in various techniques to determine different information. To measure the drop size and size distribution, a laser backscatter technique (Optical Reflectance Measurement (ORM) Particle Size Analyser) (MTS, Germany), using the thermostatted cell in Figure **2.8**, and a laser diffraction technique (Mastersizer 2000) (Malvern Instruments Ltd., UK) were used.

The backscatter technique works by focusing a laser beam through a lens to create a very small focal point of high intensity [182]. The lens is then rotated, at a known velocity, to give a circular scanning beam. When this beam intercepts a drop, light is backscattered and can be recorded on a detector behind the lens, and because both the scanning velocity and time of the backscattering are known, and the probability of the beam hitting any part of the drop is equal, characteristic lengths are determined for the sample being probed. These are termed chord lengths rather than the drop diameter but the data is then converted from chord distributions into drop diameter distributions.

The laser diffraction technique, however, measures the drop diameter by using an expanded He–Ne laser beam (9–18 mm beam width) [183]. This is shone through the sample and, as the drops pass through the beam, they scatter light. At small forward angles, this scattering is predominantly diffraction and this is detected by a set of concentric detectors placed at the focal point of a Fourier transform lens. This means that the detector only measures light scattered at a specific angle, which is independent of the position in the sample of the drops, and calculates the drop diameter.

Other laser diffraction instruments were also used to measure the zeta–potential at the oil–water interface, namely a Coulter DELSA 440SX (Beckmann Coulter Laboratories, UK) and a Zetasizer 3000 (Malvern Instruments Ltd., UK). All the light scattering techniques investigated were PC software–controlled.

To analyse the electrodeposited samples, Scanning Electron Microscopy (SEM) with X–Ray diffraction (EDAX) (15kV; JEOL, UK) and Electron Microscopy X–Ray Analysis (EMXA) (Super Probe JXA–86000serie; Electron Probe X–Ray Microanalysers, JEOL, UK) were used with PC controlled software. The samples were mounted on either aluminium with a conducting self–adhesive tab, or pure carbon stubs (all Agar Scientific, UK).

Chapter 3: Creation and Characterisation of an Oil–in–Water Emulsion

3.1 Introduction

The creation of an emulsion of 1,2–dichloroethane (DCE)–in–water using a Condensation Technique is described and this technique has been optimised to give the conditions needed to produce reproducible emulsions with comparable drop volumes and number densities. These have been measured using optical microscopy and light scattering techniques to characterise the emulsion and to investigate how the drop volume, and hence the solubilities of the two phases, are dependent on temperature.

3.2 Emulsion Creation

To create a surfactantless emulsion of 1,2–dichloroethane (DCE)–in–water, different methods were investigated, with the most successful procedure being a *Condensation Technique* [135]. This uses the manipulation of the solubility of the DCE phase in the water, illustrated in Figure **3.1**.

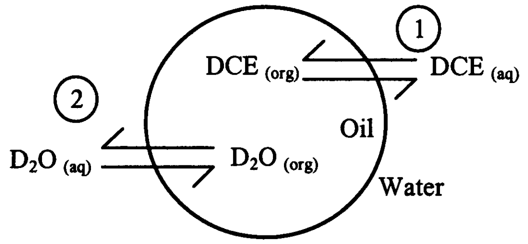

Figure 3.1: Schematic diagram of a DCE drop in water showing the dynamics of solvent exchange, schemes 1 and 2.

Figure **3.2** shows the literature solubility of DCE in water at different temperatures and it can be seen that the solubility of the DCE in water increases with temperature, and so as the two liquids are heated, the DCE dissolves into the water. The literature data has been regression fitted using the equation: y=0.8+0.06exp$^{0.03x}$.

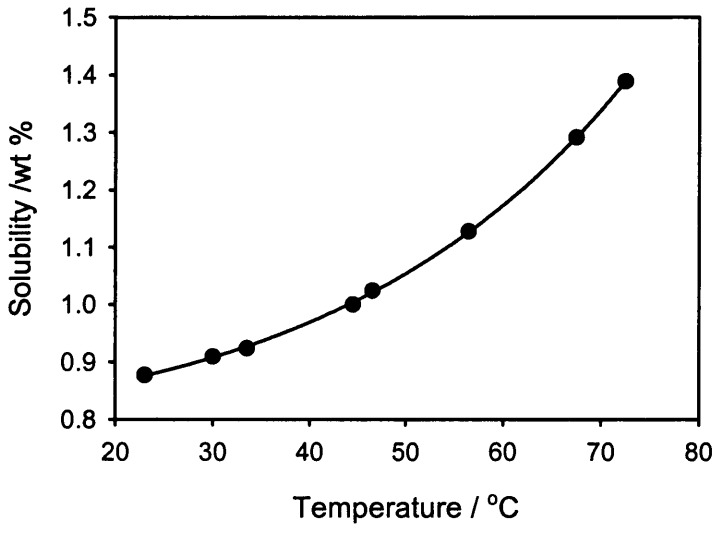

Figure 3.2: Solubility plot of DCE in H_2O determined between 23–73 °C [184]. The solid line corresponds to the regression fit using the equation: y=0.8+0.06exp$^{0.03x}$.

Conversely, as the solution is cooled rapidly, the solubility of the DCE in water decreases and the DCE condenses out of solution as emulsion drops. From Figure **3.2** and using the equation for the regression line, it can be determined that when a mixture of DCE and water is heated to 65 °C, 1.25 wt % of DCE is dissolved in water, and then after it is cooled to 15 °C, 0.85 wt % of DCE remains dissolved. This leaves 0.4 wt % of DCE supersaturating the water that will condense out of solution to form small emulsion drops at nucleation sites [112]. Table **3.1**, shows the solubility weight percent of DCE dissolved in water at different temperatures, and the calculated weight percent of DCE present as emulsion drops when the emulsion is heated to 65 °C and then cooled to temperatures in the range 55–5 °C.

Temperature / °C	**Solubility /wt %**	**wt % DCE drops**
65	1.25	–
55	1.11	0.14
45	1.01	0.24
35	0.94	0.31
25	0.88	0.37
15	0.85	0.40
5	0.82	0.43

Table 3.1: Showing the solubility weight percent of DCE in water at different temperatures [184]. Also included is the calculated wt % of DCE present as drops when the emulsion is heated to 65 °C and cooled to temperatures in the range 55–5 °C.

As described in **1.2.3**, the D_2O becomes supersaturated with DCE as the mixture is heated, and therefore when the temperature is rapidly decreased, the excess DCE condenses out as drops. The nucleation sites form simultaneously in a finite period of time and then the drops grow at a constant rate limited by radial molecular diffusion [112]. Ostwald ripening, introduced in **1.2.2** as emulsion destabilisation caused by the growth of larger emulsion drops at the expense of smaller ones, therefore has a negligible effect and is ignored for an emulsion formed using this technique. A proposed mechanism for the emulsion nucleation and growth is described in Figure **3.3**.

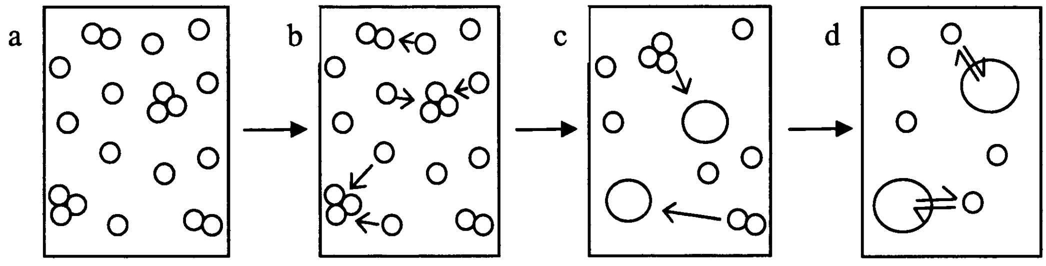

65 °C, t =0 s　15 °C, t =5–10 s　15 °C, t =10–100 s　15 °C, t >100 s

Figure 3.3: A proposed scheme for emulsion nucleation and growth when created using a Condensation Technique. A mixture of DCE and water are heated to 65 °C and the DCE dissolves into the water as 'free' molecules and 'clusters' of 2–3 molecules (a). This mixture is then cooled to 15 °C, and clusters of 3–4 DCE molecules form nucleation sites over a finite time (b). These then attract free molecules of dissolved DCE, via molecular diffusion, to create an emulsion DCE drop, and the drops then grow by attracting other smaller clusters of dissolved DCE (c) eventually setting up an equilibrium between the DCE drop and the aqueous dissolved molecules of DCE (d).

In Figure **3.3**, it is proposed that when a mixture of DCE and water are heated to 65 °C, the DCE dissolves into the water. The DCE molecules will be dispersed in the aqueous solution, not only as free molecules but also as clusters of 2–3 molecules (Figure **3.3a**). If, for example, a nucleation site corresponds to a cluster of 3 or 4 DCE molecules in aqueous solution [136], when the mixture is cooled to 15 °C, these DCE clusters will spontaneously nucleate to reduce the concentration of the supersaturated DCE–in–water solution. Other DCE molecules will also form clusters and nucleate over a finite period of time (Figure **3.3b**). These nucleation sites will then attract the free aqueous dissolved DCE molecules and grow via molecular diffusion, to create a DCE drop [112] (Figure **3.3c**), eventually setting up an equilibrium between the DCE drop and the aqueous dissolved DCE (Figure **3.3d**). In turbidity experiments using the UV–Vis spectrophotometer, a sharp peak with a scattering >3.5 au was repeatedly seen <200 nm when the emulsion was scanned from 190–1100 nm, shown in Figure **3.4**.

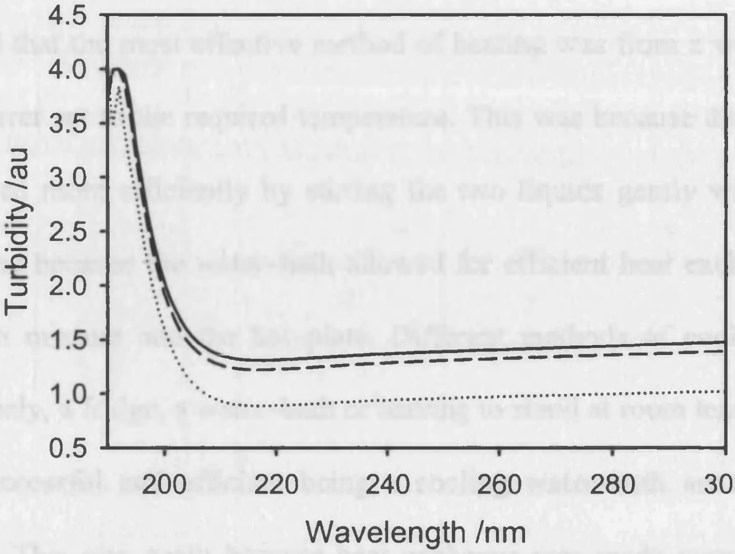

Figure 3.4: Graph showing the turbidity vs. wavelength from 190–300 nm for an emulsion containing DCE–in–1.5 M sucrose D_2O, illustrating the sharp 'scattering' peak seen <200 nm. The different plots correspond to measurements taken at different times; (——) initial scan, (------) after 10 mins, and (·······) after 1 hour.

This sharp saturated peak seen in Figure **3.4** occurred for all emulsion samples that were placed into the spectrophotometer at 65 °C and then allowed to cool to 15 °C in the beam, while the turbidity was measured. The magnitude of this peak was seen to be at the saturation limit of the UV-Vis absorbance over the first 10 mins while the emulsion formed, and this then decreased slowly as the emulsion destabilised. This peak was also present in a sample of D_2O saturated with DCE at 15 °C and is thought to correspond to the clusters of DCE molecules dissolved in the aqueous phase. The saturated maximum and then steady decrease in the scattering of this peak would then be due to the aqueous dissolved DCE molecules forming clusters and then growing to form emulsion drops. The absorbance of this peak is still quite high after 1 hour due to the presence of DCE still dissolved in the aqueous phase at 15 °C.

To heat the emulsion mixture, both an oven and a water–bath were investigated, but it was found that the most effective method of heating was from a water–bath on a hot–plate/stirrer set to the required temperature. This was because the liquids could then be mixed more efficiently by stirring the two liquids gently with a magnetic stirrer bar and because the water–bath allowed for efficient heat exchange between the emulsion mixture and the hot–plate. Different methods of cooling were also studied; namely, a fridge, a water–bath or leaving to stand at room temperature; with the most successful and efficient being a cooling water–bath set to the desired temperature. This was again because heat exchange was made more efficient and therefore maintained a steady rate of cooling.

To determine the length of heating time needed to create a reproducible emulsion of DCE–in–water, a mixture of DCE and 1.5 M sucrose in D_2O were heated to 65 °C for different, recorded solubilisation times and then cooled to 15 °C for 30 mins. D_2O and sucrose were used to reduce the rate of sedimentation and hence improve the stability of the emulsion for this experiment. This is described fully in **4.2**, and the procedure for forming the emulsion is outlined in **2.4**. A sample from each emulsion was then taken and the turbidity was measured using a UV–Vis spectrophotometer, and the average drop volume and number density were recorded using optical microscopy, as outlined in **2.6**. The results are shown in Figure 3.5.

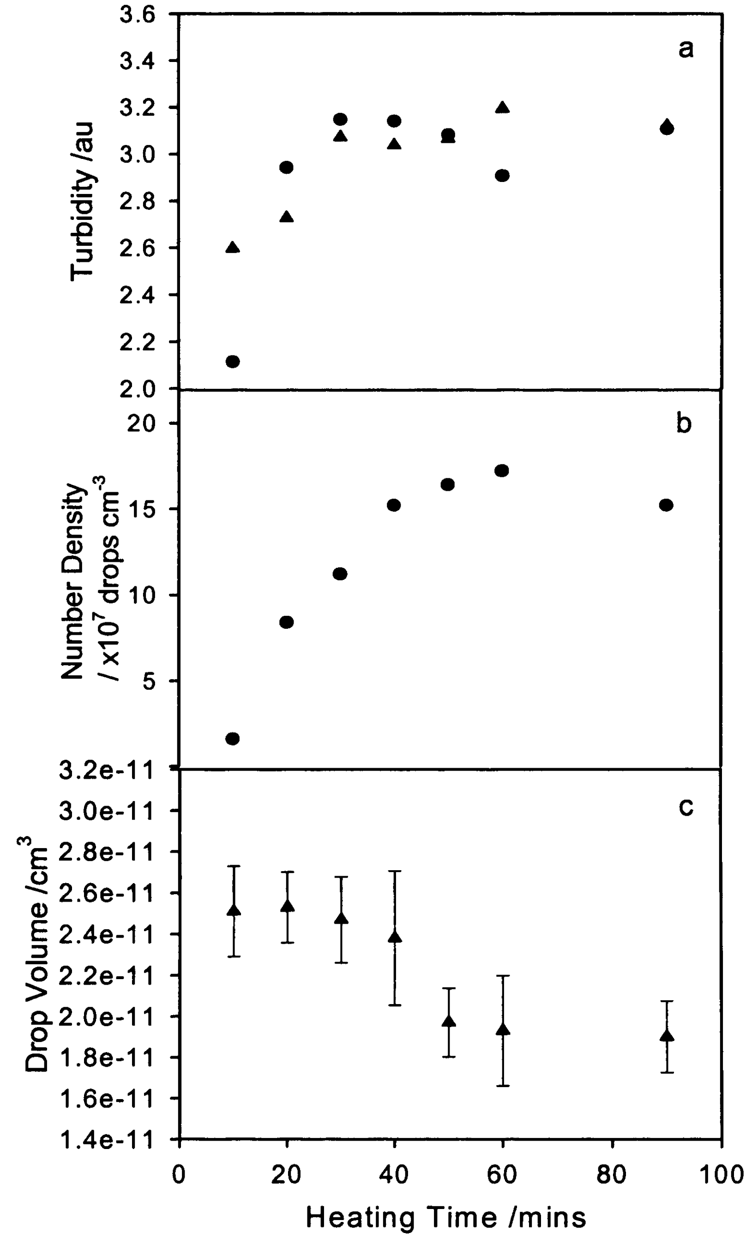

Figure 3.5: Turbidity measured at 550 nm (a), Number of drops per cm^3 (b) and Drop volume (c) vs. heating, or solubilisation, time for an emulsion of DCE–in–1.5 M sucrose D_2O only. The different symbols used in (a) correspond to two different experimental data sets and each data point shown for all plots, was determined from a different emulsion created as described. Sucrose was included in these experiments to reduce the rate of sedimentation and improve stability, and will be discussed further in **4.2**.

From Figures **3.5a** and **b**, it can be seen that the turbidity and number density of the emulsion follow a similar trend and reach a plateau after 1 hour of solubilisation time; illustrating the link between the turbidity and the number density of the emulsion. Figure **3.5c** plots the average drop volume of the emulsion against solubilisation time and from this it can be seen that there is a very slight decrease in the drop volume as the solubilisation time is increased. This also reaches a plateau after 1 hour, and may be due to the emulsion becoming more reproducible.

Using the relationships,

$$N \times V_{av} = V_t \qquad \textbf{3.1}$$

and,

$$W = \frac{V_t M_{Vi}}{V_i} \times 100 \qquad \textbf{3.2}$$

Where N is the number of drops per cm^3, V_{av} is the average drop volume in cm^3, V_i is the initial volume and V_t is the total volume, in cm^3, of DCE present as emulsion drops, M_{Vi} is the gravimetric mass of the initial volume, the total weight percent of DCE (W), present in the emulsion samples as condensed drops, can be calculated from the drop volume and number density. This is plotted in Figure **3.6** for an emulsion mixture that has been heated to 65 °C and then cooled to 15 °C, and it can be seen that the weight percent of DCE condensed as drops, also reaches a plateau after 1 hour of solubilisation time, reaching a value of approximately 0.4 wt %. This supports the literature data seen in Figure **3.2**, verifying that the aqueous phase of the heated emulsion sample is saturated with DCE after 1 hour.

The turbidity was also plotted against number density, and this can be seen in Figure **3.7**, where the fitted regression line shows that there is linear relationship between the two and therefore the turbidity can be used as a measure of emulsion destabilisation.

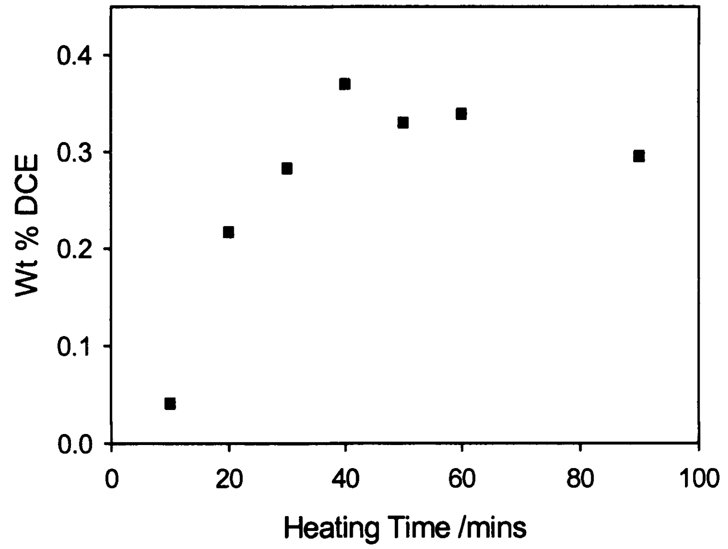

Figure 3.6: Total DCE wt % present as condensed emulsion drops, calculated from the average drop volume and number density from Figure **3.5b** and **c**, vs. solubilisation time for an emulsion of DCE–in–1.5 M sucrose D_2O only.

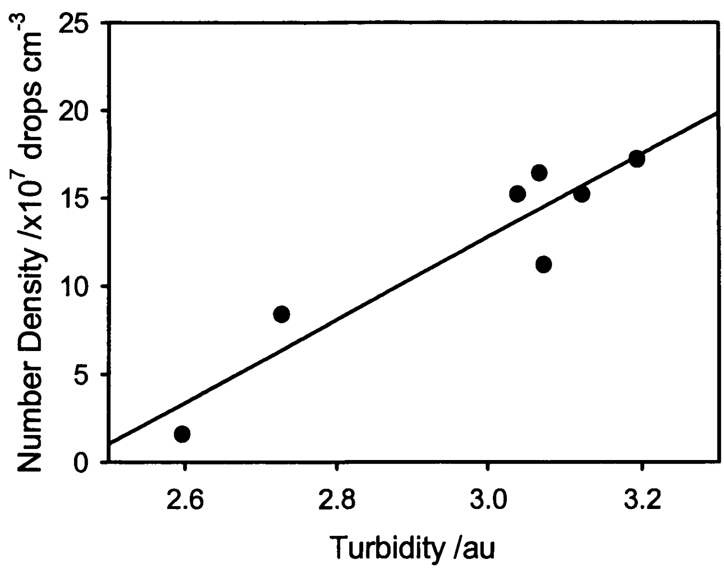

Figure 3.7: Graph plotting the emulsion number density vs. turbidity to illustrate the linear relationship between the two. The equation for the fitted regression line is y=24x-58.

Other methods investigated for creating the emulsion, were shaking by hand, mechanical agitation, and sonication. But these led to emulsions that were inhomogeneous with a large size distribution and, with sonication in particular, an emulsion that consisted of both DCE–in–water and water–in–DCE drops. This phenomenon is termed a 'multiple' or 'double' emulsion [124] and was also seen to occur when the emulsion was created using an "Avanti Mini–Extruder" [181]. This is commonly used in the creation of unilamellar vesicles [185] and it was proposed that it could be used to make a homogenous emulsion. A schematic diagram of this is shown as Figure **2.7** in **2.8** and was set–up so that one syringe was filled with DCE and the other with water. One phase would then be pushed through the membrane into the other, and it was proposed that the extruder would create an emulsion that consisted of a uniform drop volume, similar to the pore size of the membrane used [185]. In practise, the Mini–Extruder could produce an emulsion that was relatively more stable than one created using a condensation technique, but proved to an unreliable method for emulsion formation. The turbidity versus time for emulsions created using the Extruder and condensation technique are shown in Figure **3.8**, where the data has been normalised for easier qualitative comparison. This was because the emulsions were created using different methods causing the number densities, and therefore turbidities to be significantly different, making them hard to compare. The original turbidity values were 0.91 and 1.26 a.u., for the emulsion formed using the 'Avanti' mini–extruder and one formed using a condensation technique, respectively.

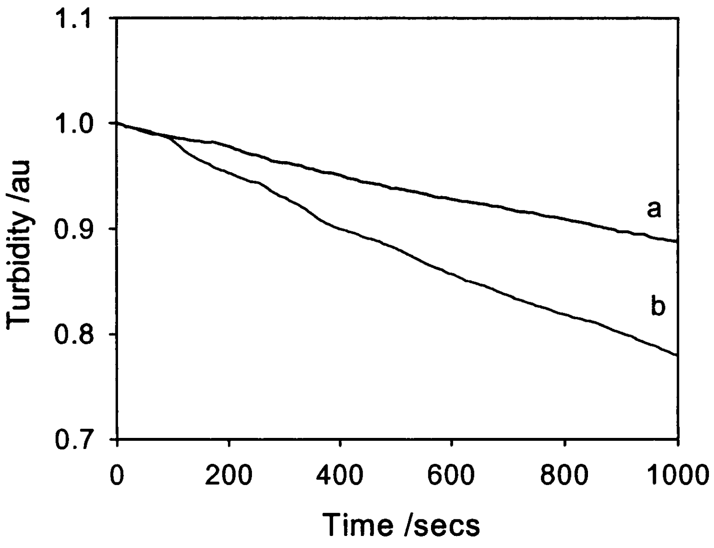

Figure 3.8: Graph showing the turbidity at 550 nm vs. time of DCE–in–D_2O emulsions formed using (a) the 'Avanti' mini–extruder and (b) a Condensation Technique. The original turbidity values were 0.91 and 1.26 au, and the rate of change of turbidity with time for the lines are –90.7 and –179.8 x10^{-6} au s^{-1} for the emulsion formed using the extruder and condensation methods respectively.

Even though Figure **3.8** suggests that the extruder method created an emulsion that had a lower change in turbidity with time, –90.7 x10^{-6} au s^{-1} compared with –179.8 x10^{-6} au s^{-1}, the extruder proved to be an unreliable technique. This was due to frequent problems from leaking syringes, caused by the high pressure at the internal membrane, and rapid coagulation of the DCE after it had been pushed through the extruder into the water phase, resulting in a single drop of DCE in water containing a suspension of fine water drops.

There were also problems encountered when removing the emulsion from the injection syringes. The emulsion experienced a high degree of shear when pushed through the syringe needle, and this increased the rate of coalescence of the emulsion drops. When stabilising agents were added, namely sucrose or potential–

determining salts, these were seen to precipitate from the solution when pushed through the extruder membrane.

Due to these problems, it was determined that emulsions created using the condensation technique, i.e. heated to 65 °C for 1 hour and then cooled to a lower temperature for 30 mins, were more reproducible with respect to drop volume and number density, and were easier to produce and analyse.

3.3 Emulsion Characterisation

3.3.1 Optical Microscopy Experiments

The emulsion drop volume and number density were determined using optical microscopy, as outlined in **2.6**. Transmission illumination, was used because it gave sharper images with the most distinguishable interface, than top or side illumination. Because DCE and water have similar refractive indices, 1.333 and 1.445 (at 20 °C, 589 nm [186]) respectively, the drops were hard to distinguish in the water phase under the microscope using top and side illumination, and therefore it was hard to determine the interface. With transmission illumination, however, the interface was seen as a 'shadow' and gave rise to different diffraction patterns. This pattern changed according to the focal plane, Figure **3.9**, and so, for accuracy, sizing images and measurements were taken of drops with the same diffraction pattern (d) (see also **2.6**, Figure **2.3**).

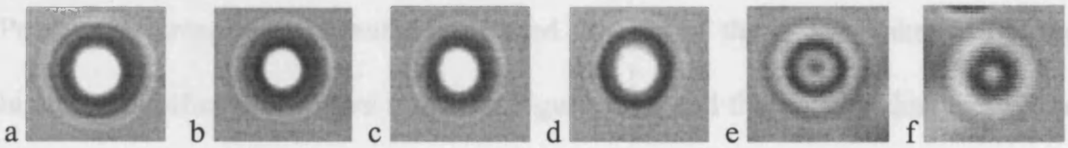

Figure 3.9: Images of an emulsion drop, (a–f), showing some of the different diffraction patterns observed. The diffraction pattern shown in (d) was chosen as showing the sharpest interface and only drops seen with this pattern were measured.

To try and improve the microscope images, and make the drops more visible in solution, the use of oil and water–soluble dyes were attempted. These were still however partially soluble in the other liquid and so did not give a visibly sharp interface. Different slides were also tested, namely mirrored and black slides, but without success, and there were also problems arising from the DCE drops adhering to the hydrophobic glass slide and coverslip and therefore giving a 'false' size. To overcome this, 'cavity' slides and a slide with a 'fused–ring' in the centre, were tested. These had a circular hollow in the centre and so allowed for a larger sample volume to be studied. Neither of these proved to be successful however because, even though there was an increase in sample volume, this led to there being a higher number density of drops in the sample and so it was harder to distinguish individual drops. To ensure that only emulsion drops that were free in solution were measured, images were only taken of drops that were seen to be moving and not static. The temperature of the emulsion also needed to be maintained and controlled, i.e. when a sample of emulsion at 15 °C was placed on a slide at room temperature, problems arose from the sudden change in temperature. This was solved by the use of a peltier device, shown in **2.6** as Figure **2.1**, to maintain and control the slide temperature and was positioned on the stage of the microscope.

To calculate the average drop volume, calibrated size standards of 5.0 μm ± 0.05 μm Polymer Microspheres in water were used. Images of these were taken under the highest magnification, shown in **2.6** as Figure **2.3a**, and the average diameter of the spheres was measured. By measuring the diameter of the emulsion drops under the same magnification and comparing this with the measured diameter of the size standard, an accurate value for the volume of the emulsion drops was calculated.

The number density, of drops per unit volume of the emulsion, was calculated using an optical microscope and a Haemocytometer slide. This was a specially designed cell, commonly used to count blood cells, and consisted of a slide with an etched grid in the centre. Each square in the grid was of a known dimension and so, by counting the number of drops in one square, this number could be scaled up to give the number of drops per unit volume, as described in **2.6**.

To characterise the emulsion, a mixture of DCE–in–1.5 M sucrose D_2O, was prepared, as in **2.4**, and a sample of the emulsion was put on a microscope slide on the Peltier device, set at 15 °C. The initial drop volume and number density were measured whilst the flask containing the bulk emulsion solution was maintained at 15 °C in the water bath for subsequent samples. Measurements of the initial drop volume were recorded as outlined in **2.6**, and then fresh samples from the bulk emulsion were taken every hour for 5 hours. The change in drop volume with time can be seen in Figure **3.10**, and it can be seen that the drop volume increased linearly, doubling after 2 hours.

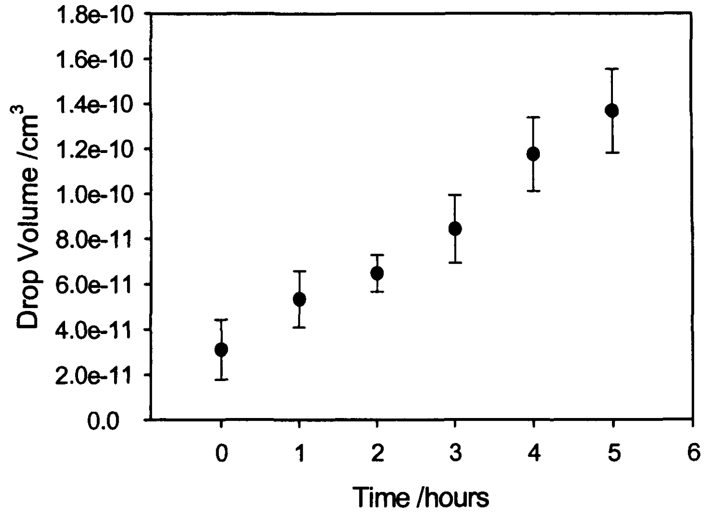

Figure 3.10: Change in drop volume with time for a DCE–in–1.5 M sucrose D_2O emulsion system.

The number density of the emulsion was also measured every hour in this experiment; however, due to the high vapour pressure of DCE, as every sample was removed, the DCE in the headspace of the vessel was also released. As a result the number density, and thus the volume fraction of DCE in the emulsion, was reduced falsely by a destabilising factor other than sedimentation or coalescence. This was also seen to be true for the drop volume, and so an experiment was performed where the drop volume and number density were measured initially and then again after 20 hours. The flask was not reopened during this time and the results show that, for an emulsion of DCE–in–1.5 M sucrose D_2O, heated to 65 °C and cooled to 15 °C, the initial drop volume was 25 ±5 μm^3 and after 20 hours, this increased to 180 ±4 μm^3. The initial number density was found to be 140 ±12 $x10^6$ drops per cm^3 and after 20 hours and this decreased to 7 ±6 $x10^6$ drops per cm^3 (this error seems to be large due to extensive emulsion destabilisation, resulting in only 3 ±3 drops being counted per square of the Haemocytometer). The value for the drop volume after 20 hours is similar to that obtained after 7 hours by extrapolating Figure **3.10**, and this suggests that by opening the flask and releasing the headspace every hour, the rate of destabilisation of the emulsion was accelerated. Figure **3.10**, still shows, qualitatively, how the emulsion destabilises over time and from calculations using the data for the drop volume measured initially and after 20 hours, the volume is seen to double after 7 hours instead of after 2 as suggested by Figure **3.10**.

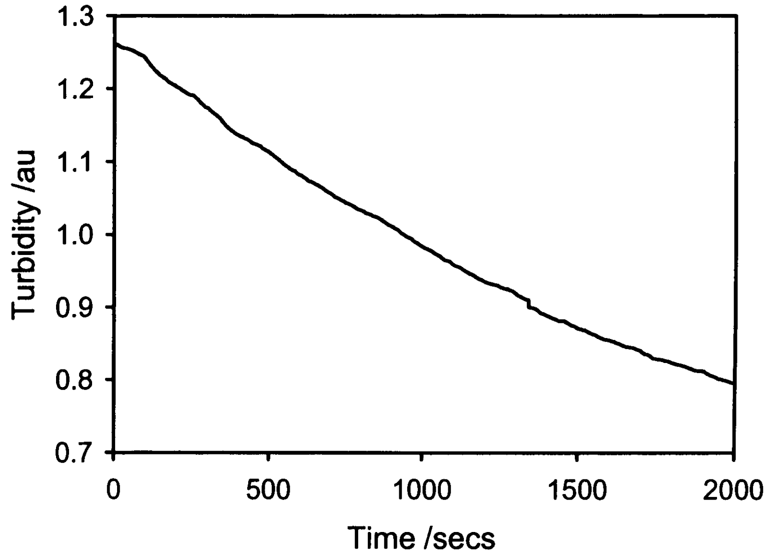

Figure 3.11: Graph showing turbidity at 550 nm vs. time for an emulsion containing DCE–in–1.5 M sucrose D_2O. The change in turbidity with time is $-179.8\ x10^{-6}$ au s^{-1}.

By looking at the change of the turbidity with time, as described in **2.5**, for an emulsion of DCE–in–1.5 M sucrose D_2O, Figure **3.11**, it can be seen that this also decreases with time, -179.8×10^{-6} au s^{-1}, showing the link between the drop volume and number density with emulsion turbidity.

3.3.2 Light Scattering Experiments

Surfactant stabilised emulsions are conventionally characterised using light scattering techniques involving analysis using Mie Theory, using the dependence of the complex scattering from a large sphere, on the scattering angle [112]. To determine the emulsion drop volume and size distribution, a variety of light scattering techniques were investigated, as described in **2.8**, but initial backscatter methods and subsequent experiments using a conventional laser light scattering emulsion sizer proved inconclusive. Results from the laser backscatter method recorded a drop diameter of 6 ±3 μm irrespective of temperature. The technique, however, involved stirring of the sample, in the thermostatted cell (**2.8**, Figure **2.8**), using a magnetic stirrer bar and this was seen to rapidly destabilise the emulsion due to the increase in shear. The results were therefore believed to be inconclusive and unreliable and so a conventional laser light scattering technique was tested.

As described in **2.8**, this conventional light scattering technique was done using a Mastersizer 2000, used at room temperature, 25 °C. An emulsion was created, following the procedure in **2.4**, composed of 100 cm^3 H_2O and 1 cm^3 DCE. Also included were, 0.1 M tetraethylammonium chloride (TEACl) in the water and 1 mM tetraethylammonium tetraphenylborate (TEATPB) in the DCE phase to help stabilise the emulsion. The emulsion was also added to the Mastersizer 'hot', at 65 °C, rather than being cooled first. This was to make sure that the emulsion formed at the same temperature as the equipment and avoided any destabilisation caused when introducing the sample. A larger volume of the aqueous phase was also used so that the emulsion could be added directly to the Mastersizer without prior dilution. This was because the sizer employed a flow–through system which would mix the sample with an aqueous medium and dilute the sample for analysis. Stirring and dilution (not shown) have been seen to destabilise the emulsion due to an increase in shear, and so, by initially using a larger volume of water to make the emulsion, this would eliminate the dilution stage and allow the propeller to be run at its lowest setting. For these experiments, this setting was 1500 rpm and, although this still accelerated the rate of destabilisation, this gave an interesting result for the drop size, seen in Figure **3.12**.

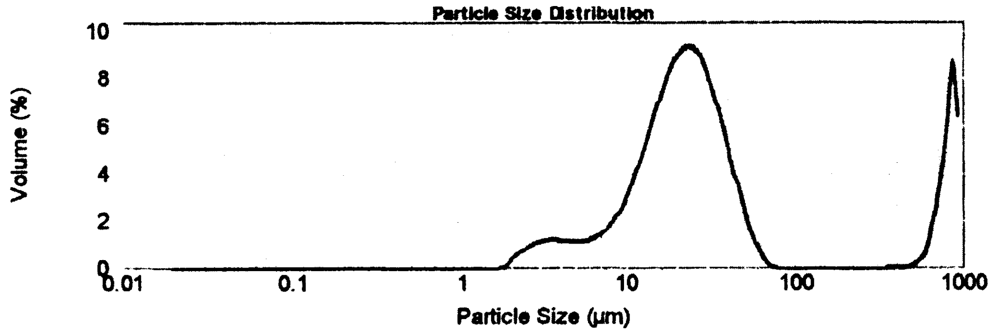

Figure 3.12: Graph showing emulsion drop percentage volume vs. drop diameter (µm) for an emulsion containing DCE–in–H_2O, measured at 25 °C using a Mastersizer 2000.

From Figure **3.12**, two peaks, at 3.6 and 12.3 µm belonging to two different populations of drop diameters, can be seen. The peak at 3.6 µm corresponds to the expected diameter of the emulsion drops, whereas the larger peak at 12.3 µm is believed to be from larger coalesced drops formed by the stirring of the solution. Using the measured percentage volume for each diameter, a ratio of 6:1 is calculated for drops at 3.6:12.3 µm, showing that the smaller drops are more prevalent in solution, even though the peak height for the larger drops is much greater than that for the small drops.

3.3.3 Temperature Effects on the Oil–in–Water Emulsion

Due to the nature of the emulsion system and the way that it was formed, the solubilities of the system, and hence drop volume are sensitive to temperature changes. To investigate this further, an emulsion of DCE–in–1.5 M sucrose D_2O was created, following the method described in **2.4**, by heating to 65 °C for 1 hour and cooling to 15 °C for 30 mins, and then a sample was taken. Sucrose was included in the emulsion to reduce the rate of sedimentation, described in **4.2**. Using the microscope temperature controller, a sample of the emulsion was heated under a optical microscope, as outlined in **2.6**, and the drop volume was measured at intervals as the emulsion was heated in recorded increments from 15 to 40 °C. The measured volume was then converted to weight percent using the measured initial number density of $140 \pm 12 \times 10^6$ drops per cm^3 and this was plotted in Figure **3.13**, showing that the weight percent of the DCE drops, and hence also drop volume, is inversely proportional to the temperature, as expected. The data was also regression fitted using the equation: y=0.08+0.8exp$^{-0.07x}$.

This effect of temperature on the emulsion was also reversible and to illustrate this, an emulsion of 5 mM LiTPFB DCE–in–1.5 M sucrose D_2O was created as described in **2.4**, sucrose was again used to reduce sedimentation and also the potential–determining salt, lithiumtetrakis(pentafluorophenyl)borate (LiTPFB) was added to reduce the rate of coalescence, described in **4.3**.

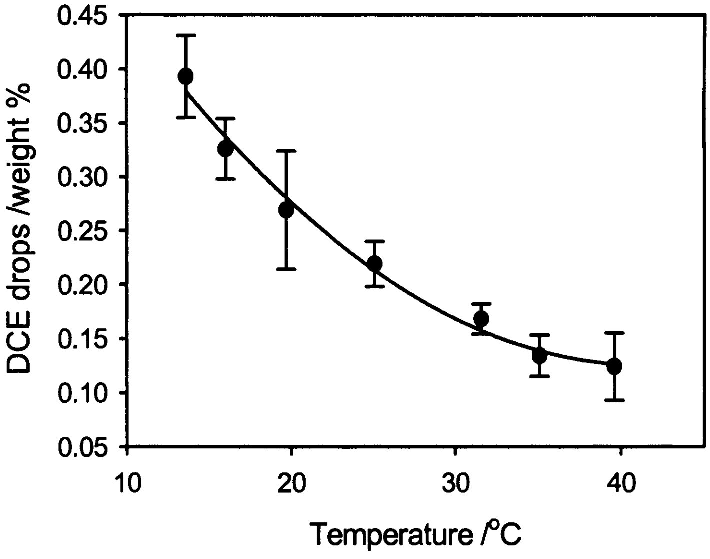

Figure 3.13: Graph showing the weight percent of DCE as emulsion drops vs. the temperature of the system for an emulsion containing DCE–in–1.5 M sucrose D_2O. The solid line is the regression fit using the equation: $y=0.08+0.8\exp^{-0.07x}$.

After the emulsion had cooled to 15 °C for 30 mins, a sample was put into a 10 mm pathlength cuvette and analysed using a UV–Vis spectrophotometer set at 15 °C. Figure **3.14** shows the turbidity at 550 nm versus time of the emulsion sample as the temperature was cycled starting from 15 °C to 35 °C and then down to 15 °C. As the temperature was increased the drop volume decreased accordingly and thus there was a corresponding decrease in turbidity. The reverse was observed on cooling from 35 °C to 15 °C. The turbidity at 25 °C, seen at points (b) and (d) in Figure **3.14**, shows no change after heating and cooling, indicating that there was no significant change in the number density of the emulsion. There was, however, a small decrease in the turbidity of the emulsion at 15 °C, at the end of the experiment compared to the start, and this was probably due to convection currents destabilising the emulsion during the experiment.

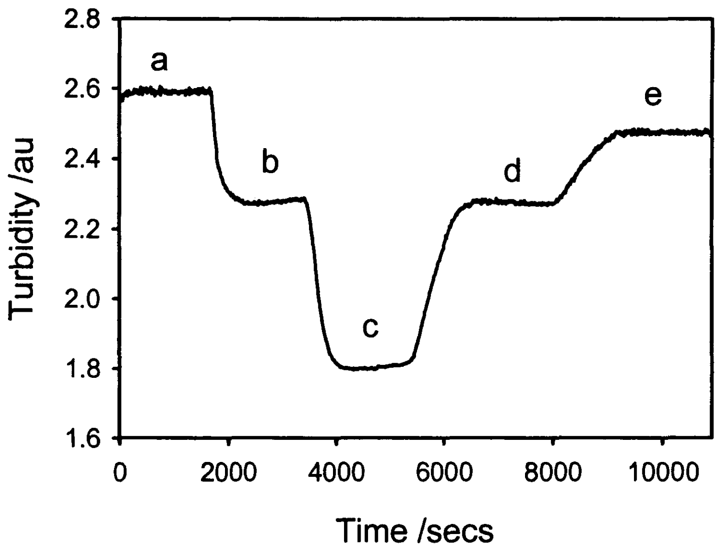

Figure 3.14: Turbidity at 550 nm versus time for temperature cycling starting from 15 °C (a), 25 °C (b), 35 °C (c), 25 °C (d) and 15 °C (e). This is for an emulsion of 5 mM LiTPFB DCE–in–1.5 M sucrose D_2O, using a 10 mm pathlength cell.

The rate at which the temperature was altered was maintained at a slow rate of approximately 1–2 °C per minute during the experiment. This was because, if the temperature was decreased too quickly (1–2 °C per second), the emulsion drop volume would increase slightly, but a secondary emulsion would also start to nucleate and grow, discussed further in Chapter **5**.

3.4 Conclusions

It was found that the most reproducible emulsion was formed using a Condensation Technique, manipulating the solubility of DCE in water. This technique was optimised and a procedure was created for the formation of a surfactantless DCE–in–water emulsion. This involved heating a mixture of DCE and water to 65 °C for 1 hour with stirring and then cooling rapidly in a water bath set at 15 °C for 30 mins. The emulsion was then characterised using optical microscopy and UV–Vis spectrophotometry and was found to have an initial number density of $140 \pm 12 \times 10^6$ drops per cm^3 and an initial average drop volume of 25 ± 5 μm^3. This was seen to almost double after 7 hours in a sealed container, however, and was shown to be very unstable. The emulsion drops were also found to be very sensitive to external shear and this was shown when using conventional light scattering techniques and also electrochemistry. Cyclic Voltammetry (CV) and Rotating–Disc Electrode (RDE) studies were carried out to look at the diffusion kinetics of the electrochemical probes tetrathiafulvalene (TTF), ferrocene (Fc) and butylferrocene (BuFc) across the emulsion interface; however problems were encountered when the solution was stirred by the electrode. The rotation caused rapid destabilisation of the emulsion and a layer of DCE was seen to form at the electrode surface, thereby preventing any useful information being obtained.

The emulsion was also seen to be sensitive to changes in temperature, with the drop volume being inversely proportional to an increase in temperature. This phenomenon was shown to be reversible and that the drop volume could be controlled using temperature changes. This was only dependent on the temperature being changed by 1–2 °C per minute, rather than 1–2 °C per second. If the temperature change occurred too quickly, a secondary emulsion would start to nucleate and grow from the DCE dissolved in the aqueous phase, rather than this adding volume to the original emulsion drops.

Overall, techniques using a condensation method, optical microscopy and turbidity measurements, were developed and optimised to create and characterise a surfactantless emulsion with a reproducible drop volume and number density.

Chapter 4: Stabilisation of an Oil–in–Water Emulsion

4.1 Introduction

In this chapter, the stabilisation of the DCE–in–D_2O emulsion created and characterised in Chapter **3**, is described. This is achieved by reducing the effects of sedimentation by dissolving sucrose, a neutral density–altering species, in the aqueous phase, and also reducing coalescence of the drops, by establishing a Galvani–type potential across the oil–water interface. The effects of the stabilisation have been monitored using turbidity and optical microscopy measurements and the emulsion is seen to have significant stabilisation over two hours compared with an emulsion of DCE–in–D_2O only.

4.2 Reducing Sedimentation

A set of experiments were designed and carried out to investigate the effects of gravity on the oil–in–water emulsion system. As DCE (density = 1.235 g cm^{-3} at 20 °C) [186] is denser than water, sedimentation of the drops, rather than creaming, occurs. It was proposed that if the densities of the two liquids were matched then the rate of sedimentation would be reduced and the main factor affecting the stability would be that of coalescence. It was also thought that, due to the uniform drop size resulting from the condensation technique used, the effects of Ostwald ripening would be negligible.

Firstly, D_2O (ρ = 1.105 g cm^{-3} at 20 °C [186]) was used as the aqueous phase instead of H_2O. Emulsions were prepared, as in **2.4**, to compare DCE–in–H_2O only with DCE–in–D_2O only and the stability was monitored using turbidity measurements at 25 °C. The results are shown in Figure **4.1** and all the turbidity versus time graphs have been normalised for easier qualitative comparison. This was because, in these experiments, the emulsion was heated until it reached 65 °C for 20 mins. This led to the aqueous phase not being fully saturated with DCE and so the turbidities of the different emulsion samples were significantly different, making them hard to compare. The original turbidity values were 0.99 and 1.26 a.u., for the H_2O and D_2O emulsions respectively.

From Figure **4.1**, it can be seen that using D_2O does not give any significant stabilisation to the emulsion, relative to using H_2O. This can be verified by comparing the change in turbidity with time for the two plots; –179.5 x10^{-6} for H_2O and –172.6 x10^{-6} au s^{-1} for D_2O. The similarity between the destabilisation of the two systems is because the difference in density between H_2O and D_2O is negligible when compared with the density of DCE. Although it would be less expensive to use

H_2O as the aqueous phase, D_2O would be required in SANS experiments and so it was decided to use this in future stabilisation experiments.

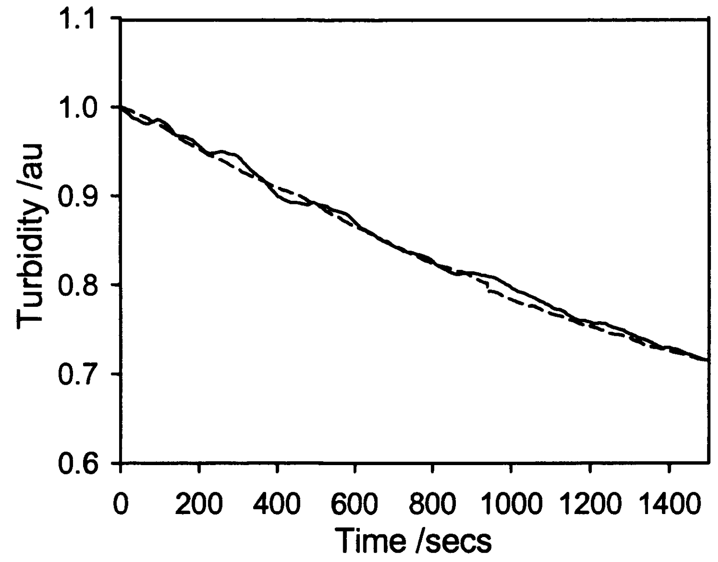

Figure 4.1: Turbidity at 550 nm vs. time at 25 °C, comparing H_2O (—) and D_2O (----) as the aqueous phase in a DCE–in–water emulsion. The original turbidity values were 0.99 and 1.26 au, and the rate of change of turbidity with time for the plots are –179.5 and –172.6 x10^{-6} au s^{-1} for the H_2O and D_2O emulsions respectively.

To match the density of the D_2O with that of the DCE, a neutral–density altering species, e.g. a sugar, was required. Possible aqueous sugar concentrations and their densities [186] can be seen in Table **4.1**, and these were matched with the density of DCE at 20 °C, a value of 1.235 g cm^{-3}. From Table **4.1**, sucrose was chosen on the basis of its cost, availability and effectiveness at altering density.

The literature densities of the different sucrose solution concentrations in H_2O investigated can also be seen in Table **4.2**, and included in this table is the experimentally measured gravimetric density of 1.5 M sucrose in D_2O.

Sugar	**Density /g cm^{-3} at 20 °C**	**Concentration /M**
Fructose	1.2404	3.580
	1.1372	2.020
Glucose	1.2342	3.562
	1.1340	2.014
Glycerol	1.2299	11.752
	1.1308	6.385
Maltose	1.2304	1.796
	1.1367	1.062
Sucrose	1.2295	1.796
	1.1366	1.063

Table 4.1: Showing the densities of different concentrations of various sugars dissolved in water at 20°C [186].

Solution	**Density /g cm^{-3}**
H_2O	0.998
D_2O	1.105
DCE	1.235
0.5 M Sucrose $_{H2O}$	1.07
1.0 M Sucrose $_{H2O}$	1.13
1.5 M Sucrose $_{H2O}$	1.19
2.0 M Sucrose $_{H2O}$	1.25
1.5 M Sucrose $_{D2O}$	1.26

Table 4.2: Showing the literature densities of various solutions at 20 °C [186], and also the experimentally measured density of 1.5 M Sucrose in D_2O at room temperature.

As the densities of the two phases change with temperature, an experiment was designed to determine at which temperature the densities of the DCE and D_2O/sucrose solution were matched. The experiment involved the observation of creaming or sedimentation of large (1–3 mm diameter) DCE drops in aqueous sucrose solutions, as the solution was heated slowly from 5 to 85 °C. The initial state of the sample was recorded and as the emulsion was heated, the density of the DCE relative to the D_2O, and vice versa, was observed. Different sucrose concentrations were investigated in a range of 0.5 to 2.0 M and temperature ranges were determined for each concentration of sucrose to show at which temperature the DCE would be affected by either sedimentation or creaming. The results are shown in Table **4.3**.

Sucrose conc. /M **DCE state**	**1.0**	**1.25**	**1.5**	**1.75**	**2.0**
Sedimented	< 60 °C	< 45 °C	< 30 °C	< 15 °C	< 10 °C
Dispersed	65–73 °C	53–58 °C	40–45 °C	28–33 °C	15–23 °C
Creamed	> 80 °C	> 63 °C	> 55 °C	> 45 °C	> 30 °C

Table 4.3: Showing the temperature range at which the DCE phase is dispersed (i.e. the same density) as the D_2O phase containing different concentrations of sucrose.

It can be seen, from Table **4.3**, that at 25 °C, the optimum concentration of sucrose in D_2O would be between 1.75 and 2.0 M. It also shows that to match the densities of the two liquids, a balance needs to be achieved between the concentration of sucrose and the temperature that the solution is cooled to during formation.

Different sucrose concentrations between 0.5–2.0 M were then tested in an emulsion. The emulsion was made using the procedure outlined, in **2.4**, with the sucrose dissolved first in the D_2O before the DCE was added, and after cooling for 30 mins to 15 °C, a sample was taken for analysis of turbidity with time. The results can be seen in Figure **4.2**. As explained, the turbidity versus time graphs have been normalised and, for these experiments, the original turbidity values were 1.92, 1.71, 1.63 and 1.26 a.u., for 1.5, 1.0, 0.5 M and no sucrose respectively. It can be seen that there appears to be a trend of increasing turbidity with increasing sucrose concentration and, even though the samples were not heated until saturated, they were heated for approximately the same length of time, this suggests that the sucrose is therefore increasing the rate of solubility between the DCE and water. This could be due to the increased viscosity of the aqueous phase causing a decrease in the rate of coalescence and so maintaining a high DCE-water surface area during emulsion heating.

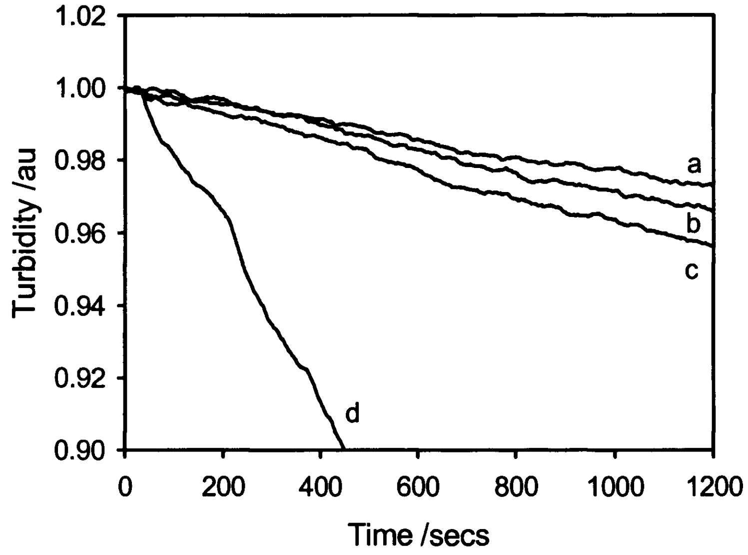

Figure 4.2: Turbidity at 550 nm vs. time at 15 °C, for DCE–in–D_2O containing (a) 1.5 M, (b) 1.0 M and (c) 0.5 M sucrose with no salts and (d) a sample of DCE–in–D_2O only. The original turbidity values were 1.63, 1.71, 1.92 and 1.26 au, and the rate of change of turbidity with time for the plots are –23.5, –29.7, –36.8 and –214.6 x10^{-6} au s^{-1} for 1.5, 1.0, 0.5 M and no sucrose respectively.

From Figure **4.2**, and by comparing the change in turbidity with time for the results from each sucrose concentration, it can be seen that with a concentration of sucrose of 1.5 M there was a marked improvement on the stability of the emulsion, by reducing the effect of phase separation. For 1.5 M sucrose, the change in the turbidity with time is –23.5 x10^{-6} au s^{-1}, whereas for an emulsion containing DCE–in–D_2O only, this is increased to –214.6 x10^{-6} au s^{-1}. For emulsions containing 1.0 and 0.5 M sucrose, the change of turbidity with time was –29.7 and –36.8 x10^{-6} au s^{-1} respectively. When a solution of 2.0 M sucrose in D_2O was investigated, the density of the DCE was less than that of the D_2O, and so the DCE formed a layer at the top of the mixture, resulting in evaporation as the solution was heated. This prevented the emulsion from forming via a condensation method. There was also a limit to the amount of sugar that could be dissolved in the aqueous phase and the higher the concentration, the higher the probability of precipitates forming when the emulsion was heated and then cooled rapidly. It was therefore ensured that the concentrations of sucrose and stabilising salts used in all future experiments, were low enough so that precipitates did not form.

Different glucose concentrations were also tested in a range of 1.7M to 2.7M, and the emulsion was made using the procedure explained in **2.4**, with the sugar dissolved first into the D_2O before the DCE was added. These emulsions were then studied using turbidity measurements, and the results can be seen in Figure **4.3**.

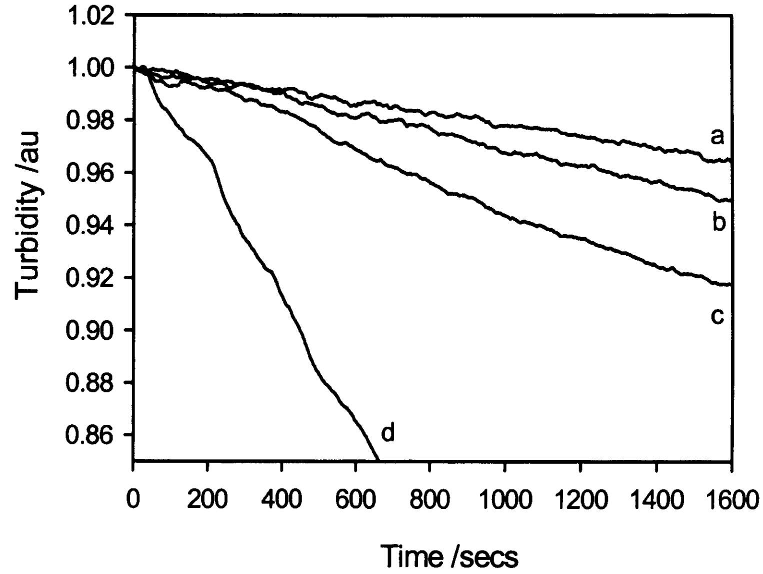

Figure 4.3: Turbidity at 550 nm versus time at 25 °C, for DCE–in–D_2O containing (a) 2.7 M, (b) 2.2 M and (c) 1.7 M glucose with no salts and (d) a sample of DCE–in–D_2O only. The original turbidity values were 1.11, 1.24, 1.46 and 1.26 au, and the rate of change of turbidity with time for the plots are –20.7, –32.8, –58.1 and –215.3 x10^{-6} au s^{-1} for 2.7, 2.2, 1.7 M and no glucose respectively.

The data in Figure **4.3** was also normalised, with the initial turbidity values being 1.11, 1.24, 1.46 and 1.26 a.u., for 2.7, 2.2, 1.7 M and no glucose respectively. There appears to be an inverse trend, when compared with the experiment using sucrose, in the turbidity values with relation to glucose concentration and it is thought that this is due to changes in experimental technique between creating the samples and not due to the glucose affecting the emulsion number density.

From Figure **4.3**, it can be seen that glucose also stabilised the system well by reducing the change in turbidity with time to -20.7×10^{-6} au s^{-1} for 2.7 M glucose compared to -215.3×10^{-6} au s^{-1} for an emulsion of DCE–in–D_2O only. 2.7 M glucose is a relatively high concentration compared to the amount of sucrose that gives slightly less stability (-23.5×10^{-6} au s^{-1} for 1.5 M) and therefore sucrose, at a concentration of 1.5M in D_2O, was determined to be a better density–matching species than glucose. The emulsion was still seen to destabilise over time, however, due to the effects of coalescence.

4.3 Reducing Coalescence

Coalescence of the drops is caused by the high surface energy at the liquid–liquid interface, causing a decrease in the electrostatic repulsion, and therefore resulting in the coalescence of the DCE drops. To reduce these effects, the liquid–liquid interface was 'electrified' using potential–determining salts, following the principles of DLVO theory, as introduced in **1.2.4**, which describes the stability of an emulsion as a function of the ionic strength of the aqueous phase.

Setting up the electrical double layers can be achieved by two different methods; a single partitioning salt that is soluble in both phases and a two salt system with a 'common ion' dissolved in each phase. These are illustrated in Figure **4.4** as schemes (a) and (b) respectively.

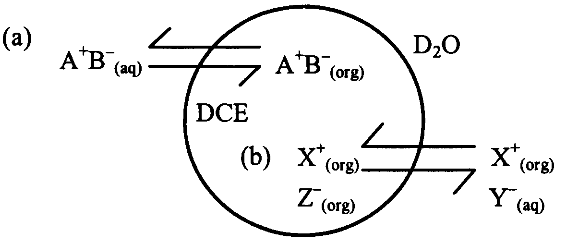

Figure 4.4: Schematic diagram of a DCE drop in a D_2O phase showing (a) the partitioning of a single potential–determining salt, soluble in both phases, across the liquid–liquid interface, e.g. LiTPFB or THpABr (A^+B^-), and (b) the partitioning of a two salt 'common ion' system, e.g. $TEACl_{(aq)}$ (X^+Y^-) and $TEATPB_{(org)}$ (X^+Z^-).

4.3.1 Investigating the Two–Salt Emulsion Stabilisation System

By using a system of two salts, a Galvani–type potential can be established across the liquid–liquid interface; scheme (b) in Figure **4.4**. This is made possible by using two salts with a 'common ion', e.g. tetraethylammonium (TEA^+), and a hydrophilic or hydrophobic counter–ion, e.g. chloride (Cl^-) or tetraphenylborate (TPB^-). With one salt dissolved in the aqueous phase and the other in the DCE, and by using different concentrations of the salts, the common ion is distributed unequally across the interface and hence a potential gradient is set–up, similar to a Galvani potential described in **1.1.2**. This potential makes the emulsion drops 'charged' and hence, when they are in solution, they repel each other and destabilisation from coalescence is reduced.

Firstly this theory was tested to see if using a salt system improved emulsion stability. Two emulsions were created as described in **2.4**; one with 1.5 M sucrose added to reduce sedimentation and both with 0.1 M tetraethylammonium chloride (TEACl) dissolved in the D_2O phase and 10 μM tetraethylammonium tetraphenylborate (TEATPB) in the DCE phase. These ions were added to the separate phases before the two were mixed and heated, and then once the emulsions had cooled at 15 °C for 30 mins, samples were taken for analysis using turbidity measurements. These were then compared with the turbidity results for an emulsion containing DCE–in–D_2O only and are shown in Figure **4.5**. The initial turbidity values, before normalisation, were 1.76, 1.88 and 1.26 a.u. for the emulsions: salts and sucrose, salts only and DCE–in–D_2O only respectively.

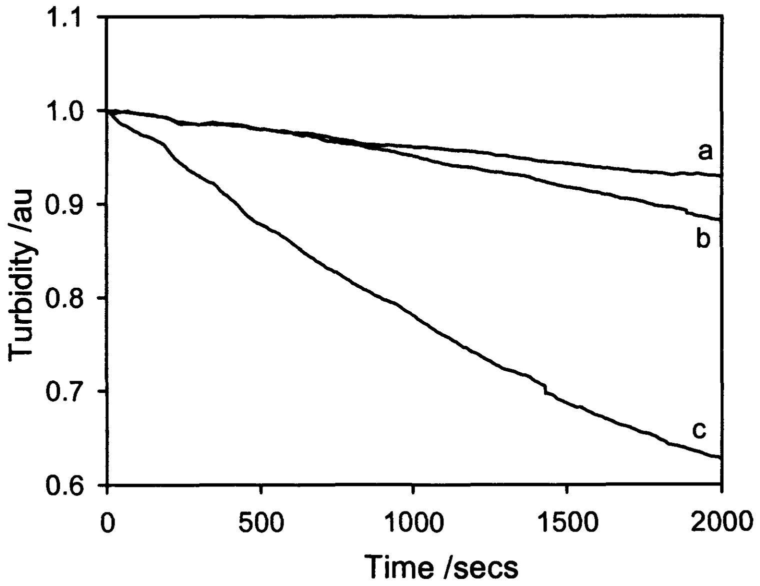

Figure 4.5: Graph comparing turbidity at 550 nm vs. time at 15 °C for emulsions containing (a) 10 μM TEATPB DCE–in–0.1 M TEACl, 1.5 M sucrose D_2O, (b) 10 μM TEATPB DCE–in–0.1 M TEACl D_2O and (c) DCE–in–D_2O only. The original turbidity values were 1.76, 1.88 and 1.26 au, and the rate of change of turbidity with time for the plots are –33.4, –60.8 and –182.2 $\times10^{-6}$ au s^{-1} for emulsions stabilised using TEA^+ and sucrose, TEA^+ only, and an emulsion of DCE–in–D_2O only, respectively.

From Figure **4.5** it is clearly seen that the presence of potential–determining salts in the emulsion has a marked improvement on the stabilisation of the system, which is improved further with the inclusion of sucrose. This is illustrated by looking at the values for the change in turbidity with time. For an emulsion with no stabilisation, this equals –182.2 $\times10^{-6}$ au s^{-1}, and is decreased to –60.8 $\times10^{-6}$ au s^{-1} when potential–determining salts are used. This is then decreased further to –33.4 $\times10^{-6}$ au s^{-1} when using both sucrose and potential–determining salts. These results cannot, however, be compared with the results obtained in **4.2** due to the different experimental conditions used. This was because, when investigating the effects of sedimentation, the turbidity measurements were made using a Pye Unicam SP8–100

UV–Vis spectrophotometer and all emulsions were made at room temperature, 25 °C. The emulsion creation and monitoring techniques were subsequently optimised and all further experiments were undertaken at a recorded and controlled temperature using the Agilent 8453 UV–Vis Spectroscopy System. The results presented in **4.2** can still be analysed qualitatively, however, to investigate the optimum concentration of sucrose needed to effectively reduce sedimentation.

To investigate the stabilisation from the salts further, different salt concentrations were studied. The concentration affects the interfacial potential according to Equation **4.1**, first introduced in **1.1.2** as Equation **1.7** [75]:

$$\Delta_O^W \phi = \Delta_O^W \phi_i^o + \frac{RT}{z_i F} \ln \frac{\gamma_i^O c_i^O}{\gamma_i^W c_i^W} \qquad \textbf{4.1}$$

Where $\Delta_O^W \phi$ and $\Delta_O^W \phi_i^o$ are the interfacial equilibrium and standard ion–transfer potentials respectively, R is the gas constant (8.3145 J mol^{-1} K^{-1} [186]), T is the absolute temperature (288 K at 15 °C), z_i is the ionic charge, F is the Faraday constant (96485.3 C mol^{-1} [186]), γ_i^O and γ_i^W are the activity coefficients and c_i^O and c_i^W are the concentrations of the 'common ion' in the oil and water phases. As described in **1.1.2**, this is similar to the Nernst Equation for redox reactions and is used to describe the potential at the interface between two immiscible electrolyte solutions (ITIES). From Equation (4.1), it can be seen that the interfacial potential is determined by the standard ion–transfer potential and the concentration ratio of the ion in the water and oil phases. It is thought that by changing this concentration ratio, the magnitude of the potential could be changed, thus further reducing the rate of coalescence. It was assumed that the concentration of the ions in the DCE drops at 15 °C was the same as the initial concentration before heating. This is not strictly correct but the concentration in the drops would certainly be a fraction of the initial value. This is because the salt concentration is determined by its solubility in water at the highest and lowest temperatures used in emulsion formation but this, however, must be calculated in terms of the number of moles of the organic ion in the DCE and water due to the different volumes of each phase present. If the initial number of moles of the organic ion is lower than the aqueous number of moles at 65 °C, the final number of moles in the DCE drops will be equal to the initial number of moles minus the number of moles dissolved in the aqueous phase at 15 °C, Equation **4.2**.

$$n(\mathrm{TEATPB_{DCE}})_{\mathrm{Final}} = n(\mathrm{TEATPB_{DCE}})_{\mathrm{Initial}} - n(\mathrm{TEATPB_{Aq}})_{15\,^{\circ}\mathrm{C}} \qquad \textbf{4.2}$$

Where $n(\mathrm{TEATPB}_x)_y$ is the number of moles of TEATPB in solution x at temperature or time y. If, however, the initial number of moles in the DCE is higher than the aqueous number of moles at 65 °C, the final number of moles in the DCE drops will be equal to the number of moles dissolved in water at 65 °C minus the aqueous number of moles at 15 °C, Equation **4.3**.

$$n(\mathrm{TEATPB_{DCE}})_{\mathrm{Final}} = n(\mathrm{TEATPB_{Aq}})_{65\,^{\circ}\mathrm{C}} - n(\mathrm{TEATPB_{Aq}})_{15\,^{\circ}\mathrm{C}} \qquad \textbf{4.3}$$

Assuming that $n(\mathrm{TEATPB_{DCE}})_{\mathrm{Final}} = n(\mathrm{TEATPB_{DCE}})_{\mathrm{Initial}}$ (i.e. $n(\mathrm{TEATPB_{Aq}})_{15\,^{\circ}\mathrm{C}}$ is negligible) and that the charge on the ion and the activity coefficients are unity, approximate values for the interfacial potential have been calculated using Equation **4.1**, at 15 °C (288 K), and are shown in Table **4.4**. The 'common ion' investigated was $\mathrm{TEA^+}$ and the standard ion–transfer potential used in the calculations was 43.5

mV [78]. The concentration of the aqueous ion was kept constant at 0.1 M whilst the concentration of the organic ion was changed.

$c^{DCE}_{TEA^+}$ / M	$\Delta^W_O\phi$ / mV
1 x10^{-3}	–70.8
1 x10^{-4}	–171.4
1 x10^{-5}	–228.6

Table 4.4: Calculated values, using Equation **4.1**, for the interfacial potential, $\Delta^W_O\phi$, for different initial organic ion concentrations, $c^{DCE}_{TEA^+}$, at 15 °C.

From Table **4.4**, it can be seen that as the ratio of the concentration of the aqueous ion to that of the organic ion is increased, the magnitude of the equilibrium potential increases. These are only approximate calculations for the potential because the equilibrium concentration of the organic ion is likely to be less than the initial value and the activity coefficients are assumed to be unity. These organic ion concentrations were then used in an emulsion to investigate their effect on the stability. The salt concentrations used were 10 μM, 0.1 mM and 1 mM TEATPB with 0.1 M TEACl and the emulsions were created as described in **2.4**, with 1.5 M sucrose included to increase stability. The changes in turbidity with time were then measured for each emulsion at 15 °C and are shown in Figure **4.6**. The initial turbidity values for the emulsions were 1.84, 1.67 and 1.69 a.u. for the organic concentrations 10 μM, 0.1 mM and 1 mM respectively.

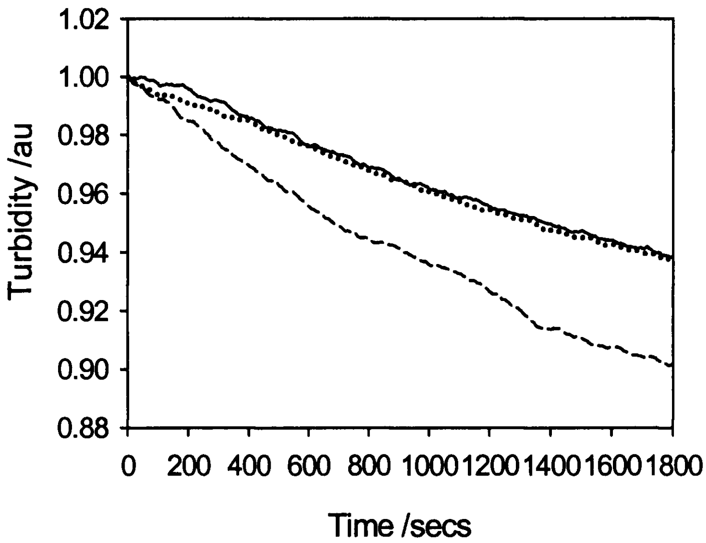

Figure 4.6: Graph comparing turbidity at 550 nm vs. time at 15 °C for emulsions containing (—) 10 μM, (······) 0.1 mM and (----) 1 mM TEATPB DCE–in–0.1 M TEACl, 1.5 M sucrose D_2O. The original turbidity values were 1.84, 1.67 and 1.69 au, and the rate of change of turbidity with time for the plots are –33.4, –34.8 and –51.8 $\times 10^{-6}$ au s^{-1} for emulsions stabilised using 10 μM, 0.1 mM and 1 mM TEATPB, respectively.

From Figure **4.6**, it can be seen that there is an increase in the stability of the emulsion when the organic ion concentration is decreased from 1 mM to 0.1 mM, with the change in turbidity with time decreasing from –51.8 $\times 10^{-6}$ au s^{-1} to –34.8 $\times 10^{-6}$ au s^{-1}. However, when this is decreased further from 0.1 mM to 10 μM, there is no significant change in the turbidity with time; –34.8 and –33.4 $\times 10^{-6}$ au s^{-1}.

From looking at Equation **4.1**, it was suggested that a greater change in interfacial potential might be achieved by using a different potential–determining 'common ion'. Each ion has a standard ion–transfer potential which can be determined using conventional electrochemistry techniques. Example values for standard ion–transfer potentials, $\Delta_O^W\phi_i^o$, are shown in Table **4.5** for a range of tetraalkylammonium salts. Included in Table **4.5**, is the interfacial equilibrium potential, $\Delta_O^W\phi$, when aqueous and organic concentrations of 0.1 M and 10 μM, respectively, are used. Also tabulated is the standard Gibb's energy of transfer of the ion from the aqueous to the organic phase, $\Delta G_i^{W \to O,o}$. This relates to the standard ion–transfer potential using, $\Delta_O^W \phi_i^o = \frac{1}{z_i F} \Delta G_i^{W \to O,o}$ as introduced in **1.1.2**.

Tetraalkylammonium ion (TXA$^+$)	$\Delta_O^W \phi_i^o$ /mV	$\Delta G_i^{W \to O,o}$ /kJ mol^{-1}	$\Delta_O^W \phi$ / mV
Methyl (TMA$^+$)	182.4	17.6	–46.2
Ethyl (TEA$^+$)	43.5	4.2	–185.1
Propyl (TPrA$^+$)	–91.2	–8.8	–319.8
Butyl (TBuA$^+$)	–224.9	–21.7	–453.5
Pentyl (TPeA$^+$)	–359.6	–34.7	–588.2
Hexyl (THxA$^+$)	–494.4	–47.7	–723.0

Table 4.5: Examples of standard ion–transfer potentials, $\Delta_O^W \phi_i^o$, and the standard Gibb's energy of transfer, $\Delta G_i^{W \to O,o}$, for tetraalkylammonium salts (TXA$^+$) [78] and the calculated approximate equilibrium interfacial potentials, $\Delta_O^W \phi$, at 15 °C, when the aqueous and organic ion concentrations are 0.1 M and 10 μM respectively. The activity coefficients are assumed to be unity.

From Table **4.5** it can be seen that by changing the salts used in the emulsion, the potential established could have a greater magnitude than from merely changing the concentration ratio.

To investigate this, tetraethylammonium (TEA$^+$) and tetrabutylammonium (TBuA$^+$) were used in emulsions as the 'common ion'. This was incorporated as the chloride salt (TXACl) in the aqueous phase and the tetraphenylborate salt (TXATPB) in the DCE. Three emulsions were created as in **2.4**, one containing DCE–in–D_2O only, and the other two using stabilising salts 0.1 M TXACl and 10 μM TXATPB, both with 1.5 M sucrose dissolved in the aqueous phase for added stability. The turbidity was then measured with time once the emulsions had cooled for 30 mins at 15 °C and the results are shown in Figure **4.7**. The data was normalised and the initial turbidity values were 1.94, 1.84 and 1.26 a.u. for TBuA$^+$, TEA$^+$ and DCE–in–D_2O only, respectively.

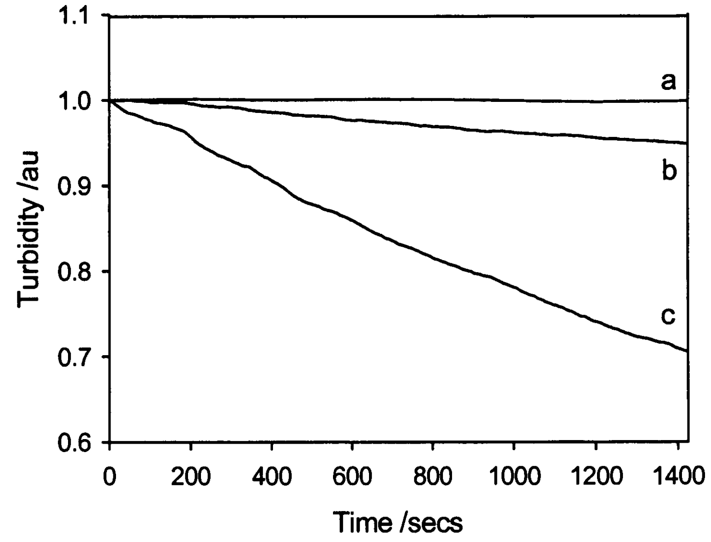

Figure 4.7: Graph comparing turbidity at 550 nm vs. time at 15 °C for emulsions containing (a) 10 μM TBuATPB DCE–in–0.1 M TBuACl, 1.5 M sucrose D_2O, (b) 10 μM TEATPB DCE–in–0.1 M TEACl, 1.5 M sucrose D_2O and (c) DCE–in–D_2O only. The original turbidity values were 1.94, 1.84 and 1.26 au, and the rate of change of turbidity with time for the plots are –10.2, –33.4 and –182.2 x10^{-6} au s^{-1} for emulsions stabilised using TBuA$^+$, TEA$^+$ and an emulsion of DCE–in–D_2O only, respectively.

Figure **4.7** shows that using TBuA$^+$ caused a significant improvement to the stability of the emulsion and that the rate of coalescence was effectively reduced. This was also shown by the values for the change in turbidity with time; –10.2 x10^{-6} au s^{-1} for an emulsion stabilised with TBuA$^+$ and 1.5 M sucrose, and –33.4 x10^{-6} au s^{-1} when using TEA$^+$ and sucrose. There is still some long–term destabilisation (not shown), however, but this is because the destabilising processes cannot be prevented completely and will still act to separate the two phases over time. This was illustrated by measuring the initial emulsion drop volume and number density at the start of the experiment and again after 20 hours. These measurements were taken following the procedure described in **2.6** and are tabulated in Table **4.6**. The diameter of the emulsion drops, in µm, is also included in brackets, below the value calculated for the drop volume in cm^3.

Emulsion Stabilisation	**Initial**		**After 20 Hours**	
	Drop Volume /µm^3	**Number Density /x10^6 drops cm^{-3}**	**Drop Volume /µm^3**	**Number Density /x10^6 drops cm^{-3}**
TBuA$^+$ + sucrose	24 ±5 (3.6 ±0.2 µm)	150 ±19	140 ±61 (6.3 ±0.8 µm)	10 ±6
TEA$^+$ + sucrose	27 ±5 (3.7 ±0.2 µm)	130 ±17	150 ±70 (6.5 ±0.9 µm)	5 ±6
Sucrose only	25 ±5 (3.6 ±0.2 µm)	140 ±12	180 ±35 (7.0 ±0.4 µm)	7 ±6

Table 4.6: Comparing the average initial drop volume and number density with measurements taken after 20 hours, for emulsions containing TBuA$^+$ and sucrose, TEA$^+$ and sucrose, and an emulsion stabilised with 1.5 M sucrose only. The standard deviation, determined from replicate measurements, is given as the error. Also included in brackets, is the average drop diameter, in µm, below the determined value for the drop volume in cm^3.

Table **4.6** shows that after 20 hours, all three emulsion systems have destabilised by the same order of magnitude, with a doubling of the drop diameter from 3.6 to 6.6 µm, and that any stabilisation achieved from using sucrose and potential–determining ions is largely seen over the first few hours, as shown by Figure **4.7**.

4.3.2 Determining the Interfacial Potential for a Two–Salt Emulsion

The approach used to determine the interfacial potential, was by calculation using Equation **4.1**. To do this, the standard ion–transfer potential of the 'common ion' and its activity coefficient and concentration in both the water and oil phases needed to be known. These can all be determined except the activity coefficient and concentration of the ion in DCE. The equilibrium concentration would not equal the initial concentration due to the method with which the emulsion is created, because, as the two liquids are mixed and heated, the DCE dissolves into the water phase, as does a proportion of the potential–determining salt. The remaining oil soluble salt stays in the 'excess' DCE that does not dissolve in the water. When the emulsion cools, the dissolved proportion of oil–soluble salt diffuses back into the condensing DCE drops and results in different concentrations of salt in the emulsion drops and in the excess DCE. To determine the concentration of the 'common ion' in the DCE emulsion drops, it was proposed that UV–Vis spectroscopy could be used, along with the Beer–Lambert Law, Equation **4.4**.

$$A=\varepsilon_{\mathrm{m}}cl \qquad \mathbf{4.4}$$

Where A is the absorbance of the sample, c is the concentration, l is the path length of the sample, and ε_{m} is the molar absorbtivity coefficient. Because the potential–determining salt TPB$^-$ contains phenyl groups, which would absorb light in the UV range, the molar absorbtivity coefficient can be determined by measuring the maximum absorbance for different concentrations of TEATPB in DCE. Firstly solutions were created containing 0.1 mM and 10 μM TEATPB in DCE. UV scans were run in a range of 190–1100 nm, using a 10 mm pathlength cell and DCE to blank the UV spectrophotometer and an absorbance peak was seen at 242 ±1 nm in both solutions, and is shown in Figure **4.8**.

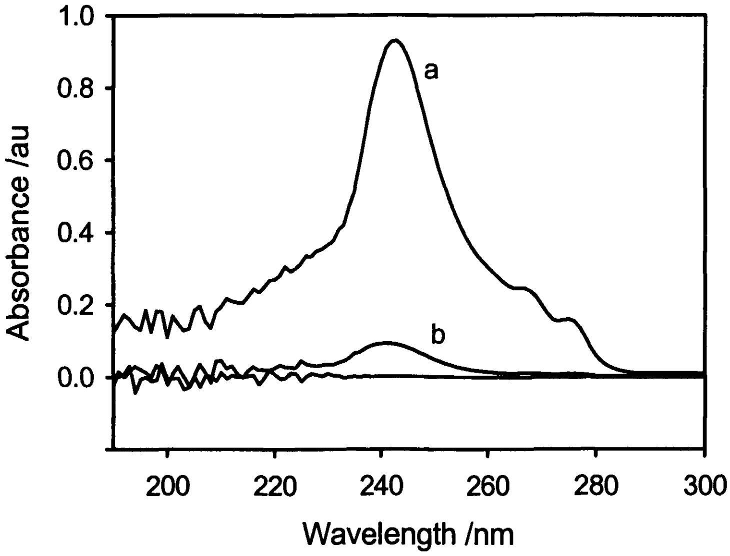

Figure 4.8: Graph showing the absorbance vs. wavelength, in a range from 190–300 nm, for different concentrations of TEATPB in DCE: (a) 0.1 mM and (b) 10 μM. The base line is DCE only.

Table **4.7** contains the maximum absorbance value for each TEATPB concentration and, using Equation **4.4**, the calculated molar absorbtivity coefficient. This was determined to be 930 mol^{-1} mm^{-1} for TPB$^-$ in DCE.

[TEATPB] /M	**Absorbance at 242 ±1 nm /au**	**Calculated ε_m of TPB$^-$ in DCE /mol^{-1} mm^{-1}**
1 x10^{-4}	0.93	930
1 x10^{-5}	0.093	930

Table 4.7: Showing the maximum absorbance at 242±1 nm and calculated molar absorbtivity coefficients for a range of TEATPB concentrations in DCE.

The shift in the absorbance peak, and resulting error, was thought to be due to the occurrence of ion–association in the DCE.

The absorbance could then be measured for an emulsion sample and the concentration of the ion in the DCE drops calculated. Because the emulsion sample would also scatter light, i.e. the turbidity measurement, the absorbance of the ions in the DCE would equal Equation **4.5**.

$$A_{\mathrm{TPB}^-} = A_{(\text{turbidity of emulsion + max. absorbance TPB}^-)} - A_{(\text{turbidity of emulsion only})} \qquad \mathbf{4.5}$$

Where $A_{(\text{turbidity of emulsion + max. absorbance TPB}^-)}$ was measured at 242±1 nm and $A_{(\text{turbidity of emulsion only})}$ is from the same emulsion but at a different wavelength where no ionic absorbance was seen (550 nm). These were obtained from the same UV–Vis scan of absorbance versus wavelength over 190–1100 nm, for a single emulsion sample, to ensure reproducibility.

An emulsion of 2 mM TEATPB, DCE–in–0.1 M TEACl, 1.5 M sucrose, D_2O was therefore created, as in **2.4**, and the UV spectrum was measured. A small peak was seen at 272.3 ±0.2 nm with a maximum absorbance of 0.908 au, and is shown in Figure **4.9**. At 550 nm, the absorbance was only from the emulsion turbidity and a value of 0.579 au was determined for this. The high absorbance seen at <210 nm was due to the aqueous dissolved DCE, as observed in **3.2**, and from the sucrose and TEACl in the aqueous phase of the emulsion, shown in background scans of the emulsion components, Figure **4.10**.

Using the calculated maximum absorbance from Equation **4.5** and an average molar absorbtivity coefficient of 930 $\mathrm{mol}^{-1}\ \mathrm{mm}^{-1}$, the calculated concentration for the emulsion TEATPB concentration is determined to be 0.2 mM, compared with the initial concentration of 2 mM.

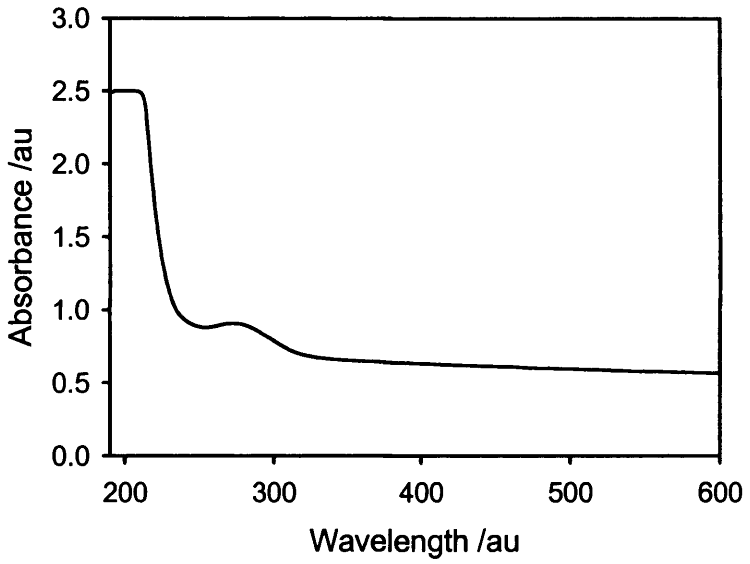

Figure 4.9: Graph showing the absorbance vs. wavelength, in a range from 190–600 nm, for an emulsion of 2 mM TEATPB, DCE–in–0.1 M TEACl, 1.5 M sucrose, D_2O.

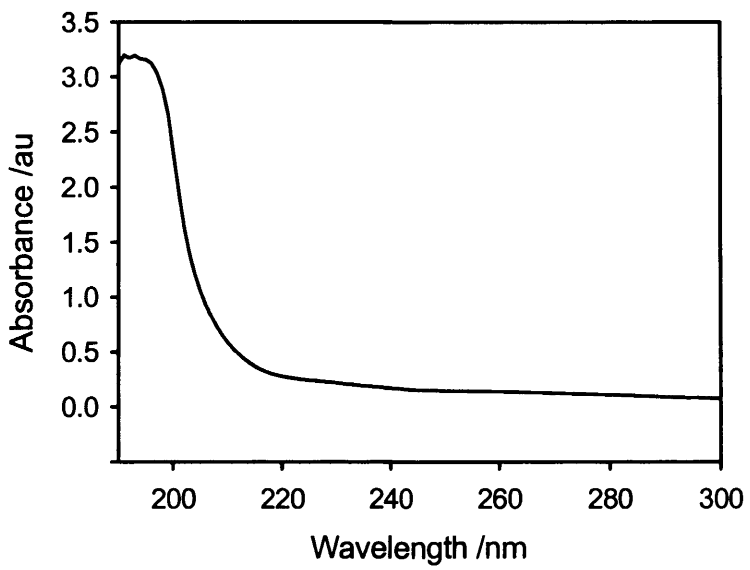

Figure 4.10: Graph showing the absorbance vs. wavelength, in a range from 190–300 nm, for a solution of 0.1 M TEACl and 1.5 M sucrose in D_2O.

For the calculation using Equation **4.4**, the pathlength for the cell was estimated to be 2 mm rather than 10 mm, which was used to determine the molar absorbtivity coefficient. This is because the pathlength in the emulsion would not be the width of the cuvette, but the sum of the diameters of each DCE drop in the light path. If the number of drops per cm^3 is 140 x10^6, hence 520 drops per cm, and the diameter of one drop is 4 μm, the sum of the diameters would be 0.2 cm.

To confirm the calculated concentration value of 0.2 mM for TEATPB in the DCE emulsion drops, the experiment was then repeated using tetrathiafulvalene (TTF) as the organic ion. This was originally used in electrochemical experiments, in Chapter **3**, to investigate the dynamics at the liquid–liquid interface and, because it is very hydrophobic, it was thought to have a similar solubility in water as TEATPB. TTF has a single absorption maximum in the UV range and, by using this as the oil soluble ion in the emulsion, it was hoped that it would give a more accurate molar absorbtivity coefficient, and a more defined UV spectrum for the emulsion. The TTF concentrations used were 0.1 mM and 50 μM in DCE and their UV spectra were measured as for TEATPB, shown in Figure **4.11**. Also included in Figure **4.11**, is the spectrum obtained for an emulsion of 2 mM TTF, DCE–in–D_2O, created as in **2.4**.

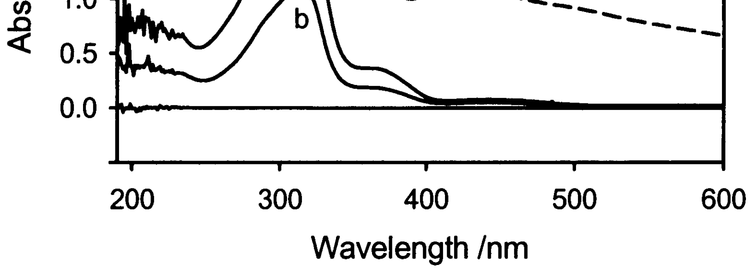

Figure 4.11: Graph showing the absorbance vs. wavelength for different concentrations of TTF in DCE: (a) 0.1 mM and (b) 50 μM. Also included is the UV spectrum (-----) for an emulsion of 2 mM TTF, DCE–in–D_2O (c). The base line is DCE only.

From Figure **4.11**, the maximum absorbencies at 319 nm, were measured and the molar absorbtivity coefficients were calculated. These are shown in Table **4.8**.

[TTF] /M	Absorbance at 319 nm /au	Calculated ε_m of TTF in DCE /mol^{-1} mm^{-1}
1 x10^{-4}	2.097	2097
5 x10^{-5}	1.044	2088

Table 4.8: Showing the maximum absorbance at 319 nm and calculated molar absorbtivity coefficients for a range of TTF concentrations in DCE.

The molar absorbtivity coefficient for TTF in DCE was calculated to be 2092.5 ±4.5 mol^{-1} mm^{-1} and, from Figure **4.11**, the maximum absorbance from TTF in the emulsion was measured as 1.648 au at 319 nm. The concentration of TTF in the DCE drops of the emulsion sample, using the determined molar absorbtivity and absorbance, was then calculated to be 0.2 mM, compared to the initial concentration of 2 mM and is comparable to the concentration calculated for TEATPB. Because the organic ion concentration in the emulsion drops is dependent on the solubility of the oil–soluble ion in water, the results show that at least 0.15 mM TXATPB will be present in the DCE drops. Therefore, for the emulsions containing 10 μM TXATPB, all of the oil–soluble ion should dissolve into the water as the emulsion is heated, and then diffuse back into the drops upon cooling. This would be true for both TEATPB and TBuATPB, because it is the solubility of the hydrophobic TPB$^-$ that determines the final concentration, following Equation **4.2**.

To calculate the interfacial potential, the activity coefficients of the ions in the oil and water phases also needed to be determined. Firstly the Bjerrum Equation, Equation **4.6**, introduced as Equation **1.14** in **1.1.2**, was used. This calculates q, the minimum distance of ion separation in the solvent, to determine if ion–association occurs.

$$q = \frac{z_+ z_- e^2}{8\pi \varepsilon_0 \varepsilon kT} \qquad \textbf{4.6}$$

Where z_+ and z_- are the ionic valences, e is the elementary charge constant (1.6022 x10^{-19} C [91]), ε_0 is the dielectric permittivity in a vacuum (8.8542 x10^{-12} F m^{-1} [91]), ε is the relative dielectric permittivity of the solvent (ε_{DCE} = 10.42 [91] and ε_{D2O} = 78.26 [190]), k is the Boltzmann constant (1.3807 x10^{-23} J K^{-1} [91]) and T is the absolute temperature (288 K). Solving Equation **4.6** for each solvent, gives values of q = 27.84 Å for DCE and q = 3.71 Å for D_2O at 15 °C. Table **4.9** contains the literature ionic radii for the salts used to stabilise the emulsion, and the resulting sum of the ionic radii, used as a in the Debye–Hückel Extended Law, Equation **4.7** introduced as Equation **1.9** in **1.1.2**.

Stabilising Ion	**Ionic Radii /Å**	**Stabilising Salt**	**Sum of Ionic Radii (a) /Å**
TEA^+	4.00 [187]	**$TEACl_{(aq)}$**	5.81
$TBuA^+$	4.94 [187]	**$TBuACl_{(aq)}$**	6.75
Cl^-	1.81 [188]	**$TEATPB_{(org)}$**	8.21
TPB^-	4.21 [189]	**$TBuATPB_{(org)}$**	9.15

Table 4.9: Showing the ionic radii and sum of the ionic radii, a, for the two–salt systems used in emulsion stabilisation.

From Table **4.9**, it can be seen that for the aqueous salts $a > q$ and that, as described in **1.1.2**, the calculated activity coefficient would follow the Debye–Hückel

Extended Law. For the organic salts, however, $a < q$, showing that ion–association would occur within the DCE phase and that the activity coefficient would not be unity.

For the aqueous salts, the activity coefficients were therefore estimated using the Debye–Hückel Extended Law in Equation **4.7**,

$$-\log \gamma_{\pm} = \frac{|z_+ z_-| A \sqrt{I}}{1 + B a \sqrt{I}} \qquad \textbf{4.7}$$

Where $\gamma_{\pm}$ is the activity coefficient for the electrolyte in solution, a is the sum of the ionic radii and I is the ionic strength of the solution, determined using Equation **4.8**,

$$I = \frac{1}{2} \sum_i m_i z_i^2 \qquad \textbf{4.8}$$

Where, m_i is the concentration of the cation or anion z_i. The parameters m_i, z_i and $\sqrt{I}$ for both $\text{TEACl}_{(aq)}$ and $\text{TBuACl}_{(aq)}$ aqueous stabilising salts were 0.1 M, ±1, and 0.316 respectively.

In Equation **4.7**, A and B are solvent and temperature dependent constants,

$$A = \frac{e^2 N_{\mathrm{A}}}{2.3 RT (8\pi\varepsilon_0\varepsilon)} \left(\frac{2 \times 10^3 N_{\mathrm{A}}{}^2 e^2}{\varepsilon_0 \varepsilon RT} \right)^{\frac{1}{2}} \qquad \textbf{4.9}$$

$$B = \left(\frac{2 \times 10^3 N_{\mathrm{A}}{}^2 e^2}{\varepsilon_0 \varepsilon RT} \right)^{\frac{1}{2}} \qquad \textbf{4.10}$$

Where N_A is the Avogadro number (6.0221 x10^{23} mol^{-1} [91]) and R is the molar gas constant (8.3145 J mol^{-1} K^{-1} [91]). Solving Equations **4.9** and **4.10** for D_2O gives, A = 0.540 $mol^{-1/2}$ $kg^{1/2}$ and B = 33.50 x10^8 m^{-1} $mol^{-1/2}$ $kg^{1/2}$ at 15 °C. The calculated activity coefficients were therefore determined to be $\gamma_{\pm}=1$, for $TEACl_{(aq)}$ and $TBuACl_{(aq)}$.

Because $a < q$, for the ions in the DCE phase, the activity will not be equal to unity due to the occurrence of ion–association and will therefore not follow the Debye–Hückel Extended Law. The interfacial potential has therefore been calculated, using Equation **4.1**, with a range of values for the organic ion activity coefficient and the results are shown in Table **4.10**.

γ^o	$\Delta^W_O\phi_{TEA^+}$ / mV	$\Delta^W_O\phi_{TBuA^+}$ / mV	γ^o	$\Delta^W_O\phi_{TEA^+}$ / mV	$\Delta^W_O\phi_{TBuA^+}$ / mV
1.0	-185	–453	**0.5**	-202	–471
0.9	-188	–456	**0.4**	-208	–476
0.8	-191	–459	**0.3**	-215	–483
0.7	-194	–462	**0.2**	-225	-503
0.6	-198	–466	**0.1**	-242	-511

Table 4.10: Showing the calculated interfacial potential, $\Delta^W_O\phi$, at 15 °C for TEA^+ and $TBuA^+$, using a range from 1.0 to 0.1 for the activity coefficient.

Using the data in Table **4.10**, the interfacial potentials for the two–salt emulsion systems are estimated to be –205 ±17 mV and –474 ±19 mV for systems using TEA^+ and $TBuA^+$ at 15 °C respectively.

The Debye-Length ($1/\kappa$) can also be estimated for the emulsions containing TEA^+ and $TBuA^+$ using Equation **4.11**, introduction as Equation **1.13** in **1.1.2**.

$$\kappa = \left(\frac{2x10^3 e^2 N_A}{\varepsilon_0 \varepsilon kT} \right)^{\frac{1}{2}} \sqrt{I} \qquad \mathbf{4.11}$$

This gives a value of 0.9 nm for the Debye–Length, or drop interaction distance, for both the emulsions stabilised with TEA$^+$ of TBuA$^+$. Comparing this with the calculated average separation distance between each drop; using $l = N^{-1/3}$, where N is the number density of drops per m^3 and gives a value of 19 µm, it can be seen that the Debye-Length, and hence interaction distance is much smaller that the drop separation distance, therefore confirming the stability of the emulsion drops as explained by DLVO theory.

4.3.3 Investigating the Single–Salt Emulsion Stabilisation System

The single salt system establishes a potential because the salts do not distribute across the two phases equally, scheme (a) in Figure **4.4**. This is because they dissolve more readily in one phase than the other and to illustrate this, a simple partitioning experiment was used. For this, a known concentration of either lithium tetrakispentafluorophenylborate (LiTPFB) or tetraheptylammonium bromide (THpABr) potential–determining salt was dissolved in 10 cm^3 DCE and this was then mixed with 10 cm^3 D_2O. After leaving to stand for 1 week, a 1 cm^3 aliquot was taken from each phase and the solvent was left to evaporate, hence leaving the precipitated salt. The initial and resulting equilibration masses can be seen in Table **4.11**, showing that both salts partition into the aqueous phase from the DCE layer, resulting in the D_2O becoming saturated with the salts.

Equilibration Mass (initial mass) /mg **Initial conc. /mM**	**LiTPFB**		**THpABr**	
	DCE	**D_2O**	**DCE**	**D_2O**
5	2.4 (3.9)	1.3 (0)	2.4 (2.5)	* (0)
10	4.4 (6.7)	2.1 (0)	4.8 (5.1)	* (0)
50	30 (38)	5.4 (0)	24.0 (26)	2.0 (0)

Table 4.11: Showing the equilibration (and initial) masses of potential–determining salts before and after partitioning across the oil–water interface. * indicates a mass less than the accuracy of the balance which was ±0.1 mg.

Table **4.11** shows that The effect of the ions on the stability of the system was then assessed by comparing with an emulsion of DCE–in–1.5 M sucrose D_2O. For this, emulsions containing 5 mM LiTPFB or THpABr, DCE–in–1.5 M sucrose, D_2O and DCE only–in–1.5 M sucrose, D_2O were created as in **2.4**. Once the emulsions had cooled to 15 °C for 30 mins, samples were taken for analysis using optical microscopy and the bulk emulsion was maintained at 15 °C in the waterbath. Measurements were made of the initial drop volume, using optical microscopy as outlined in **2.6**, and then subsequent, fresh samples were measured every hour for 5 hours. The change in drop volume with time can be seen in Figure **4.12** and it is clear that the salts have a significant effect on the stability of the emulsion drop volume.

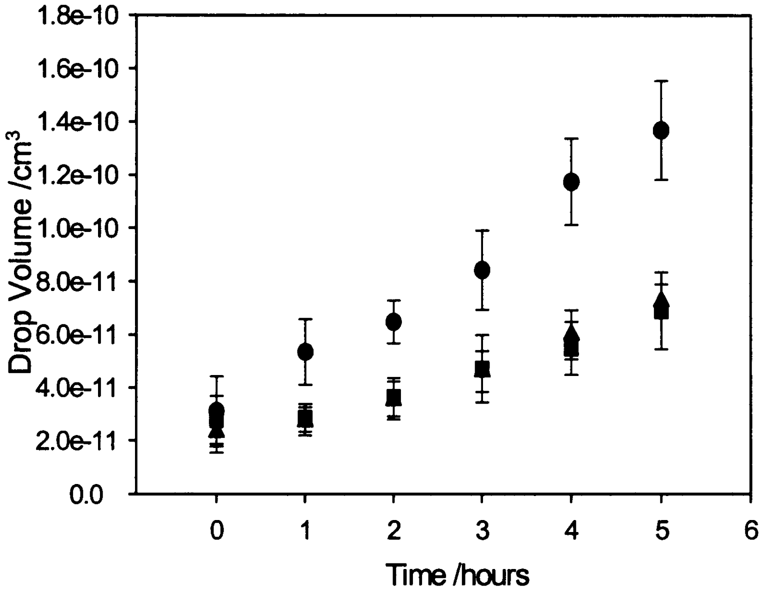

Figure 4.12: Change in drop volume vs. time for DCE–in–D_2O emulsion systems containing 1.5 M sucrose with no salts (•), THpABr (■) and LiTPFB (▲).

After the first two hours there was no detectable change in the drop volume when salts were present, yet there was a doubling of the drop volume in the absence of stabilising salts. This improved stability was a direct result of the addition of salts to reduce coalescence and it appears that the identity of the salts has no effect. This may be due to LiTPFB and THpABr setting–up similar interfacial potentials.

Using the same procedure, the drop volume and number density were measured again after 20 hours. The number densities for the emulsions were also measured, initially, and, adding these to the data from Table **4.6**, are shown in Table **4.12**. This compares the initial and final drop volumes and number densities for emulsions containing a two–salt stabilisation system (average of $TBuA^+$ and TEA^+ data from Table **4.6**), a single–salt system (average of LiTPFB and THpABr) and an emulsion containing sucrose only. Also included in Table **4.12**, is the data for LiTPFB and THpABr before averaging. The average drop diameter, in µm, has also been calculated and this is presented in brackets below the value for the drop volume in cm^3.

Emulsion Stabilisation	**Initial**		**After 20 Hours**	
	Drop Volume /μm^3 (Drop Diameter)	**Number Density /$x10^6$ drops cm^{-3}**	**Drop Volume /μm^3 (Drop Diameter)**	**Number Density /$x10^6$ drops cm^{-3}**
LiTPFB + sucrose	25 ±6 (3.6 ±0.2 µm)	200 ±24	80 ±50 (5.2 ±1.0 µm)	26 ±1
THpABr + sucrose	23 ±7 (3.5 ±0.3 µm)	170 ±19	66 ±10 (5.0 ±0.2 µm)	24 ±9
Single–Salt System	**24 ±7** (3.6 ±0.3 µm)	**185 ±22**	**73 ±30** (5.1 ±0.6 µm)	**25 ±5**
Two–Salt System	**26 ±5** (3.7 ±0.2 µm)	**140 ±18**	**145 ±66** (6.4 ±0.9 µm)	**8 ±6**
Sucrose only	**25 ±5** (3.6 ±0.2 µm)	**140 ±12**	**180 ±35** (7.0 ±0.4 µm)	**7 ±6**

Table 4.12: Comparing the average initial drop volume and number density with measurements taken after 20 hours, for emulsions containing sucrose and LiTPFB or THpABr. This data is averaged to give results for a single–salt system and is compared with data from Table **4.6** (for $TBuA^+$ and TEA^+ averaged to give results for a two–salt system) and an emulsion stabilised with 1.5 M sucrose only. Because these are average measurements, the standard deviation of the results is included as the error. The value in brackets below that of the drop volume in cm^3 corresponds to the average drop diameter in µm.

From comparing the two–salt and single–salt systems, it can be seen that the single–salt system drop volume is approximately half that of the two–salt emulsions after 20 hours. This suggests that the single–salt system might give better long–term stability than the two–salt, and this is also reflected in the number densities of the emulsions, with the average from the LiTPFB and THpABr emulsions being nearly triple that from the $TBuA^+$, TEA^+ and no sucrose emulsions after 20 hours. By comparing the results from Table **4.12** with those in Figure **4.12**, it can be seen that they do not correlate. The drop volume measured after 5 hours in Figure **4.12**, for the emulsions are similar to those measured after 20 hours in Table **4.12**. This was due to the different experimental techniques used; for the measurements taken every hour in Figure **4.12**, the emulsion vessel was repeatedly opened and closed causing a quantity of DCE, contained in the head space of the vessel, to be released. This led to the accelerated destabilisation of the emulsion by reducing the weight percent of DCE present in the emulsion mixture. The results in Table **4.12**, however, were measured by only opening the flask at the start of the experiment and then again after 20 hours, hence showing the emulsion to be more stable when kept in a closed vessel.

To investigate the improved stability caused by the single–salt system further, the turbidities of emulsions containing 5 mM LiTPFB or THpABr DCE–in–1.5 M sucrose D_2O, created as in **2.4**, were measured. The results are compared with turbidity vs. time results, from Figure **4.7**, for emulsions containing sucrose and $TBuA^+$, and are shown in Figure **4.13**. The initial turbidity values before normalisation were 3.26, 3.13 and 3.18 au for the emulsion stabilised using LiTPFB, THpABr and $TBuA^+$.

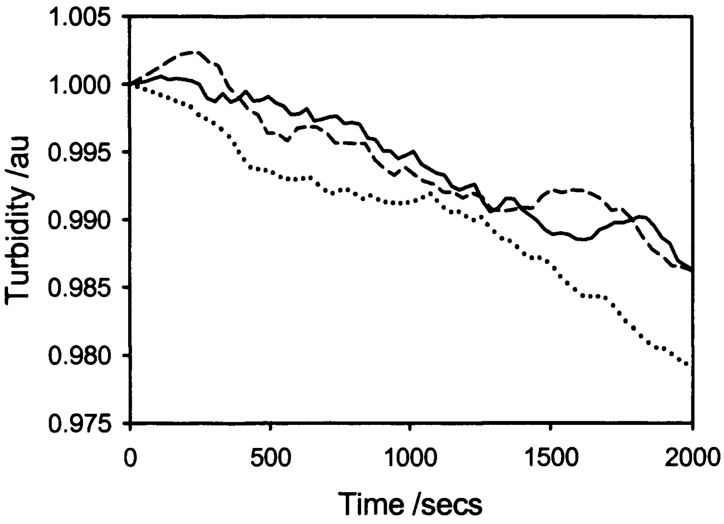

Figure 4.13: Graph comparing turbidity at 550 nm vs. time at 15 °C for emulsions containing (----) 5 mM LiTPFB DCE–in–1.5 M sucrose D_2O, (——) 5 mM THpABr DCE–in–1.5 M sucrose D_2O and (⋯⋯) 10 μM TBuATPB DCE–in–0.1 M TBuACl 1.5 M sucrose D_2O. The original turbidity values were 3.26, 3.13 and 3.18 au, and the rate of change of turbidity with time for the plots are –6.5, –6.5 and –10.2 x10^{-6} au s^{-1} for emulsions stabilised using LiTPFB, THpABr and $TBuA^+$, respectively.

From Figure **4.13**, it can be seen that the single–salt system does give greater stabilisation than the two–salt system, with the change in turbidity with time decreasing from –10.2 x10^{-6} au s^{-1} to –6.5 x10^{-6} au s^{-1} for stabilisation using $TBuA^+$ and LiTPFB and THpABr respectively. This may be because the interfacial potential is greater for the LiTPFB and THpABr emulsions.

4.3.4 Calculating the Interfacial Potential for a Single–Salt Emulsion

The interfacial potential for a single–salt system is calculated differently to that for a two–salt emulsion. For a single–salt system, the interfacial potential depends on the transfer potential of the cation and anion across the interface. Whereas in a two–salt system, the interfacial potential follows Equation **4.1** and is dependent on the transfer potential, activity coefficient and concentration of the 'common ion' only, in both the oil and water phases. Equation **4.1** is therefore not valid for a single–salt system and is rewritten to give the interfacial distribution potential, $\Delta_O^W\phi$, for a single–salt emulsion, shown as Equation **4.12** [74&88]. This was introduced in **1.1.2** as Equation **1.8**.

$$\Delta_O^W\phi = \frac{\Delta_O^W\phi_+^o + \Delta_O^W\phi_-^o}{2} + \frac{RT}{2F}\ln\frac{\gamma_+^O\gamma_-^W}{\gamma_+^W\gamma_-^O} \qquad \mathbf{4.12}$$

Where $\Delta_O^W\phi_+^o$ and $\Delta_O^W\phi_-^o$ are the standard ion–transfer potentials, from the water phase to the oil phase for the cation and anion respectively, and $\gamma_\pm^{W\,or\,O}$ is the activity of the cation or anion in the water or oil phase. Equation **4.12** does not depend on the final concentration (i.e. after partitioning) of the ions in the DCE drops and is therefore easily solvable providing the ion–transfer potentials and activity coefficients of the anion and cation are known.

As described in **4.3.1** or **1.1.2**, the transfer potentials can be found in the literature or, as outlined in **1.1.2**, can be measured using conventional electrochemical techniques. The data available for the single–salts, used in these experiments, is shown in Table **4.13**, where the Gibb's energy of transfer from water to oil,

$\Delta G_i^{W\to O,o}$, has been estimated for THpABr by extrapolating the data from Table **4.5**. It has not been possible to measure the Gibb's energy of transfer or standard ion–transfer potential for TPFB$^-$, due to an inability to set a potential window large enough. The value has therefore been assumed to be larger than that extrapolated for THpABr but of a similar magnitude due to their similar stabilisation effects.

Ion	$\Delta_O^W \phi_i^o$ /mV	$\Delta G_i^{W\to O,o}$ /kJ mol^{-1}
THpA$^+$	–610	–59
Br$^-$	398	38.4
Li$^+$	576	55.6
TPFB$^-$	–620	–60

Table 4.13: Literature standard ion–transfer potentials, $\Delta_O^W \phi_i^o$, and the standard Gibb's energy of transfer, $\Delta G_i^{W\to O,o}$, for Br$^-$ and Li$^+$ [78] and estimated values for THpA$^+$ and TPFB$^-$.

To calculate the interfacial potential, the activity coefficient has to be determined. From **4.3.2**, the minimum distance of ion separation is found to be q = 27.84 Å for DCE and q = 3.71 Å for D_2O at 15 °C, using the Bjerrum Equation, Equation **4.6**. The ionic radii of each stabilising ion are shown in Table **4.14**, as are the sum of the ionic radii, used as a in the Debye–Hückel Law, Equation **4.7**.

From Table **4.14**, it can be seen that for the aqueous salts $a > q$ and that, as described in **1.1.2**, the calculated activity coefficient will follow the Debye–Hückel Law. For the organic salts, however, $a < q$, showing that ion–association will occur within the DCE phase and that the activity coefficient will not be unity.

Stabilising Ion	**Ionic Radii /Å**	**Stabilising Salt**	**Sum of Ionic Radii (a) /Å**
$THpA^+$	6.31*	**$LiTPFB_{(aq)}$**	6.17
Li^+	0.60 [188]	**$THpABr_{(aq)}$**	8.26
Br^-	1.95 [188]	**$LiTPFB_{(org)}$**	6.17
$TPFB^-$	5.57*	**$THpABr_{(org)}$**	8.26

Table 4.14: Showing the ionic radii, and sum of the ionic radii for the single–salt systems used in emulsion stabilisation. *The value of a for $THpA^+$ was estimated by extrapolating data for tetraalkylammonium ions from [187] and the value for $TPFB^-$ was estimated by using the sum $a_{TPFB^-} = a_{TPB^-} + a_{F^-}$ (1.36 Å [188])

For the aqueous salts, the activity coefficients were calculated using the Debye–Hückel Law in Equation **4.7** and the parameters m_i, z_i and $\sqrt{I}$ for the different aqueous single–salt used, are 5 mM, ±1 and 0.071, respectively, for both $LiTPFB_{(aq)}$ and $THpABr_{(aq)}$. Using Equation **4.7**, the calculated activity coefficients are then determined to be $\gamma_{\pm}^{W} = 1$, for $LiTPFB_{aq}$ and $THpABr_{aq}$.

Because $a < q$, for the ions in the DCE phase, the activities will not be equal to unity due to the occurrence of ion–association. However, by assuming that $\gamma_{+}^{O} = \gamma_{-}^{O}$ and $\gamma_{\pm}^{W} = 1$, Equation **4.11** can be simplified to Equation **4.13**.

$$\Delta_{O}^{W}\phi = \frac{\Delta_{O}^{W}\phi_{+}^{o} + \Delta_{O}^{W}\phi_{-}^{o}}{2} \qquad \textbf{4.13}$$

The distribution potentials have been calculated to be –106 and –22 mV for THpABr and LiTPFB stabilised emulsions respectively. It can therefore be seen that the interfacial potentials for the LiTPFB and THpABr emulsions are much lower than those estimated for the two–salt system using $TBuA^+$ and TEA^+ (–474 and –

205 mV respectively). These contradict the greater emulsion stability seen when using the single–salt and suggest that the extra stability comes from an additional factor to the interfacial potential. This could be because the single–salt systems lower the surface tension between the DCE and D_2O, similar to the manner in which surfactants work. It has been reported that the surface tension can increase or decrease when in the presence of electrolytes [191] and is a function of the activity of the bulk solution, therefore if the solution activity is increased, the surface tension will decrease.

Another reason why the value obtained for the potential is very small, would be that there was an error in the calculation. Considering the large amount of experimental data suggesting that both single–salt emulsions have a value >400 mV, it is therefore thought that Equation **4.13** is inaccurate or that underestimates have been made for the Gibbs energy of transfer of $TPFB^-$ and $THpA^+$.

Because the concentration of the salt in the aqueous emulsion phase is unknown it is not possible to calculate the Debye–Length. It is however thought that this will be of the same order of magnitude or less than that of the two-salt emulsion, <1 nm, and therefore this would be much less than the emulsion separation distance of 17 µm, supporting the DLVO theory of emulsion stability.

4.4 Temperature Effects on the Salt–Stabilised Emulsion

In **3.3.3**, it was shown that the emulsion drop volume is sensitive to temperature changes, due to the changes in solubility of the two phases in each other. To investigate if the stabilising salts affect the solubility of DCE in D_2O, and hence the sensitivity of the drop volume to temperature, the drop volume at different temperatures was measured for the stabilising salt–systems studied. Emulsions were made as described in **2.4** containing: DCE–in–D_2O only, 10 μM TEATPB DCE–in–0.1 M TEACl D_2O, 10 μM TBuATPB DCE–in–0.1 M TBuACl D_2O, 5 mM LiTPFB DCE–in–D_2O and 5 mM THpABr DCE–in–D_2O. 1.5 M sucrose was included in all the emulsions to improve stability and once the emulsions had cooled to 15 °C for 30 mins, a sample was taken for analysis using optical microscopy, as in **2.6**. The measured drop volume was then converted to DCE weight percent using the measured initial number densities in Tables **4.6** and **4.12**, and this was plotted versus temperature for each system in Figure **4.14**. From this figure, it can be seen that the DCE drop weight percent, and hence drop volume, is inversely proportional to temperature and that the emulsions respond to the temperature change in a similar manner irrespective of the stabilising salt. This is because the drop volume is dependent on the solubility only, which in turn is reliant on the temperature of the system. The salts also seem to have a negligible effect on the change in solubility with temperature for DCE in D_2O.

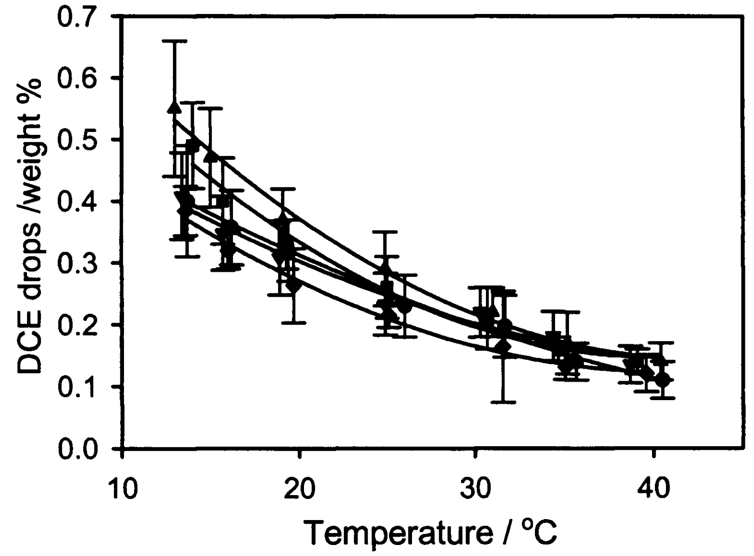

Figure 4.14: DCE weight percent vs. temperature for emulsions containing: (◆) DCE–in–D_2O only (y=0.08+0.8exp$^{-0.07x}$), (●) 10 μM TEATPB DCE–in–0.1 M TEACl D_2O (y=–0.2+0.8exp$^{-0.03x}$), (▼) 10 μM TBuATPB DCE–in–0.1 M TBuACl D_2O (y=0.07+0.7exp$^{-0.05x}$), (▲) 5 mM LiTPFB DCE–in–D_2O (y=0.07+1.1exp$^{-0.07x}$) and (■) 5 mM THpABr DCE–in–D_2O (y=0.1+1.2exp$^{-0.09x}$). 1.5 M sucrose was included in all the emulsions to improve stability and the fitted regression line equations are included in brackets for each emulsion.

The data from Figure **4.14**, at 15 °C was then used in Table **4.15** to show the initial weight percent of DCE present as emulsion drops, for each system, and it can be seen that TEA^+ and $TBuA^+$ have a minimal effect on the solubility of DCE in D_2O, but THpABr and, in particular LiTPFB, cause an increase in the weight percent of DCE present as emulsion drops. This supports the theory that the single–salt systems affect the surface tension between DCE and D_2O, therefore causing an overall increase in the solubility of the two phases. This increase in solubility is seen as an increase in number density due to the increase in the nucleation rate as described in **1.2.3**.

Stabilisation System	**Weight Percent DCE**
DCE–in–D_2O only +sucrose	0.38 ±0.06
TEA^+ + sucrose	0.40 ±0.09
$TBuA^+$ + sucrose	0.41 ±0.10
THpABr + sucrose	0.49 ±0.13
LiTPFB + sucrose	0.55 ±0.14

Table 4.15: Showing the weight percent of DCE condensed as emulsion drops, for emulsions containing: DCE–in–D_2O only, 10 μM TEATPB DCE–in–0.1 M TEACl D_2O, 10 μM TBuATPB DCE–in–0.1 M TBuACl D_2O, 5 mM LiTPFB DCE–in–D_2O and 5 mM THpABr DCE–in–D_2O. 1.5 M sucrose was included in all the emulsions to improve stability

4.5 Measuring the Zeta–Potential of the Emulsion Interface

The zeta–potential is not the "true" interfacial potential and is instead measured at the slip or shear plane. This is explained more fully in **1.2.4** but consists of a layer of charged ions that form at the interface and move with the DCE drop in solution. Although it is not the exact value of the interfacial potential, it is useful in the explanation of electrostatic interactions in the emulsion.

The zeta–potential measurements were carried out using a DELSA zeta–potential analyser at the Beckman Coulter Particle Characterisation Group in High Wycombe. The emulsions tested were DCE–in–D_2O only, DCE–in–1.5 M sucrose D_2O, 0.1 mM TEATPB DCE–in–0.1 M TEACl 1.5 M sucrose D_2O, and 10 μM TEATPB DCE–in–0.1 M TEACl 1.5 M sucrose D_2O. All emulsions were created following the procedure in **2.4** and, once they had cooled to 35 °C for 30 mins, the samples were analysed. The emulsions were cooled to 35 °C and not 15 °C to produce drops with a small volume. This was so an attempt could be made to measure the emulsion drop size when in the DELSA.

The two emulsions that did not contain ions gave no zeta–potential reading, as expected because there was no potential set–up at the interface from potential–determining salts. There would, however, be a slight potential as reported for the DCE/H_2O interface [135], but this would be below the accuracy of the DELSA.

The emulsion samples that contained potential–determining ions gave very interesting results of two peaks either side of zero, Figures **4.15** and **4.16**. For these measurements the DELSA was set at 35 °C, but the attempt to measure the size was unsuccessful because the drops were still too big at 35 °C to be detected by the DELSA.

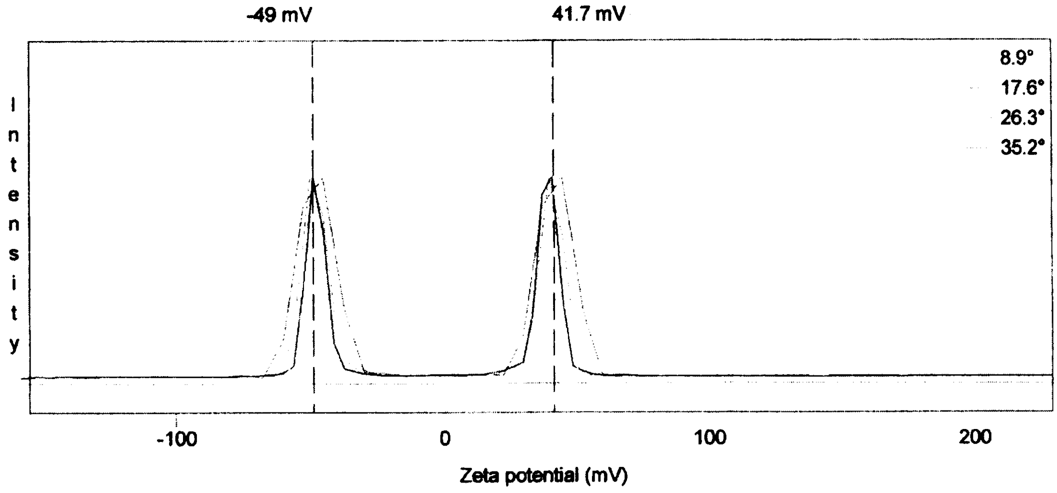

Figure 4.15: Graph showing the zeta–potential measurement of a sample of 0.1 mM TEATPB DCE–in–0.1 M TEACl 1.5 M sucrose D_2O measured at 35 °C.

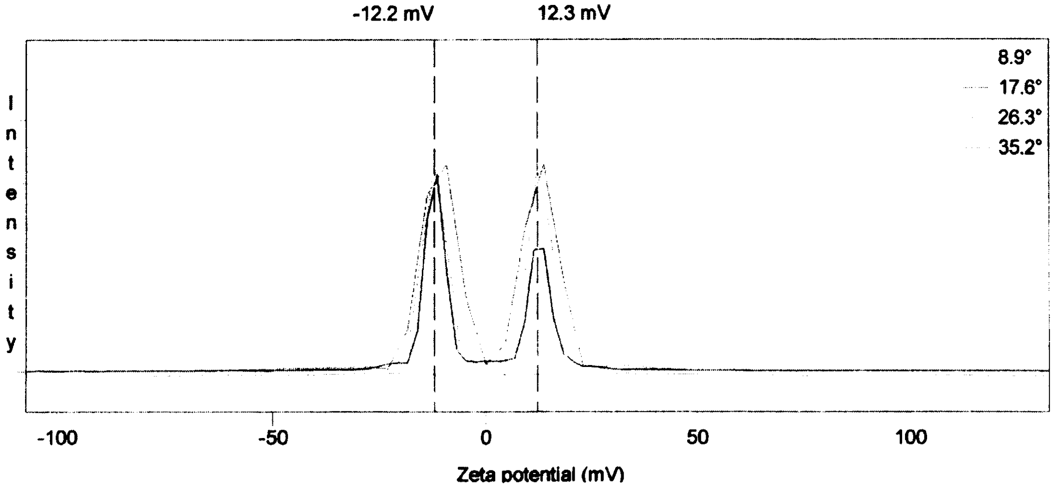

Figure 4.16: Graph showing the zeta–potential measurement of a sample of 10 μM TEATPB DCE–in–0.1 M TEACl 1.5 M sucrose D_2O measured at 35 °C.

The conductivities of the two samples were also measured by the DELSA, giving values of 3.51 and 3.44 m S cm^{-1} for Figures **4.15** and **4.16** respectively. It can be seen that the conductivities of the two samples were similar, due to their comparable drop volume, whereas the zeta–potential readings were different, and it was proposed that this was due to the different TEATPB concentrations in the two emulsions. The reason for the two, almost identical, positive and negative peaks is unknown, but may be an experimental artefact caused by the transparent and perfectly spherical emulsion drops. The unique nature of the interfacial potential established; namely two diffuse double layers, may also contribute to the two peaks. The zeta–potential was also measured using a Malvern Zeta–Sizer 3000. The different emulsions analysed at 15 °C, were DCE–in–D_2O, 10 μM TEATPB DCE–in–0.1 M TEACl D_2O, 5 mM LiTPFB DCE–in–D_2O and 5 mM THpABr DCE–in–D_2O, created as in **2.4**. 1.5 M sucrose was included, in all the emulsions tested, to improve stability and the results are shown in Table **4.16**.

Emulsion Stabilisation	**Zeta Potential Measurement /mV**			
	1	**2**	**3**	**4**
No Salts	−2.6 ±4.4	−0.3 ±9.3	–	–
TEA^+	−2.6 ±0.9	−2.7 ±0.7	–	–
LiTPFB	−25.8 ±6.1	−3.5 ±0.2	−0.2 ±6.2	−0.4 ±2.3
THpABr	−3.8 ±4.5	−3.4 ±1.2	–	–

Table 4.16: Table showing measured Zeta–Potentials for emulsion samples containing: DCE–in–D_2O (No Salts), 10 μM TEATPB DCE–in–0.1 M TEACl D_2O (TEA^+), 5 mM LiTPFB DCE–in–D_2O (LiTPFB) and 5 mM THpABr DCE–in–D_2O (THpABr). 1.5 M sucrose was included in all samples to improve stability. The different zeta–potential values for each stabilisation system correspond to multiple measurements at 15 °C.

From Table **4.16**, it can be seen that the Zeta–Sizer gave inconsistent results. The values for TEA^+ also do not correlate with those determined using the DELSA, and the Zeta–Sizer was also unable to confirm the ‘double peaks’. This was thought to be due to the way the data was presented; the DELSA gave the results as a graph of zeta potential vs. intensity, enabling the two peaks to be seen, whereas the Zeta–

Sizer presented only the maximum zeta potential for each run, thereby ignoring any possible second maximum. For the DELSA results, the peaks seen were of almost equal intensity at positive and negative zeta. This would not be reflected in the Zeta–Sizer readings and may explain the low, inconsistent results using the Zeta–Sizer, if the average peak intensity was recorded. Also, the Zeta–Sizer used an "injection" system to introduce the sample into the analyser and it is believed that this would cause a large degree of shear. This has been shown in Chapter **3**, to rapidly destabilise the emulsion and it is thought that this would have occurred for all the zeta–potential measurements using the Zeta–Sizer. When using the DELSA, a method was employed for "dripping" the emulsion into the sample chamber and so the emulsion would have experienced less shear force using this technique. Because of this, it is believed that the DELSA gave more reliable results but, due to the "double peaks", a quantitative value for the zeta–potential cannot be determined for the emulsion systems. The results do show, however, that there is a potential established at the interface and confirm the presence and effect of the potential–determining salts. Because it has not been possible to measure the zeta–potential, estimations cannot be made of the Coulomb interactions and total drop interaction potential using DLVO theory.

4.6 Conclusions

From the results in **4.2**, it was seen that it was possible to reduce the effects of sedimentation using a density–altering species. It was found that 1.5 M sucrose provided good stabilisation at a lower concentration than that needed for comparable stabilisation using glucose (–23.5 x10^{-6} au s^{-1} compared with –20.7 x10^{-6} au s^{-1}). It was also found that the stability of DCE–in–D_2O, –172.6 x10^{-6} au s^{-1}, was similar to that of DCE–in–H_2O, –179.5 x10^{-6} au s^{-1}, and showed that the aqueous phase of the system is interchangeable and therefore SANS experiments could be carried out on both with minimal loss of stability in the system.

The emulsion was further stabilised in **4.3.1**, by reducing the effects of coalescence. This was achieved using the partitioning of potential–determining salts across the liquid–liquid interface. Two systems were studied: a two–salt system using TEA^+ or $TBuA^+$ as a 'common ion', and a single–salt system using the partitioning of LiTPFB or THpABr. It was found that LiTPFB gave the best stabilisation, –6.5 x10^{-6} au s^{-1}, and effectively caused insignificant changes to the emulsion drop volume over the first two hours when used in conjunction with sucrose. The interfacial potential established at the interface was estimated in **4.3.4**, to be –22 mV and this was compared to the potentials estimated for the other salt systems of –205 ±17, –474 ±19 and –106 mV for systems containing TEA^+, $TBuA^+$ and THpABr at 15 °C. The potentials were calculated using UV–Vis spectroscopy in **4.3.2**, to determine the concentration of ions in the emulsion oil drops; 0.15 mM. The difference in the magnitude of the potential between the single-salt emulsions and the two-salt emulsions is not entirely clear but may be due to the single-salts reducing the interfacial tension between the two phases. It was thought, though, that this would be insufficient to cause the significant improvement in stability and therefore it was suggested that there are terms missing from Equation **4.13**.

It was also seen in **4.4**, that the emulsions were sensitive to changes in temperature, irrespective of the stabilising salt used and that the inclusion of TEA^+ and $TBuA^+$ had an insignificant effect on the solubility of the DCE in D_2O. LiTPFB and THpABr, however, were seen to increase the solubility of DCE in D_2O and this is believed to be due to the partitioning salts lowering the surface tension between the two phases.

Calculations of the emulsion drop Debye–Length also showed that the drop interaction distance was much less than the drop separation distance as expected, following DLVO theory, and correspond to the resulting emulsion stability.

Another method used to stabilise the emulsion was by dilution, (not included). The aim was to dilute the emulsion samples to give the DCE drops a lower probability of collision and thus reduce the process of coalescence. This however, caused a decrease in the emulsion stability, likely to be due to the increase in shear caused by the mixing of the two liquids.

Attempts were also made to measure the zeta–potential at the interface in **4.5**, with some interesting results when using the DELSA. These showed that the potential changed with different organic ion concentrations and this was presented as two peaks at almost identical positive and negative potentials. It has been proposed that these could be an experimental artefact due to the perfectly spherical and transparent emulsion drops. This may result in a 'shadow' being seen by the DELSA as the drop moves in solution. The similar refractive indices of the DCE and aqueous solution may also add to the creation of this 'shadow'. Another proposition, is that these peaks are caused by the unique nature of the liquid–liquid system, i.e. because there is no solid particle with a defined positive or negative charge. Instead there is an oil drop with two separate charge layers either side of the interface. As a potential is applied to the system, a solid particle would move in the opposite direction to its net overall charge and this single movement would be seen as a positive or negative zeta–potential reading. The liquid drop, however has no net overall charge and so would be both attracted and repelled to the applied potential, causing the drop to deform and elongate, and could result in equal positive and negative zeta–potentials. Overall the emulsion was successfully stabilised using 1.5 M sucrose to reduce sedimentation and 5 mM LiTPFB to reduce coalescence. This stabilisation was then seen to be effective over the first two hours, enabling the emulsion to be studied using SANS.

Chapter 5: Small Angle Neutron Scattering Analysis of Protein Adsorption at the Oil–in–Water Emulsion Interface

5.1 Introduction

The adsorption of the protein bovine serum albumin (BSA) at the liquid–liquid interface has been investigated using small angle neutron scattering (SANS) on an oil–in–water emulsion using three different diffractometers; D11 and D22 at the Institute Laue–Langevin (ILL), France, and LOQ at the ISIS facility, UK, with the only analysable data being obtained from D11 due to the lower *Q*–range accessible.

The interfacial layer has been investigated using different isotopic solution phase contrasts and information has been obtained about the thickness of the protein layer with and without the stabilising salt LiTPFB.

The emulsion containing BSA with and without LiTPFB has also been characterised using optical microscopy, and this is compared with the emulsion composed of DCE–in–D_2O investigated in Chapters **3** and **4**.

5.2 Characterisation of the DCE–in–BSA D_2O Emulsion

As described in **1.3**, bovine serum albumin (BSA) is a well characterised protein that adsorbs to form a layer at the liquid–liquid interface [160]. This adsorbed layer has also been shown to act to stabilise emulsions [169&170] and, therefore to investigate this, DCE–in–1.5 M sucrose D_2O emulsions were created, as in **2.4**, containing: 5 mM LiTPFB in the DCE and 5 μM BSA in the D_2O, and an emulsion containing 5 μM BSA only with no salts. The emulsion drop volume was then measured initially after 30 mins cooling to 15 °C, and then every hour for 5 hours. The results were compared with those from Figure **4.12** in **4.3.3**, for DCE–in–1.5 M sucrose D_2O and 5 mM LiTPFB DCE–in–D_2O, and are shown in Figure **5.1**.

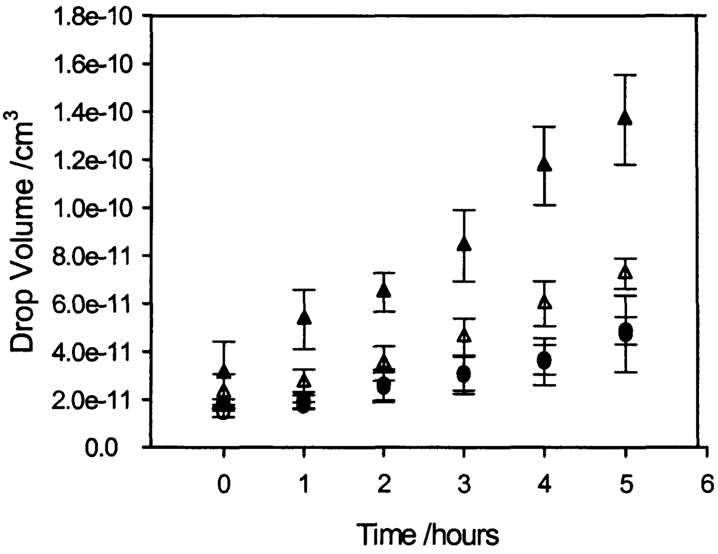

Figure 5.1: Graph showing the change in drop volume with time for DCE–in–1.5 M sucrose D_2O emulsion systems containing: (▲) no salts or protein, (Δ) 5 mM LiTPFB only, (●) 5 μM BSA and 5 mM LiTPFB and (○) 5 μM BSA only.

From Figure **5.1** it can be seen that the presence of protein causes further stabilisation of the emulsion, irrespective of the presence of stabilising salt, due to the BSA adsorbing at the liquid–liquid interface and reducing the surface energy between the two phases.

The effect of temperature changes on the emulsion containing BSA were then studied by creating emulsions containing DCE–in–1.5 M sucrose D_2O, with 5 mM LiTPFB and 5 μM BSA, and BSA only. The emulsions were heated to 65 °C and then cooled to 15 °C for 30 mins, and a sample was placed onto the microscope temperature controller for analysis as in **2.6**. The initial drop volume and number density were measured and then the temperature was increased in recorded increments from 15 to 45 °C. The results were converted to DCE drop weight percent using the measured initial number density, and compared with the data from Figure **4.14** in **4.4** for emulsions containing no salts or protein, and salts only, and these are shown in Figure **5.2**. From this figure it can be seen that the presence of BSA at the emulsion interface does not affect the solubility of DCE in D_2O and the sensitivity of the emulsion to temperature changes. The recorded number density, initial drop volume and calculated DCE weight percent, used in Figure **5.2** for the emulsions containing BSA, were then tabulated in Table **5.1** and these were compared with the data from Table **4.12** in **4.3.3** for the emulsions without protein.

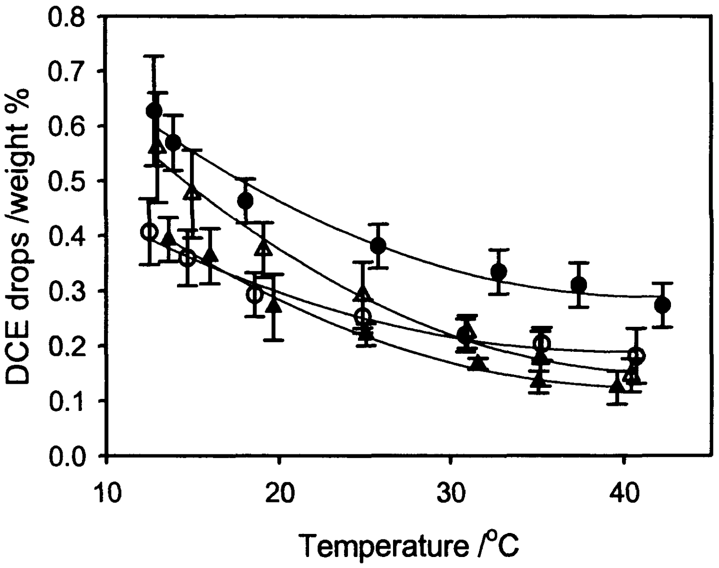

Figure 5.2: Graph showing the weight percent of D_2O as emulsion drops vs. the temperature of the system. For DCE–in–1.5 M sucrose D_2O emulsion systems containing: (▲) no salts or protein, (Δ) 5 mM LiTPFB only, (●) 5 μM BSA and 5 mM LiTPFB and (○) 5 μM BSA only.

The solid lines are the regression fits using the equations: $y=0.07+0.9\exp^{-0.07x}$ for no salts or protein, $y=0.09+1.2\exp^{-0.07x}$ for salts only, $y=0.3+1.1\exp^{-0.09x}$ for protein and salts, and $y=0.2+0.7\exp^{-0.09x}$ for protein only.

Emulsion System (+ sucrose)	**Drop Volume /μm^3**	**Number Density /x10^6 drops cm^{-3}**	**Weight Percent Emulsion Drops**
DCE–in–D_2O	25 ±5 (3.6 ±0.2 μm)	140 ±12	0.35 ±0.06
LiTPFB DCE–in–D_2O	25 ±6 (3.6 ±0.2 μm)	200 ±24	0.51 ±0.14
DCE–in–BSA D_2O	15 ±2 (3.1 ±0.1 μm)	160 ±10	0.25 ±0.03
LiTPFB DCE–in–BSA D_2O	18 ±2 (3.3 ±0.1 μm)	230 ±16	0.42 ±0.05

Table 5.1: Comparing the measured drop volume, number density and calculated weight percent of emulsion drops for emulsions containing DCE–in–1.5 M sucrose D_2O, with 5 mM LiTPFB and/or 5 μM BSA. The value in brackets below that of the drop volume in cm^3 corresponds to the average drop diameter in μm.

Table **5.1** shows that the average drop volume for emulsions containing BSA is slightly lower than that measured for emulsions without protein, and this is reflected in the weight percent of DCE condensed as emulsion drops. The weight percent is significantly lower for the DCE–in–5 μM BSA D_2O emulsion, suggesting that the protein decreases the solubility of DCE in D_2O. When LiTPFB is included in the emulsion containing BSA, the weight percent is increased due to the salt lowering the surface tension between the oil and water, but the effect of the BSA on the solubility is still noticeable due to the weight percent being less than that of the emulsion containing LiTPFB and no protein (0.42 ±0.05 and 0.51 ±0.14 wt % for LiTPFB and BSA, compared with LiTPFB only), and there appears to be a reproducible discrepancy of 0.1 wt % between the emulsions with BSA and those without, irrespective of stabilising salt.

As described in **1.3.1**, the isoelectric point of BSA is pH 4.7 [155] and the conformation of the protein structure changes with pH between the Extended, Fast, Normal, Basic and Aged forms. The pH of the aqueous emulsion phase was therefore measured with and without LiTPFB. For this, water solutions were created containing: 100 % D_2O, 50 % D_2O + 50 % H_2O, and 90.6 % D_2O + 9.4 % H_2O, all including 1.5 M sucrose, 20 μM BSA and with or without 5 mM LiTPFB. The pH of these 6 solutions was then measured and the results are shown in Table **5.2**. The different solution contrasts of D_2O and H_2O, used in this experiment, correspond to the emulsion solutions used in subsequent SANS D11 experiments.

Aqueous Solution (+ 1.5 M sucrose & 20 μM BSA)	**pH**	
	With Salts	**Without Salts**
100 % D_2O	7.84	7.27
50 % D_2O + 50 % H_2O	8.21	7.29
90.6 % D_2O + 9.4 % H_2O	8.18	7.25

Table 5.2: Showing the measured pH for emulsion aqueous phase solutions with and without stabilising LiTPFB.

From Table **5.2** it can be seen that the average pH of the emulsion aqueous phases is pH 8.1 with salts and pH 7.3 without. This suggests that the protein adsorbed at the emulsion interface would be in the Normal or Basic form depending on the presence of salts.

5.3 Principles of Small Angle Neutron Scattering

As described in **1.3.2**, small angle neutron scattering (SANS) is a simple diffraction technique that uses the considerable difference in the scattering of a neutron from hydrogen nuclei compared with that from a deuterium nucleus, to determine information about the size and shape of molecules, and this has been used successfully to investigate interfacial adsorption [58&59]. A schematic diagram of the SANS geometry is shown in Figure **5.3**.

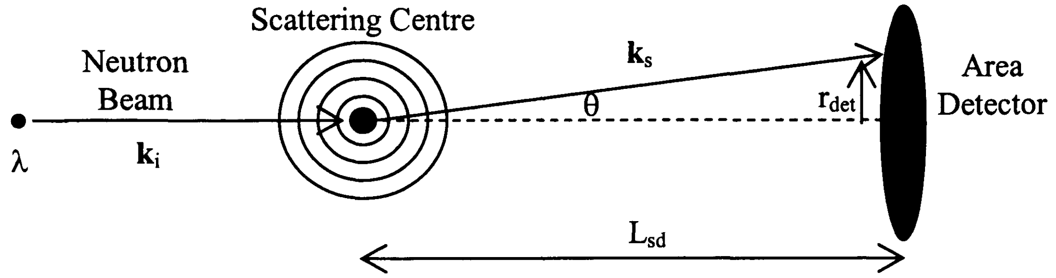

Figure 5.3: Schematic diagram showing the geometry of a SANS experiment where $\mathbf{k}_i$ and $\mathbf{k}_s$ are the incident and scattered wavevectors of neutrons with wavelength λ nm. The neutrons hit the scattering centre (hydrogen or deuterium nucleus) and are scattered through an angle θ and then recorded on a detector at a distance L_{sd} from the sample.

In Figure **5.4**, $\mathbf{k}_i = 2\pi/\lambda$, and the modulus of the scattering vector, $\mathbf{Q} = |\mathbf{k}_s - \mathbf{k}_i|$, is approximately equal to Equation **5.1** when the scattering angle is small.

$$Q = |\mathbf{Q}| = \frac{4\pi}{\lambda}\frac{r_{det}}{L_{sd}} \qquad \mathbf{5.1}$$

Where Q is the independent variable in SANS experiments and has units of length^{-1}. By substituting Equation **5.1** into the Bragg law of diffraction (Equation **5.2**), Equation **5.3** is obtained for the relationship between Q and the dimensions of the investigated system, again assuming that θ is small.

$$\lambda = 2d \sin(\theta/2) \qquad \textbf{5.2}$$

$$d = \frac{2\pi}{Q} \qquad \textbf{5.3}$$

The dependent variable measured in a SANS experiment is the intensity of scattering, $I(Q)$, with dimensions of length^{-1}, and corresponds to the flux, or more precisely, the number of neutrons of a given wavelength scattered through a particular angle, that arrive on a small area of the detector in a given time. This flux is given by,

$$I(Q) = I_0(\lambda)\Delta\Omega\eta(\lambda)T(\lambda)V_s\frac{d\Sigma}{d\Omega}(Q) \qquad \textbf{5.4}$$

Where I_0 is the incident flux, $\Delta\Omega$ is the solid angle element defined by the size of a detector pixel, η is the detector efficiency, and V_s is the volume of the sample illuminated by the neutron beam. T is the neutron transmission of the sample, given by,

$$T(\lambda) = \exp(-N\, t\sigma_{\mathrm{tot}}(\lambda)) = \exp(-\mu_m\delta_t) \qquad \textbf{5.5}$$

Where t is the sample thickness, μ_m is the mass absorption coefficient and $\sigma_{\mathrm{tot}}(\lambda)$ is the sum of the coherent, incoherent and absorption cross sections, shown in Equation **5.6**, for each constituent nuclei.

$$\sigma_{\mathrm{tot}}(\lambda) = 4\pi \sum_i [\, \sigma_{\mathrm{coh},i} + \sigma_{\mathrm{inc},i} + \sigma_{\mathrm{abs},i}(\lambda)]/4\pi \qquad \textbf{5.6}$$

In Equation **5.4**, $(\mathrm{d}\Sigma/\mathrm{d}\Omega)(Q)$ is the differential scattering cross–section and contains all the information regarding the scattering centres in the samples and can be represented by [192],

$$\frac{\mathrm{d}\Sigma}{\mathrm{d}\Omega}(Q) = NV^2(\Delta\rho)^2 P(Q)\, S(Q) + B \qquad \mathbf{5.7}$$

Where N is the number concentration of scattering centres, V is the volume of one scattering centre, $(\Delta\rho)^2$ is the contrast, $P(Q)$ is the Form factor, $S(Q)$ is the Structure factor and B is the background signal.

The contrast, $(\Delta\rho)^2$, relates to the difference in the neutron scattering length density (SLD), ρ, of each solution phase in the emulsion. Each nucleus has a specific SLD and thus the SLD for a molecule can be calculated using,

$$\rho_m = \left(\frac{\delta_m N_A}{M_m}\right)\sum_n^m \rho_n \qquad \mathbf{5.8}$$

Where ρ_m is the SLD of the molecule, δ_m is the bulk density of the molecule and M_m is the molecular mass. N_A is the Avogadro constant (6.0221×10^{23} mol^{-1}) and $\sum_n^m \rho_n$ is the sum of the coherent neutron scattering lengths of each nucleus n in molecule m.

One of the main principles of SANS arises because the neutron scattering length for hydrogen and deuterium are significantly different, -3.74 and $+6.67 \times 10^{-13}$ cm for ^{1}H and ^{2}D respectively, and therefore isotopic substitution can cause a 180° phase shift in the scattering. This in turn causes different scattering patterns for the molecule, depending on the isotope, and results in different structural information being obtained. The contrast of the emulsion is merely the difference in the SLD between the DCE and the aqueous phase, $(\Delta\rho)^2 = (\rho_{DCE} - \rho_{aq})^2$. To simplify the scattering patterns from the emulsion, the SLD of the phases can be matched. This effectively reduces the 3–phase emulsion, DCE–BSA–aqueous, to a 2–phase system and is illustrated in Figure 5.4.

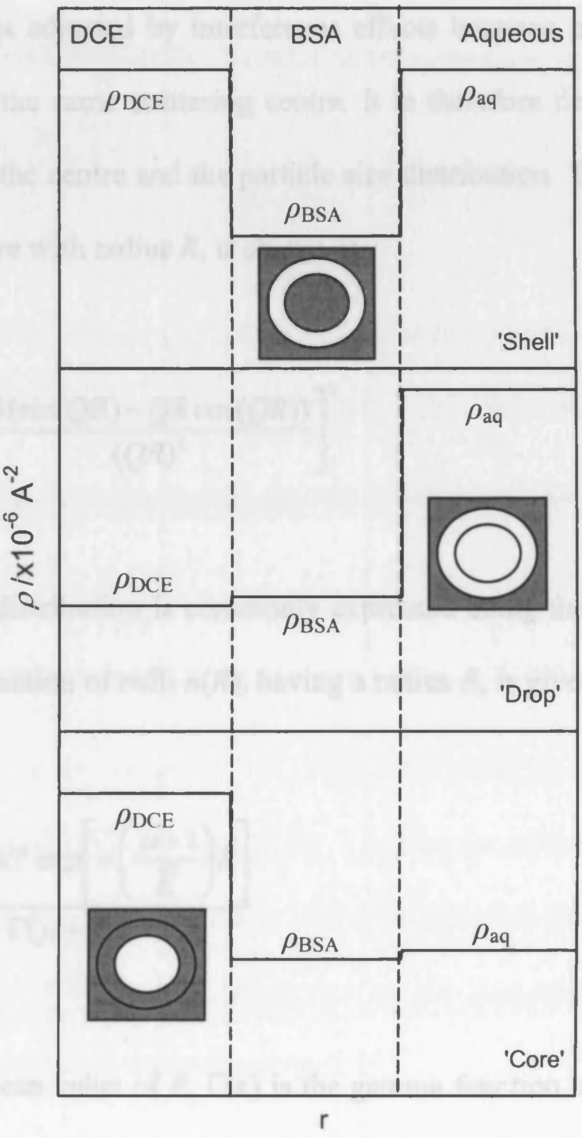

Figure 5.4: Diagram showing the SLD profile vs. distance r for the three ideal phase contrasts: 'shell', 'drop' and 'core'. Schematics of emulsion drops are also included to show in grey the areas where the SLD is matched, effectively isolating the area in white.

The most important contrast in Figure **5.4** is where the SLD of the DCE is matched to that of the aqueous phase, $\rho_{\mathrm{DCE}} = \rho_{\mathrm{aq}} >> \rho_{\mathrm{BSA}}$. This gives information on the interfacial layer of protein and is termed the 'shell' contrast. The two other contrasts, termed 'drop' and 'core' respectively, are ideally when $\rho_{\mathrm{DCE}} = \rho_{\mathrm{BSA}} << \rho_{\mathrm{aq}}$ and $\rho_{\mathrm{DCE}} >> \rho_{\mathrm{BSA}} = \rho_{\mathrm{aq}}$.

The Form factor in Equation **5.7**, *P*(*Q*), is a dimensionless function that describes how (dΣ/dΩ)(*Q*) is adjusted by interference effects between neutrons scattered by different parts of the same scattering centre. It is therefore dependent on both the size and shape of the centre and the particle size distribution. The Form factor for a homogenous sphere with radius *R*, is shown as,

$$P(Q) = F^2(Q) = \left[\frac{3(\sin(QR) - QR\cos(QR))}{(QR)^3}\right]^2 \qquad \mathbf{5.9}$$

The particle size distribution is commonly expressed using the Schultz distribution [193] where the fraction of radii *n*(*R*), having a radius *R*, is given by,

$$n(R) = \frac{\left(\frac{\mu+1}{\bar{R}}\right)^{\mu+1} R^{\mu} \exp\left[-\left(\frac{\mu+1}{\bar{R}}\right)R\right]}{\Gamma(\mu+1)} \qquad \mathbf{5.10}$$

Where $\bar{R}$ is the mean value of *R*, Γ(x) is the gamma function, and μ is the width of the distribution, given in Equation **5.11**. β is the standard deviation of the distribution.

$$\mu = \frac{\left(1 - \frac{\beta^2}{\overline{R}^2}\right)}{\frac{\beta^2}{\overline{R}^2}} \qquad \textbf{5.11}$$

The corresponding molecular weight distribution, *n*(*M*), is shown in Equation **5.12**.

$$n(M) = \frac{M^h \exp\left[-(1+h)\frac{M}{M_w}\right]}{\Gamma(1+h)\left(\frac{M_w}{1+h}\right)^{1+h}} \qquad \textbf{5.12}$$

Where M_w is the weight–average molecular weight and *h* is the polydispersity index, given in Equation **5.13**. M_n is the number–average molecular weight.

$$h = \left(\frac{M_w}{M_n} - 1\right)^{-1} \qquad \textbf{5.13}$$

The Structure factor in Equation **5.7**, *S*(*Q*), is similar to the Form factor but describes how (dΣ/dΩ)(*Q*) is altered by interference effects between neutrons scattered by different scattering centres in the sample. It is therefore dependent on the degree of local order in the sample and on the interaction potential between scattering centres, and is given by Equation **5.14**.

$$S(Q) = 1 + \frac{4\pi N}{QV_s}\int_0^{\infty}[g(r) - 1]r\sin(Qr)\ \mathrm{d}r \qquad \textbf{5.14}$$

Where $g(r)$ is a density distribution function, whose maxima corresponds to the distance r, of each nearest neighbour coordination shell. The Structure factor is not easily solvable and therefore, when the observed SANS data is fitted, an approximate form from theoretical models is generally used [192].

Once the raw data has been collected, it is normalised to get the absolute scattering intensity. For the data collected at the ILL, this follows Equation **5.15**.

$$\left(\frac{\mathrm{d}\Sigma}{\mathrm{d}\Omega}\right)(Q)_{\mathrm{s}} = \frac{\left[\frac{I(Q)_s}{T_s M_s} - \frac{I(Q)_{ec}}{T_{ec} M_{ec}}\right]}{\left[\frac{I(Q)_{H_2O}}{T_{H_2O}} - \frac{I(Q)_{ec}}{T_{ec} M_{ec}}\right]} \left(\frac{\mathrm{d}\Sigma}{\mathrm{d}\Omega}\right)(Q)_{\mathrm{H_2O}} \qquad \mathbf{5.15}$$

The subscripts *s*, *ec* and H_2O, correspond to the sample runs, empty cell and H_2O normalisation runs, respectively. $I(Q)$ is the scattering data, T, the transmission runs, and M is the recorded monitor count. Data collected at the ISIS facility is normalised using a similar equation except an instrument dependent scaling factor is used instead of the H_2O dependent terms.

5.3.1 Calculating the Molecular Scattering Length Densities

The molecular scattering length density (SLD) for each solution phase was calculated using Equation **5.8**, and the coherent scattering lengths and molecular mass for each nucleus used in the SANS experiments is shown in Table **5.3**.

Nucleus	ρ_n **/x10^{-13} cm**	**M$_n$ /g mol^{-1}**
^{1}H	-3.741	1.008
^{2}D	+6.671	2.014
C	+6.646	12.011
O	+5.803	15.999
Cl	+9.577	35.453

Table 5.3: Showing the coherent scattering length (ρ_n) and molecular mass (M_n) for each atom used to calculate the molecular SLD (ρ_m) of molecules used in the SANS experiments.

The bulk density of sucrose was determined by weighing 1.5 M sucrose (12.836 g) into a 25 cm^3 volumetric flask and filling to the line with a recorded volume of D_2O (16.55 cm^3). This corresponds to 12.836 g sucrose being equal to 8.45 cm^3 volume and therefore, the bulk density is 1.519 g cm^{-3} in D_2O, using Equation **5.16**.

$$\delta_m = m / V \qquad \textbf{5.16}$$

Where δ_m is the bulk molecular density of a substance, calculated using a recorded mass of the substance, m, displacing a measured volume of liquid, V. In H_2O, 12.836 g sucrose was equal to 7.7 cm^3 volume, and hence gave a bulk density of 1.667 g cm^{-3} of sucrose in H_2O.

Table 5.4 shows the determined and literature [186] bulk molecular densities (δ_m) and the calculated sum of the coherent neutron scattering lengths of each nucleus *n* in molecule *m* ($\sum_n^m \rho_n$) for the emulsion components, used to calculate the emulsion phase SLD.

Molecule	δ_m /g cm^{-3}	$\sum_n^m \rho_n$ /x10^{-12} cm	M_m /g mol^{-1}	ρ_m /x10^{10} cm^{-2}
Sucrose$_{D2O}$ ($C_{12}H_{22}O_{11}$)	1.519	+6.1283	342.297	1.6377
Sucrose$_{H2O}$	1.667	+6.1283	342.297	1.7973
D_2O	1.105	+1.9145	20.027	6.3614
H_2O	0.998	–0.1679	18.015	–0.5601
d-DCE ($C_2D_4Cl_2$)	1.250	+5.913	102.984	4.3221
h-DCE ($C_2H_4Cl_2$)	1.235	+1.7482	98.96	1.3139

Table 5.4: Showing the determined and literature [186] bulk molecular densities (δ_m), molecular masses (M_m) and the calculated sum of the coherent neutron scattering lengths of each nucleus *i* in molecule *m* ($\sum_n^m \rho_n$) and the calculated molecular SLD (ρ_m) for each emulsion components.

The SLD of the aqueous emulsion phases will be a sum of both the SLD of the sucrose and the D_2O or H_2O. Because 1.5 M sucrose in 25 cm^3 is 8.45 cm^3 sucrose and 16.55 cm^3 D_2O, it was determined that a 1.5 M sucrose solution was 33.8 % sucrose and 66.2 % D_2O. Therefore the SLD for D_2O containing 1.5 M sucrose was calculated to be 4.7648 x10^{10} cm^{-2} for 1.5 M sucrose D_2O. For H_2O, the experiment was repeated and it was found that 12.839 g sucrose equalled 7.7 cm^3 H_2O, hence the bulk density was 1.667 g cm^{-3} and a 1.5 M sucrose H_2O solution was 30.8 % sucrose and 69.2 % H_2O. This gave a SLD of 0.1660 x10^{10} cm^{-2} for a solution of 1.5 M sucrose H_2O.

5.3.2 Calculating the BSA Concentration Needed to Form an Emulsion Interfacial Monolayer

For the SANS experiments investigating protein adsorption, the concentration of BSA used needed precise calculation; too little and there would be insufficient to form a monolayer around all the emulsion drops, too much and it could form a bilayer.

To calculate the total surface area of the DCE drops per unit volume (A_E), Equation **5.17** was used.

$$A_E = 4\pi r^2 N \qquad \textbf{5.17}$$

Where r is the average drop radius and N is the number density and, for an emulsion containing BSA, the average total surface area was calculated to be 6.17 ±1.5 x10^{17} Å^2. As described in **1.3.1**, there are two reported dimensions for BSA; 140 x 40 x 40 Å [155] and 84 x 84 x 31.5 Å [159], the maximum surface area of a BSA unit (A_{BSA}) was also reported to be 7070 Å ^{2} [155], approximately the average of these two suggested dimensions, and, using Equation **5.18**, the number of BSA units needed to form an emulsion monolayer (N_{BSA}) was calculated.

$$N_{BSA} = \frac{A_E}{A_{BSA}} \qquad \textbf{5.18}$$

From Equation **5.18**, it is determined that 8.7 ±1.7 x10^{13} BSA units were needed for a monolayer and, using the molecular mass of BSA (M) to be 66500 g mol^{-1} [155]

and the Avogadro constant ($N_A = 6.0221 \times 10^{23}$ mol^{-1} [91], this number of units was converted to the number of moles of BSA (M_{BSA}) (Equation **5.19**).

$$M_{BSA} = \left(\frac{N_{BSA}}{N_A}\right)M \qquad \textbf{5.19}$$

The number of moles BSA needed was calculated, using Equation **5.19**, to be 9.6 ±1.5 μM and therefore to ensure an excess and allow for BSA feely dissolved in the aqueous phase of the emulsion, it was determined that 20 μM BSA were needed to give a monolayer, but would be insufficient to form a bilayer.

5.4 ILL D11 Results

The experimental data collection using D11 was carried out at two detector distances, 8 and 34 m, because, as described in **2.7**, D11 is a fixed–wavelength instrument, set at 13 Å, and this gave a greater *Q*–range than if only one detector distance was used. The two sets of data were then merged together to give one continuous set of data.

To achieve the 'drop' phase contrast, h–DCE and D_2O were used in an emulsion containing h–DCE–in–1.5 M sucrose 20 μM BSA D_2O. For the 'shell' contrast, the SLD of the aqueous phase was matched to that for d–DCE using a mixture of 1.5 M sucrose D_2O and H_2O. This was calculated to be 0.903 mole fraction 1.5 M sucrose D_2O and the emulsion was composed of d–DCE–in–1.5 M sucrose 20 μM BSA 0.903 mole fraction D_2O 0.097 mole fraction H_2O. Because the SLD of the BSA was unknown, the 'core' contrast was made to be d–DCE and a mixture of D_2O and H_2O matched to a value just below the expected SLD of the BSA, 2.5×10^{-6} Å^{-2} [160]. This contained 0.5 mole fraction H_2O and 0.5 mole fraction D_2O, with a calculated SLD of 2.4738×10^{-6} Å^{-2} and the emulsion was created composed of d–DCE–in–1.5 M sucrose 20 μM BSA 0.5 mole fraction D_2O 0.5 mole fraction H_2O. These phase contrasts were repeated with the inclusion of 5 mM LiTPFB in the DCE to investigate the inclusion of stabilising salts on the interfacial protein layer. The SLD profiles for all the D11 experiments are shown in Figure **5.5**.

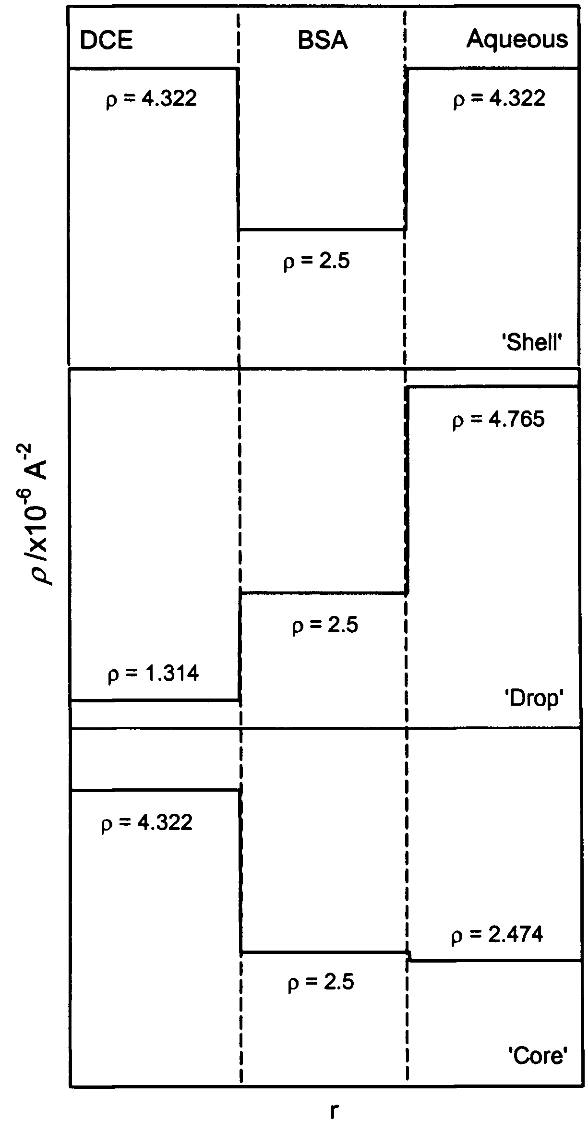

Figure 5.5: Diagram showing the SLD profile vs. distance r for the three phase contrasts: 'shell', 'drop' and 'core' used in the ILL D11 SANS experiments for an emulsion with a layer of BSA adsorbed at the liquid–liquid interface.

From Figure 5.5, it can seen that the three contrasts used in the D11 experiments were close to the 'ideal' cases and therefore information regarding the interfacial layer would be obtainable from the SANS data.

For the D11 SANS experiments, the emulsions were prepared containing 5 cm^3 aqueous solution and 0.5 cm^3 DCE. These were heated with stirring to 65 °C for 55 mins and then 0.05 cm^3 of BSA stock solution was added and the mixture was heated for a further 5 mins. The BSA solution was added towards the end of the heating time so that the protein structure remained reasonably intact. Some unfolding would occur, due to the presence of the DCE, but it was hoped that this could be limited by controlling the heating time. As described in **1.3.1**, BSA is known to partially unfold in certain conditions, but that this is also reversible [160]. It was therefore proposed that, even if some unfolding occurred whilst the BSA was heated, this would be reversed as the emulsion cooled and the BSA would retain some of its original globular shape at the liquid–liquid interface. Because there were no obvious signs of precipitation in the emulsion samples, it was assumed that the BSA had not denatured during emulsion formation.

While the emulsion was heated, the cuvette to be used was placed in the water–bath at 65 °C to heat to the same temperature. A sample was then taken of the 'hot' emulsion and placed into the cuvette, as described in **2.7**, and so as to reduce destabilisation due to shear, this was subsequently cooled in a water–bath set at 15 °C to form the emulsion. After 5 mins, the sample was then placed in the neutron beam and the scattering and transmission were recorded.

As described, the match–point for the 'shell' contrast was calculated to be 0.903 mole fraction D_2O in a solution of 1.5 M sucrose D_2O/H_2O. There would, however, be some solvent penetration of the oil into the water and vice versa, and also into the protein layer, and so the match–point needed to be confirmed experimentally. This was done by creating emulsions containing 0.5 cm^3 d–DCE and the following mole fractions of D_2O in 5 cm^3 of D_2O/H_2O: 0.950, 0.920, 0.890 and 0.850. The integrated scattering intensity was calculated for each mole fraction of D_2O, using Equation **5.20** and this was plotted in Figure **5.6**.

$$\text{Integrated Scattering Intensity} = (\text{Count rate} / \text{Sample Transmission})^2 \qquad \textbf{5.20}$$

Two lines of regression were drawn and then equated to give the corresponding mole fraction of D_2O where the lines crossed.

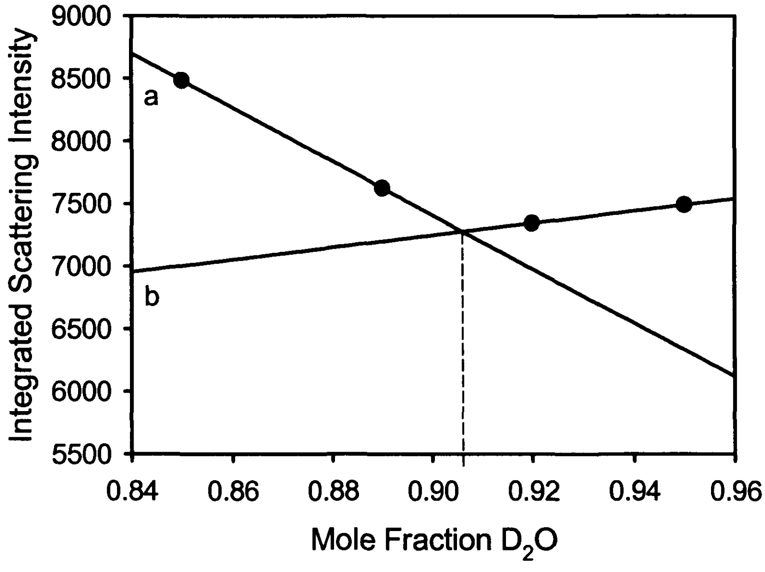

Figure 5.6: Plot of integrated scattering intensity (ISI) vs. mole fraction of D_2O to determine the contrast match–point for an emulsion of DCE–in–1.5 M sucrose D_2O/H_2O. The integrated scattering intensity was calculated using the equation: ISI=(count rate /sample transmission)^2 and the lines of regression correspond to the equations: (a) $y = 26760 - 21500x$ and (b) $y = 2864.5 + 4870x$. The match–point is determined to be 0.906 mole fraction D_2O in a solution of 1.5 M sucrose D_2O/H_2O.

From Figure **5.6**, the contrast match–point was determined to be 0.906 mole fraction of 1.5 M sucrose D_2O in a solution containing 1.5 M sucrose D_2O/H_2O, using the regression lines: $y = 26760 - 21500x$ and $y = 2864.5 + 4870x$. The scattering intensity does not pass through zero because, even though the DCE and aqueous phases were contrast matched, there would still be some scattering observed from the liquid–liquid interface. The value used in Figure **5.6** for the scattering intensity, has also not been normalised and corrected for the scattering due to pure water, the empty cuvette and direct beam. This would have been equal for all four mole fractions of D_2O and hence the absolute value for the scattering intensity was not needed.

For the normalisation of the observed raw data, the scattering and transmission was measured for the empty cuvette, the direct beam and for a cuvette of pure H_2O. The data for every emulsion mixture was then corrected for these and the normalised data is shown in Figures **5.7**, **5.8** and **5.9**.

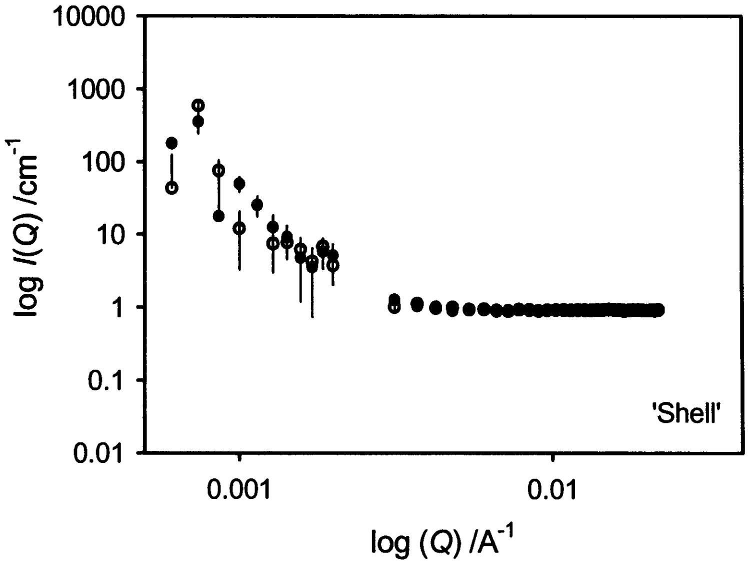

Figure 5.7: Graph showing log–log plot of the scattering intensity, $I(Q)$, vs. scattering vector, Q, for emulsion samples containing (●) 5 mM LiTPFB d–DCE–in–1.5 M sucrose 20 µM BSA 90.6:9.4 % D_2O:H_2O, and (○) d–DCE–in–1.5 M sucrose 20 µM BSA 90.6:9.4 % D_2O:H_2O. This is similar to the ideal 'shell' phase contrast.

In Figure **5.7** the large 'gap' in the data between $Q = 0.002$ and 0.003 Å^{-1}, is due to the merging of the data from the two detector distances. Whilst it can be seen that the statistics of the 8 m data are good, the errors for the 34 m are quite large, due to insufficient data collection time, and this resulted in the data not merging exactly.

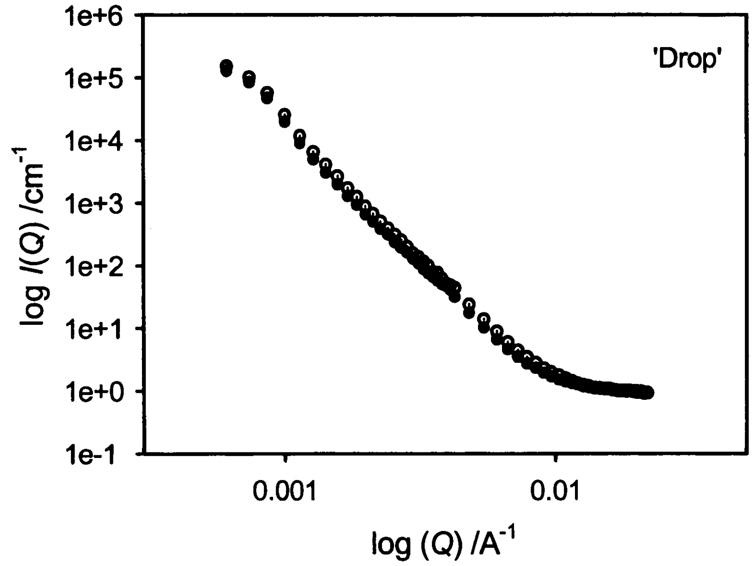

Figure 5.8: Graph showing log–log plot of the scattering intensity, *I*(*Q*), vs. scattering vector, *Q*, for emulsion samples containing (•) 5 mM LiTPFB h–DCE–in–1.5 M sucrose 20 μM BSA D_2O, and (○) h–DCE–in–1.5 M sucrose 20 μM BSA D_2O. This is similar to the ideal 'drop' phase contrast. (Error bars for *I*(*Q*) are included but are smaller than the size of the data point).

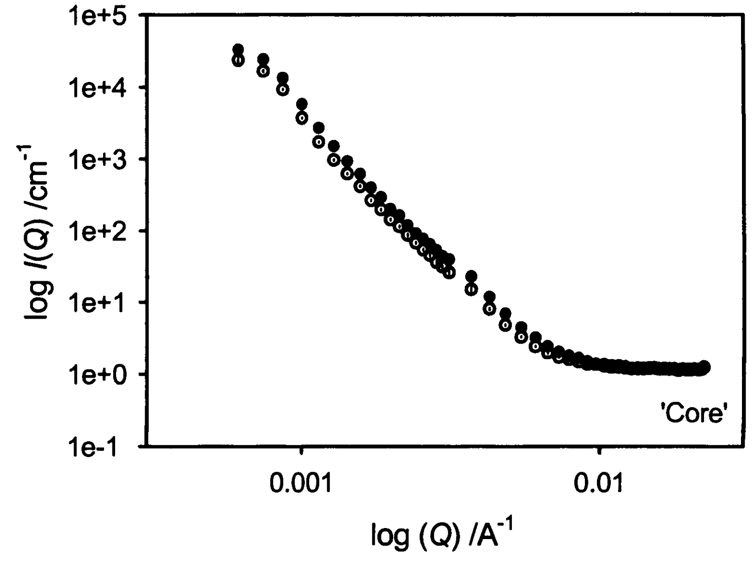

Figure 5.9: Graph showing log–log plot of the scattering intensity, *I*(*Q*), vs. scattering vector, *Q*, for emulsion samples containing (•) 5 mM LiTPFB d–DCE–in–1.5 M sucrose 20 μM BSA 50:50 % D_2O:H_2O, and (○) d–DCE–in–1.5 M sucrose 20 μM BSA 50:50 % D_2O:H_2O. This is similar to the ideal 'core' phase contrast. (Error bars for *I*(*Q*) are included but are smaller than the size of the data point).

From Figures **5.7**, **5.8** and **5.9**, a difference can be seen between the data for the emulsion with salts and those without. This suggests that the presence of stabilising salts affects the interfacial BSA and the data was then fitted using the FORTRAN program FISH to gain information regarding this protein layer.

5.4.1 D11 SANS Data Analysis using FISH

The SANS data has been analysed and model fitted using the FISH program written in FORTRAN [180]. The model used in the fitting is for a microemulsion and utilises the equations for a rigid core, with two shells, that has uniform scattering length densities in each phase (a copy of the model detailing the major parameters can be found in Appendix A). This uses a Marquardt Steepest Descent and Least Squares iteration to fit the normalised data for $\frac{\mathrm{d}\Sigma}{\mathrm{d}\Omega}(Q)$ to Equation **5.7**, using the approximated Hard Sphere Structure factor, $S_{\mathrm{HS}}(Q)$, and Equation **5.20** for the Form factor.

$$P(Q)=\left[\begin{array}{ll}\left(\rho_{BSA(DCE)}-\rho_{DCE}\right)F\left(Q,R_c\right)+\left(\rho_{BSA(aq)}-\rho_{BSA(DCE)}\right)F\left(Q,R_{s1}\right)\Big]^2 \\ +\left(\rho_{aq}-\rho_{BSA(aq)}\right)F\left(Q,R_d\right) \qquad\qquad \rho_{BSA(DCE)}\Big)F\left(Q,R_{s1}\right)\Big)\Big]^2\end{array}\right. \qquad \mathbf{5.20}$$

Where,

$$F(Q,R_x)=\left[\frac{3(\sin(QR_x)-QR_x\cos(QR_x))}{(QR_x)^3}\right] \qquad \mathbf{5.21}$$

and ρ_x and R_x are defined in Figure **5.10**.

Table **5.5** shows the scattering length densities, ρ_s, of the solution phases used in the microemulsion program, and Figures **5.11** and **5.12** show the resulting fitted data for the emulsions with and without salt respectively.

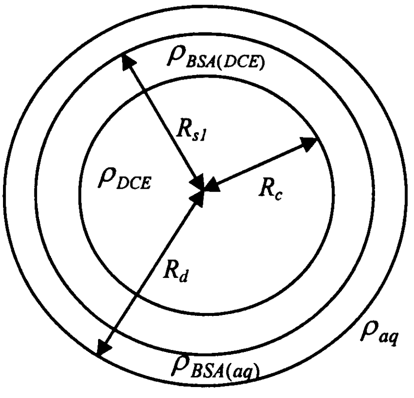

Figure 5.10: Schematic showing a DCE drop with SLD ρ_{DCE} and radius R_c. Surrounding the drop is a BSA layer composed of two shells, with SLD $\rho_{BSA(DCE)}$ and $\rho_{BSA(aq)}$ and thicknesses $(R_{s1}-R_c)$ and (R_d-R_{s1}) for the amphiphilic and hydrophilic BSA respectively.

Solution	ρ_s /x10^{-6} Å^{-2}	**Solution (+ sucrose)**	ρ_s /x10^{-6} Å^{-2}
h–DCE	1.314	**0.5:0.5 D_2O:H_2O**	2.487
d–DCE	4.322	**0.906:0.094 D_2O:H_2O**	4.337
BSA	2.5	**D_2O**	4.765

Table 5.5: Showing the scattering length densities, ρ_s, for the emulsion solution phases used in the microemulsion data fitting program.

The protein layer was assumed to be a uniform flat slab and, for fitting, the thickness of the BSA$_{DCE}$ shell was constrained at 1 Å, whilst the thickness of the BSA$_{Aq}$ shell was allowed to change. The BSA SLD for both shells was also constrained for the fitting, in a range of 2.0–3.0 x10^{-6} Å^{-2} to obtain an error for the interfacial layer with a change in SLD. Although the scattering length density of the BSA was determined in the literature to be in the order of 2.5 x10^{-6} Å^{-2}, exchange of labile hydrogens within the BSA would occur with the surrounding emulsion phases, and would result in a shift in this value [160].

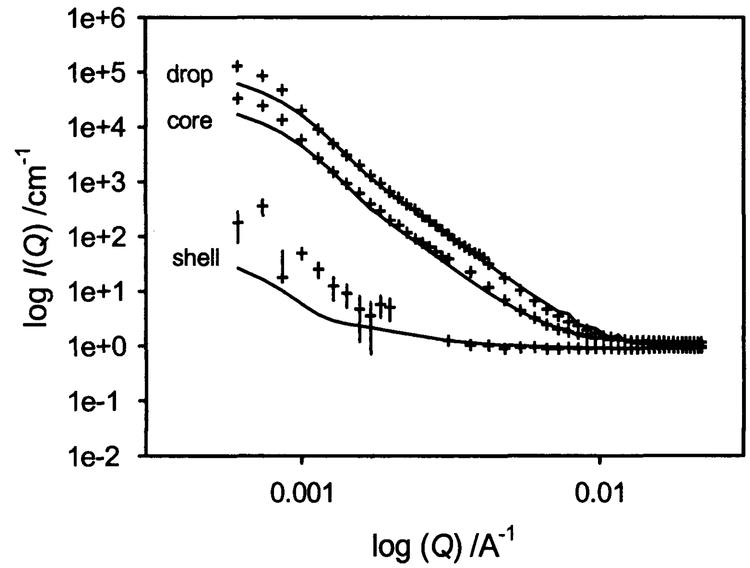

Figure 5.11: Graph showing the simultaneous fit of the 'drop', 'core' and 'shell' phase contrasts for the emulsion containing LiTPFB and BSA adsorbed at the liquid–liquid interface.

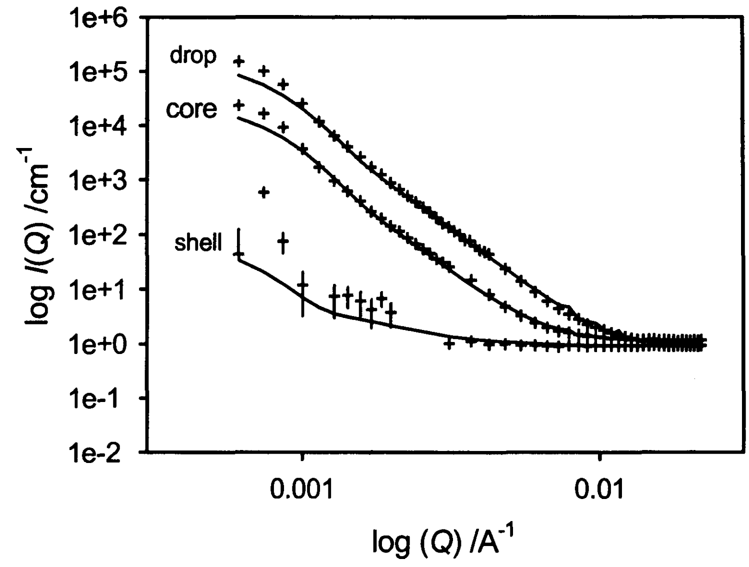

Figure 5.12: Graph showing the simultaneous fit of the 'drop', 'core' and 'shell' phase contrasts for the emulsion containing BSA adsorbed at the liquid–liquid interface without the inclusion of stabilising salts.

From Figures **5.11** and **5.12**, it can be seen that the D11 data, for the emulsion with and without salts, can be fitted simultaneously using the microemulsion FISH program. There are deviations of the fit from the data for both the emulsions at very low *Q* and this may be due to the high errors for the 'shell' contrast. The interfacial data obtained from the fit lines are shown in Table **5.6**, and these are compared with the expected values from the literature and emulsion characterisation experiments. The expected value for the interfacial BSA layer has been found to be in the order of 40 Å for the air–water interface [160&161] and corresponds to the formation of a 'sideways' adsorbed monolayer. This assumes the dimensions of the protein are 140x40x40 Å, with an oblate ellipsoid shape, as described in **1.3.1**, and has shown that the globular framework of the protein is retained after adsorption. When using an oil–water interface, there is likely to be some unfolding of the protein due to the hydrophobic nature of the DCE and therefore the interfacial BSA layer is likely to be thicker with a less defined shape.

From Table **5.6**, it can be seen that the fitted BSA layer thickness is similar to the expected value, as is the volume fraction of the BSA layer. The volume fraction for the total DCE drops is slightly less than expected and there is a large discrepancy in the fitted dimensions of the DCE drops, i.e. radius, volume and number density, when these are compared with those determined experimentally using optical microscopy. When the expected values are used initially in the FISH program, the data fails to fit and eventually returns to the obtained values in Table **5.6**. By comparing the obtained volume fraction of the DCE drops with the data in Table **5.1** in **5.2**, it can be seen that this volume fraction seems to explain the 'missing' 0.1 wt % of DCE not present in the emulsions containing BSA. It would therefore suggest, due to the small drop radius (220 nm) and very large number density (3 x10^{10} drops cm^{-3}) that a secondary microemulsion is also present in the emulsions prepared containing BSA. This would be too small to be observed under the optical microscope and would not be visible due to the small size when compared to the wavelength of visible light.

	Fitted		Expected
	No Salt	Salt	
BSA layer thickness /Å	47.9 ±16	40.3 ±15	40
BSA SLD /x10^{-6} Å^{-2}	–	–	2.5 ±0.4
% Water in BSA layer	20	0	–
Volume Fraction BSA layer per drop /%v	0.056	0.048	0.05
Total Volume Fraction DCE /%v	0.15 ±0.002	0.11 ±0.002	0.33
Emulsion Polydispersity	0.31 ±0.005	0.30 ±0.005	–
Volume DCE per drop /x10^{10} Å^{3}	5.93	5.50	1650
Volume BSA layer per drop /x10^{9} Å^{3}	3.30	2.65	786
Surface Area Outer BSA layer per drop /x10^{7} Å^{2}	7.02	6.68	323
Total Surface Area DCE+BSA Drops /x10^{18} Å^{2}	230.3	171.0	0.7
DCE drop radius /x10^{3} Å	2.21 ±0.03	2.17 ±0.03	16
Number Density DCE drops /x10^{12} drops cm^{-3}	3.28	2.56	0.0002

Table 5.6: Showing the interfacial data obtained from the simultaneous fit lines in Figures **5.12** and **5.13** compared with the expected values from the literature and emulsion characterisation experiments.

As described in **1.3.1**, BSA is a commonly used emulsifying agent due to its highly surface–active nature and rapid adsorption at the oil–water interface formed upon emulsification [173]. This emulsification is not initiated by the BSA as such, but instead the emulsion is formed by rapid mechanical homogenisation of the oil and water, with the resulting emulsion being stabilised by the protein adsorbed at the interface [168]. This results in a thin dense layer of interacting polymer molecules, with the main thermodynamic force driving the adsorption, being the removal of non–polar side–chains from the aqueous layer by displacing the water molecules at the interface [172]. The partial unfolding of the native globular structure of the protein at the interface also drives the adsorption. A possible mechanism for the formation of the secondary BSA microemulsion would be similar to that described in **3.2** but with the BSA adsorbing and forming a monolayer around the DCE molecular clusters before the emulsion drops are created. Because there would be many more molecular clusters formed initially, than there are drops seen with optical microscopy, this would explain the large number density. These BSA–covered clusters would then be stabilised by the protein, hence forming a microemulsion, and would therefore be unlikely to continue to coalesce to form the expected drop volume. From the experiments in **5.2**, drops with 3 μm diameter that appeared to be stabilised with BSA, were seen, however, and so a proportion of the microemulsion must continue to grow via molecular diffusion to form the expected emulsion. This would occur when an incomplete monolayer forms around some drops, hence allowing the molecules to penetrate the BSA layer. An approximate value of 200 $\times 10^{18}$ Å^2 is obtained for the total surface area of the secondary microemulsion, with or without salts, and, when this is compared to the surface area of the 'expected' emulsion, 0.7 $\times 10^{18}$ Å^2, it can be seen that the concentration of the expected emulsion is in fact negligible when compared to that of the microemulsion. This can also be seen by looking at the ratio of the total surface area of 'large' drops to 'small', a value of 0.003.

Because the total surface area of the microemulsion is much greater than expected, the concentration of BSA used in the experiments may have been insufficient to form a monolayer around every drop. Using the revised total emulsion surface area of 200 $\times 10^{18}$ Å^2 in Equations **5.17** and **5.18**, the concentration of BSA needed to form an interfacial monolayer is calculated to be 3 mM, a value much higher than the 20 μM used in the experiments. This would suggest that a complete monolayer is not able to form around every drop, and therefore explains why the expected emulsion drops were also able to grow. On hydrophobic surfaces, BSA has been shown to adsorb as 'islands' of protein and not a complete layer [160] and this could also explain why the layer thickness fitted using FISH is similar to the expected value.

Even though there are drops present of the expected μm diameter, it is believed that they are not observed in the data fitting because, even at the lowest *Q*–value experimentally possible, the emulsion drops are still too large to be observed in their entirety. This can be confirmed by calculating the approximate observable system dimensions investigated, using Equation **5.3** and the D11 *Q*–range of 0.0006–0.022 $Å^{-1}$. These were determined to be 285–10500 Å and thus it can be seen that the average emulsion drop diameter of 32000 Å, measured using optical microscopy, is three times greater than the maximum approximate drop dimensions measurable using D11. The neutrons are therefore only seeing the entire microemulsion drops, and a portion of the 'expected' emulsion. This is confirmed because the ratio of the total surface areas of 'large' expected emulsion drops to 'small' microemulsion drops is very low; 0.003. It can also be seen that there is some deviation from the fitted lines at low *Q*, log *Q*, < 0.001 $Å^{-1}$, for all three contrasts, and this is because there would be some contribution to the scattering profile from the 'large' drops at very low *Q*, and therefore the scattering information would overlap. To see the entire 'expected' emulsion drops, the minimum *Q* would need to be in the order of 0.00015 $Å^{-1}$ but then there may be more scattering overlap between the two emulsion systems.

From Table **5.6** it can also be seen that the emulsion containing salt appears to have a thinner and drier layer of BSA when compared with an emulsion without LiTPFB. This may be due to the salts increasing the amount of protein adsorbed at the interface and hence creating a thicker layer, however, due to there being an insufficient concentration to form a monolayer it is likely that the solvated water adds to the thickness of the interfacial protein.

As described, the data was fitted assuming a uniform slab profile for the protein but, due to partial unfolding of the BSA, the profile is more likely to be a non–uniform diffuse layer. A schematic diagram showing the uniform slab and probable diffuse layer is shown in Figure **5.13**.

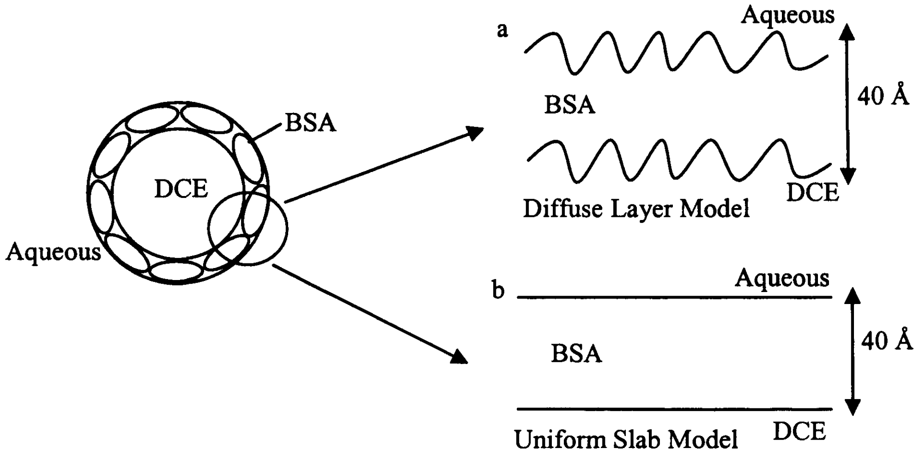

Figure 5.13: Schematic diagram showing (b) the Uniform Slab Model used in the data fitting and (a) a more realistic Diffuse Layer Model.

From Figure **5.13**, it can be seen that the microemulsion FISH model was not perfect and that the nature of the protein adsorption could not be determined by using a uniform slab. A model for a diffuse protein layer would therefore be more accurate.

5.5 ILL D22 Results

For the analysis using D22 at the ILL, four emulsion systems were investigated; DCE–in–water with and without LiTPFB and/or BSA. Not only was the interfacial adsorption of BSA investigated, but also the 'clean' liquid–liquid interface and the effects on this of stabilising salts. The data was collected at two different detector distances, 17.6 and 3.0 m, with a fixed–wavelength of 15 Å. The two sets of data were then merged together to give one continuous set of data. The emulsions were created as in **2.4**, with the emulsion cooled to 30 °C for 30 mins before analysis in the neutron beam at 15 °C. This discrepancy in cooling temperature was due to an incorrectly calibrated water–bath that had been set at 15 °C but in fact was 30 °C. This led to a secondary emulsion forming when the cuvette was put in the neutron beam at 15 °C, as shown in the schematic diagram in Figure **5.14**.

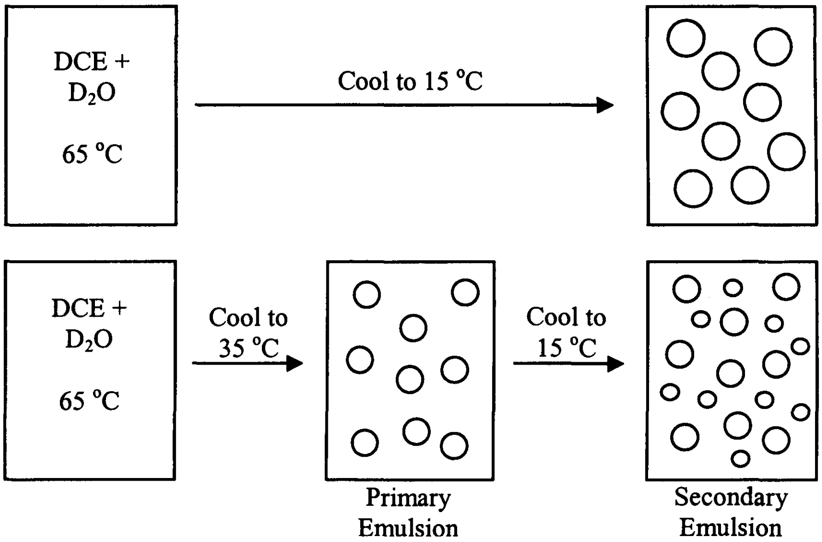

Figure 5.14: Schematic diagram showing the formation of a primary and secondary emulsion of DCE–in–D_2O created by cooling the emulsion from 65 °C to 35 °C and then subsequently rapidly cooling to 15 °C.

The secondary emulsion was formed from the aqueous dissolved DCE at 35 °C and from Table **3.1** in **3.2** it can be seen that the maximum weight percent of DCE present as the primary emulsion drops would be 0.31 wt % whereas that for the secondary emulsion would be 0.09 wt %. From the data for the weight percent of DCE drops in Table **5.1**, where the maximum weight percent is 0.40 wt %, it can be seen that only a percentage of this maximum condenses as DCE drops and therefore this value for the primary and secondary emulsions needs to be adjusted. If the number density of this secondary emulsion was assumed to be the same as for one heated to 65 °C and then cooled to 15 °C, the average drop volume and diameter for both the primary and secondary emulsions can be calculated, and are shown in Table **5.7**, for emulsions containing BSA and sucrose, BSA with sucrose and LiTPFB, sucrose only, and sucrose with LiTPFB.

As it can be seen from Table **5.7**, the drop volume calculated for the secondary emulsion is approximately 75 % smaller than that measured for the emulsion formed by heating to 65 °C and then cooling to 15 °C and the corresponding drop diameter is 30 % smaller. This can be seen for the emulsion regardless of the presence of BSA or LiTPFB, but is still only an approximation because the nucleation characteristics of the primary and secondary emulsions are assumed to be the same as that of the system formed by cooling from 65 °C to 15 °C directly. The possible formation of a separate BSA microemulsion, as seen in **5.4.1** for the D11 experiments, has also not been included in these calculations. This would create a tertiary emulsion and would cause further confusion to the analysis of the data.

Emulsion System (+ sucrose)	**Heat – Cool Temp /°C**	**Drop Volume /μm^3 (diameter)**	**Number Density /x10^6 drops cm^{-3}**	**Weight Percent Emulsion Drops (Literature)**
DCE–in–BSA D_2O	65 – 15	15 ±2 (3.1 ±0.1 μm)	160 ±10	0.25 ±0.03 (0.40)
	65 – 35	12 ±0.6 (2.8 ±0.1 μm)		0.19 (0.31)
	35 – 15	3.7 ±0.2 (1.9 ±0.1 μm)		0.06 (0.09)
LiTPFB DCE–in–BSA D_2O	65 – 15	18 ±2 (3.3 ±0.1 μm)	230 ±16	0.42 ±0.05 (0.40)
	65 – 35	14 ±0.8 (3.0 ±0.1 μm)		0.33 (0.31)
	35 – 15	4.3 ±0.2 (2.0 ±0.1 μm)		0.10 (0.09)
DCE–in–D_2O	65 – 15	25 ±5 (3.6 ±0.2 μm)	140 ±12	0.35 ±0.06 (0.40)
	65 – 35	19 ±0.8 (3.3 ±0.1 μm)		0.27 (0.31)
	35 – 15	5.6 ±0.4 (2.2 ±0.1 μm)		0.08 (0.09)
LiTPFB DCE–in–D_2O	65 – 15	25 ±6 (3.6 ±0.2 μm)	200 ±24	0.51 ±0.14 (0.40)
	65 – 35	20 ±2 (3.3 ±0.1 μm)		0.40 (0.31)
	35 – 15	5.9 ±0.6 (2.2 ±0.1 μm)		0.12 (0.09)

Table 5.7: Showing the formation temperatures and the determined drop volume, diameter and DCE weight percent for primary and secondary emulsions containing DCE–in–D_2O with and without BSA and/or LiTPFB.

5.5.1 SANS Data for the 'BSA' Interface

The emulsions used for the investigation of protein adsorption at the liquid–liquid interface were composed of d–DCE–in–1.5 M sucrose 5 μM BSA D_2O ('shell'), h–DCE–in–1.5 M sucrose 5 μM BSA D_2O ('drop'), and d–DCE–in–1.5 M sucrose 5 μM BSA 0.70 mole fraction D_2O and 0.30 mole fraction H_2O ('match'). These mole fractions calculated for the contrast match did not include the contribution due to sucrose and hence were not an exact match. The experiment was then repeated with 5 mM LiTPFB in the DCE phase to study the effect of salts on the BSA layer. The concentration of BSA was lower than that used at the ILL on D11 (20 μM) because the emulsion was not fully characterised and only an estimate had been made for the drop volume and number density. The emulsion phase contrasts investigated were also inaccurate due to a lack of experience using the technique and the contrasts are shown as SLD profiles in Figure **5.15**.

As it can be seen from this figure, only the 'drop' phase contrast used in the D22 SANS experiments on an emulsion containing BSA, was an 'ideal' system and no 'core' contrast was used. Instead there were two phase contrasts close to match–point and these were termed 'match' and 'shell'. These however were not an exact contrast match and so it was unlikely that interfacial data would be determined from the results. The SANS data obtained for both emulsions with and without salts is shown in Figures **5.16**, **5.17** and **5.18** for the phase contrasts 'drop', 'match' and 'shell' respectively. The data normalisation was the same as for D11, with the neutron scattering and transmission being measured for an empty cell, the direct beam and a sample of pure H_2O.

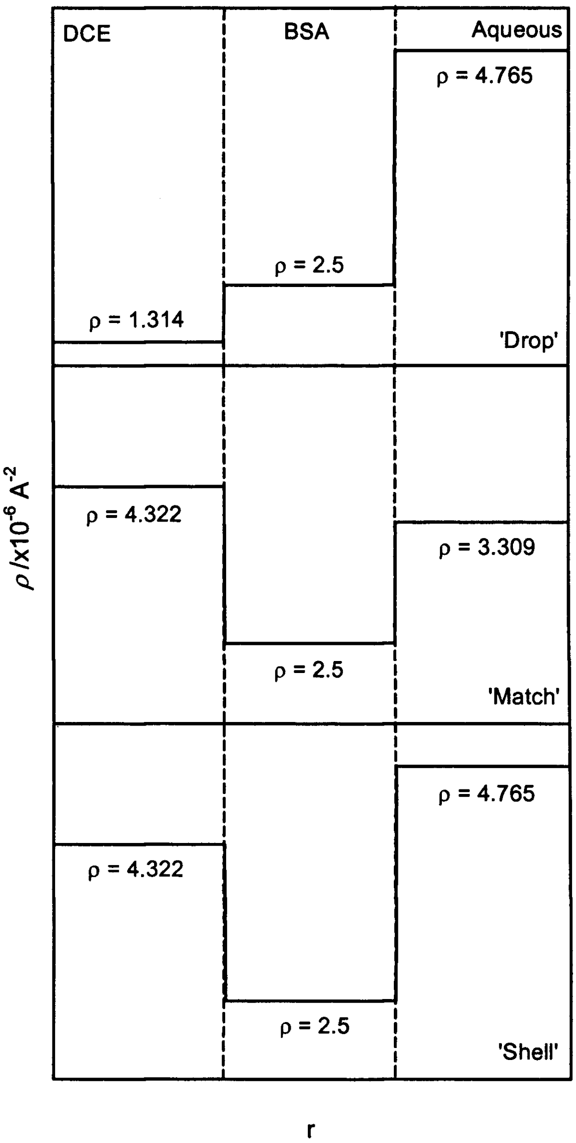

Figure 5.15: Diagram showing the SLD profile vs. distance r for the three phase contrasts: 'drop', 'match' and 'shell' used in the ILL D22 SANS experiments for an emulsion with a layer of BSA adsorbed at the liquid–liquid interface.

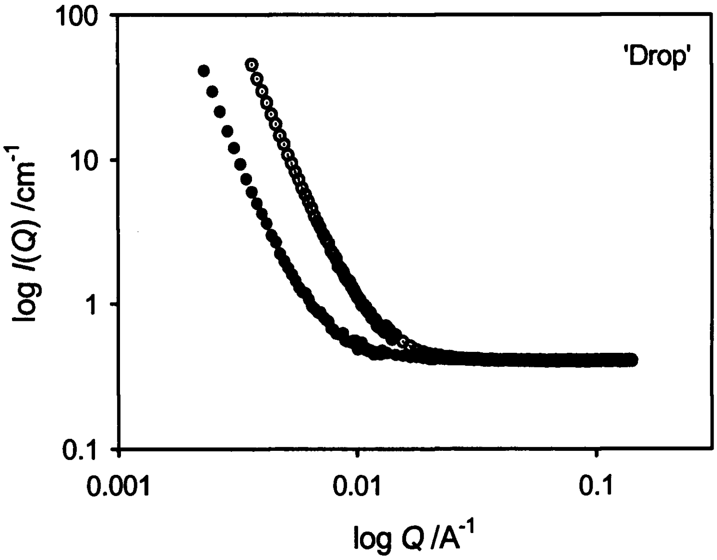

Figure 5.16: Graph showing log–log plot of the scattering intensity, *I*(*Q*), vs. scattering vector, *Q*, for emulsion samples containing (●) 5 mM LiTPFB h–DCE–in–1.5 M sucrose 5 μM BSA D_2O, and (○) h–DCE–in–1.5 M sucrose 5 μM BSA D_2O. This is similar to the ideal 'drop' phase contrast. (Error bars for *I*(*Q*) are included but are smaller than the size of the data point).

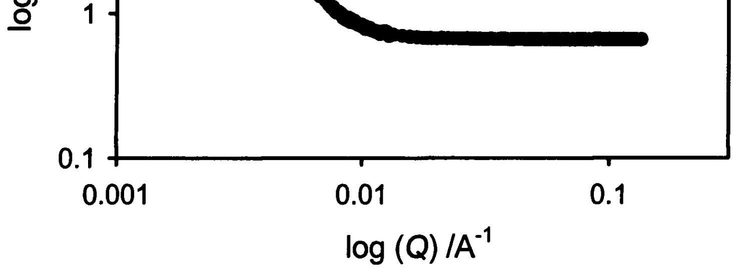

Figure 5.17: Graph showing log–log plot of the scattering intensity, *I*(*Q*), vs. scattering vector, *Q*, for emulsion samples containing (●) 5 mM LiTPFB d–DCE–in–1.5 M sucrose 5 μM BSA D_2O/H_2O, and (○) d–DCE–in–1.5 M sucrose 5 μM BSA D_2O/H_2O, termed the 'match' phase contrast. (Error bars for *I*(*Q*) are included but are smaller than the size of the data point).

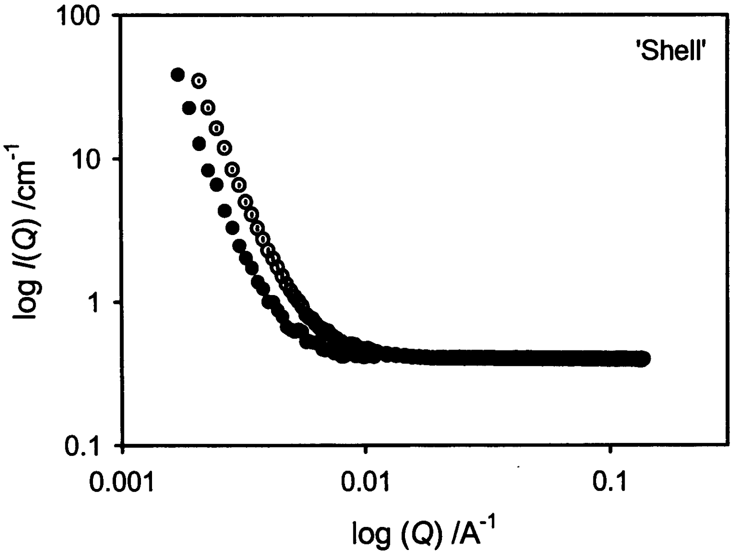

Figure 5.18: Graph showing log–log plot of the scattering intensity, *I*(*Q*), vs. scattering vector, *Q*, for emulsion samples containing (●) 5 mM LiTPFB d–DCE–in–1.5 M sucrose 5 μM BSA D_2O, and (○) d–DCE–in–1.5 M sucrose 5 μM BSA D_2O, termed the 'shell' phase contrast. (Error bars for *I*(*Q*) are included but are smaller than the size of the data point).

From Figures **5.16**, **5.17** and **5.18** it can be seen that there is a difference between the systems containing LiTPFB and those without. This confirms the results from D11 that the salts affect the thickness of the liquid–liquid interface but analysis using FISH proved inconclusive due to the incorrect phase contrasts and an inhomogeneous emulsion drop size.

5.5.2 'Clean' Interface

Emulsions were then created containing d–DCE–in–1.5 M sucrose D_2O, h–DCE–in–1.5 M sucrose D_2O, and d–DCE–in–1.5 M sucrose H_2O to investigate the thickness of the 'clean' liquid–liquid interface. These were also repeated with 5 mM LiTPFB in the DCE phase to study the effect of the salts on the interface, and the solution phase contrasts used are shown in Figure **5.19**.

As it can be seen from this figure, both the 'drop' and 'core' contrasts were similar to the ideal case. The 'shell' phase contrast was not an exact match but it was hoped that this might still give some interfacial information when combined with the 'drop' and 'core' data. Due to the presence of the two emulsion size distributions, however, data fitting was not possible. The normalised SANS data, corrected for the sample transmission, empty cell, direct beam and pure H_2O, obtained is shown in Figures **5.20**, **5.21** and **5.22** for the emulsions with and without stabilising salts. These show that there was a small difference in the scans for the emulsions with and without salts; however, this was not as large as the difference seen for the emulsions containing BSA in **5.4.1** and **5.5.1**, as expected.

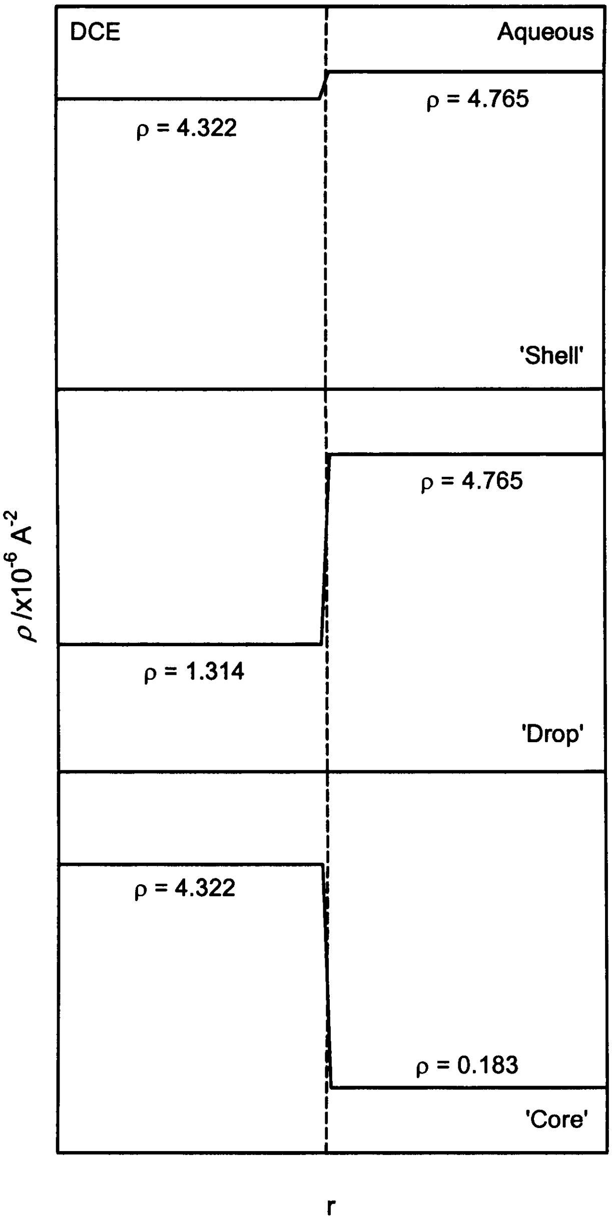

Figure 5.19: Diagram showing the SLD profile vs. distance r for the three phase contrasts: 'shell', 'drop' and 'core' used in the ILL D22 SANS experiments for an emulsion with a 'clean' liquid–liquid interface.

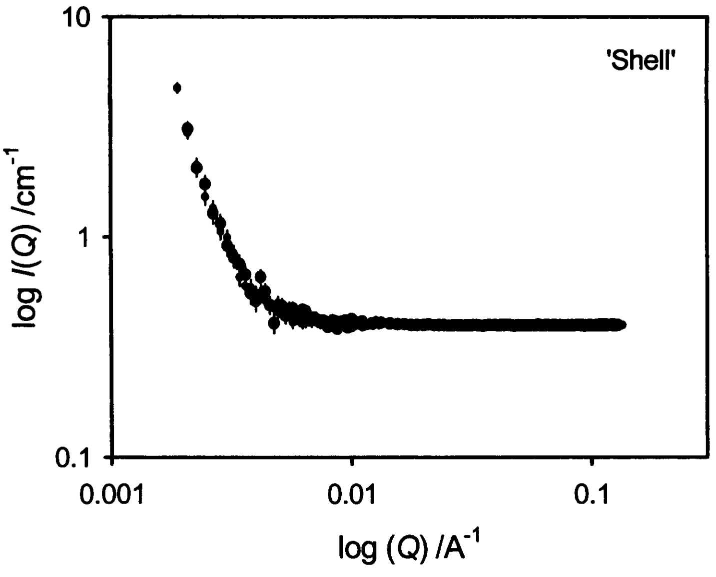

Figure 5.20: Graph showing log–log plot of the scattering intensity, *I*(*Q*), vs. scattering vector, *Q*, for emulsion samples containing (•) 5 mM LiTPFB d–DCE–in–1.5 M sucrose D_2O, and (○) d–DCE–in–1.5 M sucrose D_2O. This is similar to the ideal 'shell' phase contrast.

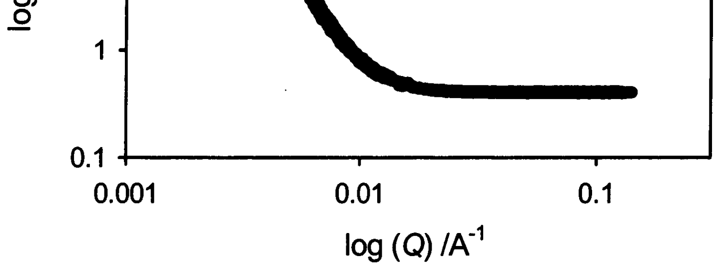

Figure 5.21: Graph showing log–log plot of the scattering intensity, *I*(*Q*), vs. scattering vector, *Q*, for emulsion samples containing (•) 5 mM LiTPFB h–DCE–in–1.5 M sucrose D_2O, and (○) h–DCE–in–1.5 M sucrose D_2O. This is similar to the ideal 'drop' phase contrast. (Error bars for *I*(*Q*) are included but are smaller than the size of the data point).

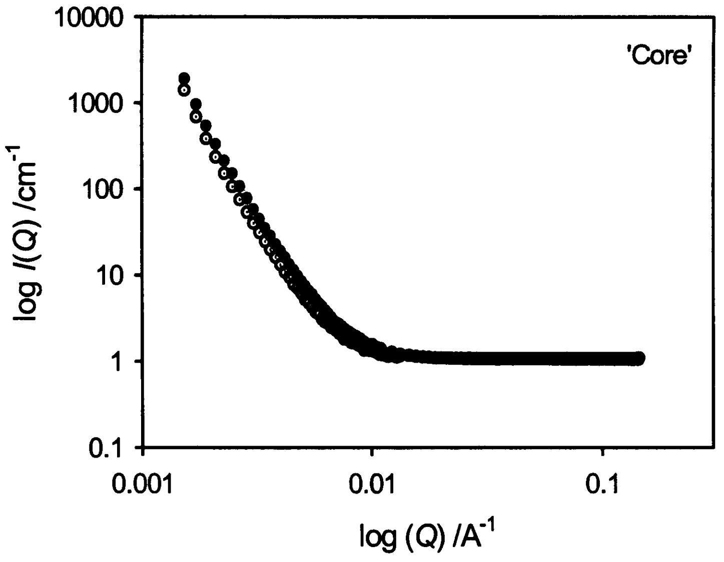

Figure 5.22: Graph showing log–log plot of the scattering intensity, *I*(*Q*), vs. scattering vector, *Q*, for emulsion samples containing (•) 5 mM LiTPFB d–DCE–in–1.5 M sucrose H_2O, and (○) d–DCE–in–1.5 M sucrose H_2O. This is similar to the ideal 'core' phase contrast. (Error bars for *I*(*Q*) are included but are smaller than the size of the data point).

5.6 ISIS LOQ Results

LOQ was a fixed–geometry instrument and hence only one detector distance, 4 m, was needed and instead neutrons with a range of wavelengths, 2.2–10 Å, were used. Emulsions were created that contained 10 μM TEATPB d–DCE–in–1.0 M sucrose 0.1 M TEACl 5 μM BSA D_2O, 10 μM TEATPB h–DCE–in–1.0 M sucrose 0.1 M TEACl 5 μM BSA D_2O, and 10 μM TEATPB d–DCE–in–1.0 M sucrose 0.1 M TEACl 5 μM BSA 0.70 mole fraction D_2O 0.30 mole fraction H_2O. The concentration of BSA was again lower than that used for D11 at the ILL, as explained for the experiments using D22. The same emulsion phase contrasts were also investigated as for D22 with the exception that 1.0 M sucrose was used instead of 1.5 M. This was to reduce the amount of incoherent scattering from hydrogen but whilst also giving some stabilisation to the emulsion. The contrasts are shown as SLD profiles in Figure **5.23.**

The emulsions were created as in **2.4** by heating to 65 °C and cooling to 15 °C for 30 mins, and then the sample was put into the cuvette and placed in the neutron beam for analysis at 15 °C. The SANS data obtained is shown in Figures **5.24**, **5.25** and **5.26** for the phase contrasts ‘drop’, ‘match’ and ‘shell’ respectively.

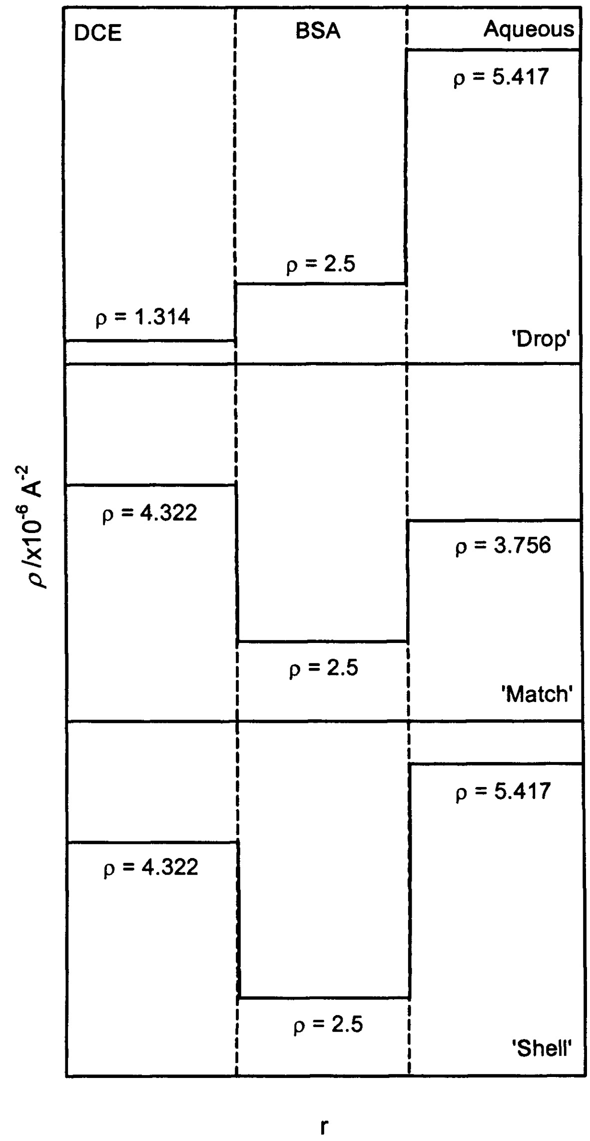

Figure 5.23: Diagram showing the SLD profile vs. distance r for the three phase contrasts: ‘drop’, ‘match’ and ‘shell’ used in the ISIS LOQ SANS experiments for an emulsion with a layer of BSA adsorbed at the liquid–liquid interface.

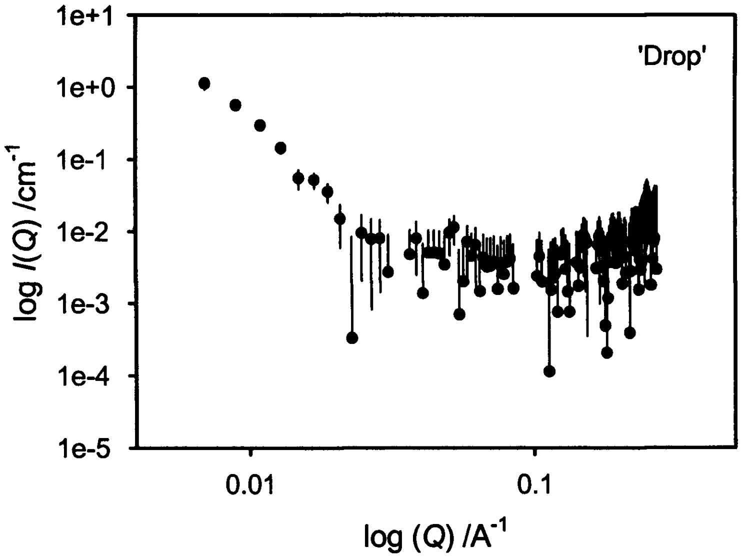

Figure 5.24: Graph showing log–log plot of the scattering intensity, $I(Q)$, vs. scattering vector, Q, for an emulsion sample containing 10 µM TEATPB h–DCE–in–1.0 M sucrose 0.1 M TEACl 5 µM BSA D_2O, similar to the ideal 'drop' phase contrast.

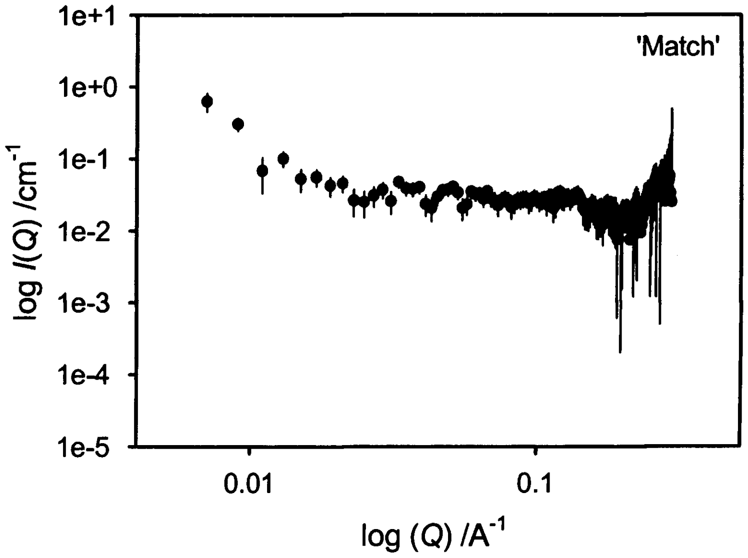

Figure 5.25: Graph showing log–log plot of the scattering intensity, $I(Q)$, vs. scattering vector, Q, for an emulsion sample containing 10 µM TEATPB d–DCE–in–1.0 M sucrose 0.1 M TEACl 5 µM BSA D_2O/H_2O, termed the 'match' phase contrast.

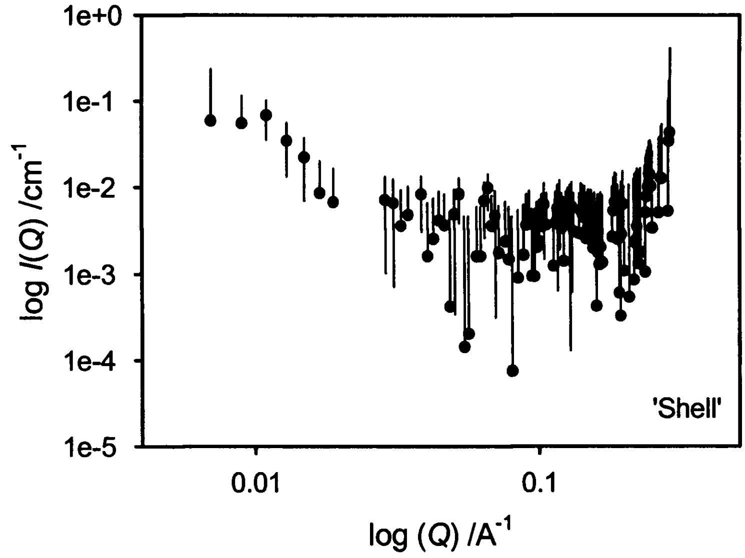

Figure 5.26: Graph showing log–log plot of the scattering intensity, *I(Q)*, vs. scattering vector, *Q*, for an emulsion sample containing 10 μM TEATPB d–DCE–in–1.0 M sucrose 0.1 M TEACl 5 μM BSA D_2O, termed the 'shell' phase contrast.

From Figures **5.24**, **5.25** and **5.26** it can be seen that, even though scattering was seen for the emulsions containing BSA, the error bars are very large when compared with the data from the ILL and hence the data was unreliable. The timescales of these experiments was on average 8 hours data collection time yet the statistics of the data were still relatively low when compared to the data collected after 30 mins at the ILL. The collection time could not be run longer, however, due to the increase in emulsion destabilisation which was seen to occur after 2 hours, and this may also have contributed to the large errors.

5.7 Conclusions

The emulsion containing BSA was characterised using optical microscopy with and without the potential–determining salt LiTPFB in **5.2**, and the addition of protein was shown to give greater stability to the emulsion, irrespective of the presence of salt. BSA was seen, however, to slightly reduce the observed weight percent of the oil drops but this was not seen to significantly affect the sensitivity of the emulsion drop volume to temperature. The pH of the aqueous emulsion phases used in subsequent SANS experiments was also measured and it was found that for emulsion containing salts, the pH was 8.1, and without salts this decreased to pH 7.3. These values suggested that the protein was present at the interface in a structure similar to its Normal and Basic forms.

From the SANS experiments, only D11 at the ILL gave data that was analysable, and data from D22 and LOQ could only be used qualitatively for comparison. From using D11 at the ILL, in **5.4**, it was seen that the inclusion of BSA acted to stabilise a secondary microemulsion of DCE in water and this corresponded to the missing 0.1 wt % from the characterisation experiments in **5.2**. It was also seen that the potential–determining salts had an effect on an interfacial adsorbed layer of BSA, and both systems with and without salts, were seen to be comparable in thickness to that determined in the literature; 40.3 Å for the emulsion containing salts compared with 40 Å, while the layer for the emulsion without salts, was slightly larger at 47.9 Å. This was believed to be due to there being solvated water in the layer; 20 % water and 80 % protein, whereas when salts were used, this layer contained no water. The salts may also have increased the amount of adsorbed protein, hence creating a complete monolayer, whereas for the emulsion without salts, the protein may have been adsorbed as islands with a more defined globular structure.

In **5.5.2**, the 'clean' liquid–liquid interface, without any adsorbed protein or surfactant, was investigated, with and without stabilising salts, using D22 at the ILL. A difference was seen in the scans with and without LiTPFB, although the shift was not as large as that for the adsorbed protein layer, suggesting that the salts affected the roughness of the interface. It was, however, not possible to determine the thickness of this interface due to the formation of a secondary emulsion and incorrect phase contrasts, therefore preventing analysis using FISH.

The emulsion containing BSA and the two–salt stabilisation system with TEA^+, was also studied in **5.6**, using LOQ at ISIS but the quality of the data was much lower than that from the ILL. The difference in the resolution of the data from ISIS and the ILL was due to the difference in the instruments at the two facilities and the method used to produce and detect the neutrons. As described in **2.7**, ISIS used a spallation source and LOQ was a fixed–geometry instrument, whereas the ILL was a reactor source with both D22 and D11 being fixed–wavelength instruments. It was found that the ILL instruments were better at investigating the emulsion, seen by the shorter experimental timescales, due to the better Q–resolution. This eliminated any possible emulsion destabilisation affecting the results and also allowed for more systems to be studied in a shorter length of time. This better Q–resolution was caused by the higher flux of neutrons from the ILL reactor when compared with the pulsed neutron beam from the ISIS spallation source. Another advantage to using the ILL instead of ISIS was the lower Q–range that could be studied with D11. This was due to the fixed–geometry instrument and longer detection distance, rather than the fixed–wavelength instrument at ISIS, and allowed for larger emulsion drops to be studied with a higher accuracy. It was seen however, in **5.4.1** that the Q–range accessible with D11 was still not low enough for the emulsion drops to be seen in their entirety, and the ideal minimum *Q* was determined to be in the order of 0.00015 $Å^{-1}$ for an emulsion formed at 15 °C. Alternatively, the emulsion drops could be formed at a higher temperature, hence with a smaller drop volume and radius.

Overall, SANS using D11 at the ILL was found to be the most effective at investigating protein adsorption at the liquid–liquid interface and it was found that adsorbed BSA formed layers 40 and 48 Å thick with and without LiTPFB respectively. It was also found that the presence of salts affected the hydration of the BSA layer; with there being 20 % water and 80 % protein in the layer without LiTPFB, and no water in the emulsion containing salts.

Chapter 6: Characterisation and Stabilisation of a Water–in–Oil Emulsion and its Comparison with an Oil–in–Water System

6.1 Introduction

A water–in–oil emulsion, consisting of D_2O–in–DCE, has been created using a condensation technique and is stabilised by partitioning the potential–determining salt lithium tetrakis(pentafluorophenyl)borate (LiTPFB) across the liquid–liquid interface. This sets–up an interfacial Galvani–type potential, that reduces the rate of coalescence, and the stability has been studied using turbidity and optical microscopy measurements. The emulsion has also been characterised and compared with the oil–in–water system described in Chapters **3** and **4**.

Presented in this chapter, are also some initial results of the electrodeposition of palladium, using the DCE–in–D_2O and D_2O–in–DCE emulsions.

6.2 Emulsion Creation and Characterisation

Using the condensation method optimised in **3.2**, emulsions were investigated that contained water–in–oil. The same principles of solubility of oil in water as for water in oil were used to create this emulsion, and Figure **6.1** shows the literature solubility of water in DCE over a range of temperatures from 20–70 °C [184]. The literature data has been fitted to a regression line using the equation: y=0.8+0.06exp$^{0.03x}$.

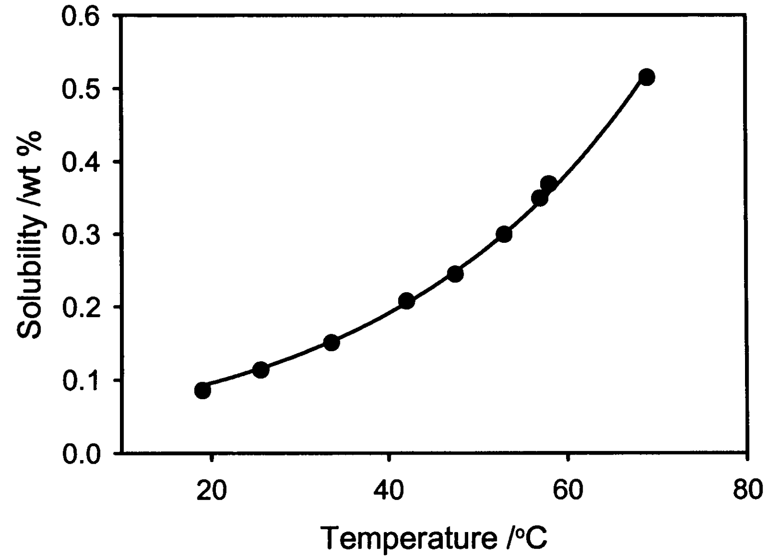

Figure 6.1: Solubility plot of H_2O in DCE determined between 20–70 °C [184]. The solid line corresponds to the regression fit using the equation: y=0.8+0.06exp$^{0.03x}$.

Figure **6.1** shows that by heating the two liquids, the solubility of water in DCE increases with temperature and it can be determined that by heating a mixture of DCE and water to 65 °C, 0.46 wt % of water dissolves in the DCE and after this is cooled to 25 °C, 0.11 wt % remains dissolved. This leaves 0.35 wt % of H_2O that will condense from the DCE to form emulsion drops, compared with 0.4 wt % determined for a DCE–in–H_2O mixture in **3.2**.

Table **6.1**, shows the solubility weight percent of H_2O dissolved in DCE at different temperatures, and the calculated weight percent of water present as emulsion drops when the emulsion is heated to 65 °C and then cooled to temperatures in the range 55–5 °C. Also included is the calculated weight percent data for DCE in water from **3.2**, Table **3.1**.

Temperature / °C	Solubility /wt %	wt % H_2O drops	wt % DCE drops
65	0.46	–	–
55	0.32	0.14	0.14
45	0.23	0.23	0.24
35	0.16	0.30	0.31
25	0.11	0.35	0.37
15	0.08	0.38	0.40
5	0.06	0.40	0.43

Table 6.1: Showing the solubility weight percent of water in DCE at different temperatures [184] and the calculated weight percent of water present as drops when the emulsion is heated to 65 °C and cooled to temperatures in the range 55–5 °C. Also included is the calculated wt % of DCE present as drops when the emulsion is heated and cooled to the same temperature range.

From Table **6.1**, it can be seen that although the solubility of water in DCE is less than that of DCE in water (Table **3.1** in **3.2**) the calculated solubility weight percent condensed as emulsion drops is comparable between the two emulsion systems.

The water–in–oil emulsion was characterised using optical microscopy to measure the drop volume and number density as described in **2.6**, and for an emulsion composed of D_2O–in–DCE heated to 65 °C and cooled to 15 °C, the drop volume was calculated to be 22 ±3 μm^3 and the number density of drops per unit volume was 150 ±15 $\times 10^6$ drops cm^{-3}. In Table **6.2** these values, and the calculated weight percent, are compared with those determined for a DCE–in–1.5 M sucrose D_2O emulsion in **3.3.1**.

Emulsion System	Drop Volume /μm^3	Number Density /x10^6 drops cm^{-3}	Weight Percent Emulsion Drops
D_2O–in–DCE	22 ±3 (3.5 ±0.1 μm)	150 ±15	0.33 ±0.05
DCE–in–D_2O (+ sucrose)	25 ±5 (3.6 ±0.2 μm)	140 ±12	0.35 ±0.06

Table 6.2: Comparing the measured drop volume, number density and calculated weight percent of emulsion drops for a D_2O–in–DCE system with values from **3.3.1** for a DCE–in–1.5 M sucrose D_2O emulsion.

From Table **6.2**, it can be seen that there is no significant difference in the drop volume and number density for emulsions containing water–in–oil or oil–in–water formed using a condensation technique.

Attempts were also made to measure the drop volume every hour, as in **3.3.1**, to see qualitatively how the emulsion destabilised over time. Difficulties were encountered, however, due to the high vapour pressure of the DCE and these were similar to the problems experienced in **3.3.1**. This was because the DCE would evaporate into the head–space of the flask and every time a measurement was taken, this would be released. Because the continuous phase of the emulsion was DCE, this caused the emulsion to decrease in total volume every time the flask was opened and caused rapid destabilisation of the emulsion. There were also problems encountered when the measurements were taken under the microscope, due to the DCE evaporation from the glass slide.

6.3 Emulsion Stabilisation

To investigate the stability of an emulsion composed of water–in–DCE, compared with using DCE–in–water, emulsions were created using 10 cm^3 DCE and 1 cm^3 of H_2O or D_2O. These were heated to 65 °C and cooled to 15 °C, as described in **2.4**, and samples were taken for analysis using turbidity measurements maintained at 15 °C. The spectra obtained were then compared with results for an emulsion composed of DCE–in–D_2O at 15 °C and the results are shown in Figure **6.2**. The spectra have been normalised for easier qualitative comparison due to the emulsions only being heated until they reached 65 °C, approx. 20 mins, rather than stirring them for 1 hour at 65 °C. This meant that the DCE was not fully saturated with the aqueous solution when the emulsion was cooled to 15 °C and the initial turbidity values are 1.26, 1.41 and 0.99 au for DCE–in–D_2O, H_2O–in–DCE and D_2O–in–DCE respectively.

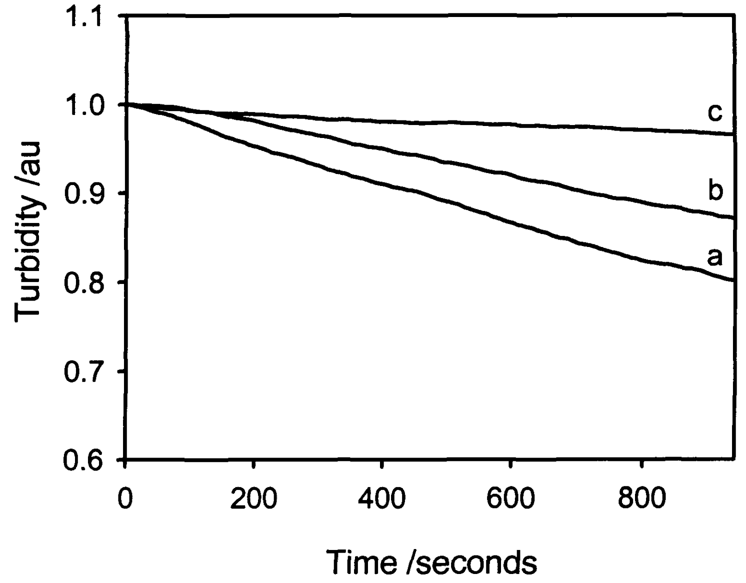

Figure 6.2: Graph comparing turbidity at 550 nm vs. time for emulsions containing (a) DCE–in–D_2O, (b) H_2O–in–DCE and (c) D_2O–in–DCE. The emulsions were formed at 15 °C and this temperature was maintained for the turbidity measurements. The original turbidity values were 1.26, 1.41 and 0.99 au, and the rate of change of turbidity with time for the plots are –172.6, –138.3 and –30.2 x10^{-6} au s^{-1} for the DCE–in–D_2O and, H_2O and D_2O–in–DCE emulsions respectively.

From Figure **6.2**, it can be seen that the water–in–oil systems were significantly more stable than an emulsion containing oil–in–water, with the change in the turbidity with time being reduced from –172.6 x10^{-6} au s^{-1} for DCE–in–D_2O, to –30.2 x10^{-6} au s^{-1} for a D_2O–in–DCE system. This is due to the viscosity of the DCE phase being much greater than that of the aqueous phase and the drops will move much slower in solution in a D_2O–in–DCE emulsion than in a DCE–in–D_2O system. Attempts were then made to stabilise the D_2O–in–DCE emulsion further using sucrose and TEACl in the aqueous phase and TEATPB in the DCE. Problems arose, however due to the small volume of the aqueous phase and this resulted in precipitates forming as the emulsion was cooled. The D_2O–in–DCE emulsion would be affected by creaming rather than sedimentation, due to the density of the aqueous drops being less than the density of the DCE, but the rate of destabilisation due to creaming could not be reduced due to the formation of precipitates when sucrose was included in the D_2O.

A single partitioning salt was therefore investigated as a method of emulsion stabilisation. An emulsion was created as in **2.4** using 1 cm^3 D_2O, and 10 cm^3 DCE containing 5 mM LiTPFB. After cooling to 15 °C for 30 mins, the turbidity of the sample was measured at 550 nm and this was compared to the spectra for an emulsion containing D_2O–in–DCE only, shown in Figure **6.2**, and a system of 5 mM LiTPFB DCE–in–1.5 M sucrose D_2O, shown in Figure **4.13** in **4.3.3**. The results are given in Figure **6.3** and the spectra have been normalised. The initial turbidity values are 0.99, 3.17 and 3.26 au for D_2O–in–DCE only, D_2O–in–5 mM LiTPFB DCE and 5 mM LiTPFB DCE–in–D_2O respectively. The large difference in the turbidity for the emulsions with and without LiTPFB is due to the experimental technique used to create the emulsions; i.e. the D_2O–in–DCE only emulsion was only heated for 20 mins whereas the emulsions containing LiTPFB were heated for 1 hour, and due to the LiTPFB lowering the surface tension between the DCE and water, this would increase the solubility of the two phases and cause a higher number density, and hence emulsion turbidity.

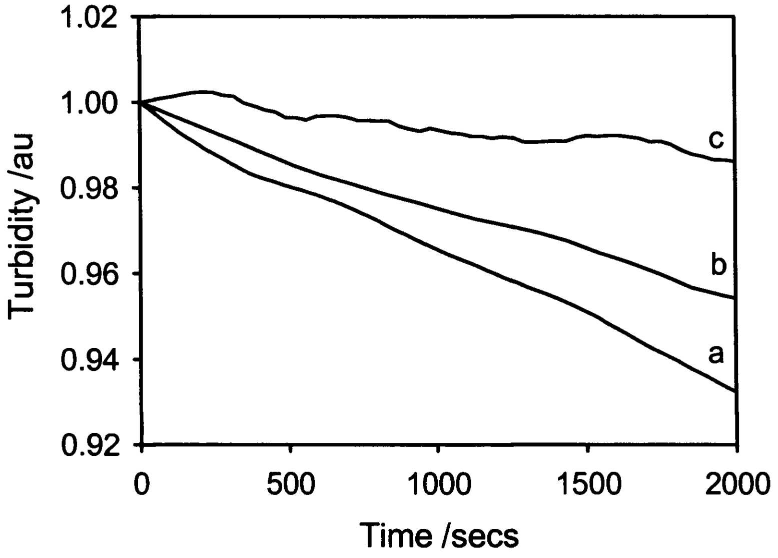

Figure 6.3: Graph comparing turbidity at 550 nm vs. time for emulsions containing (a) D_2O–in–DCE only, (b) D_2O–in–5 mM LiTPFB DCE and (c) 5 mM LiTPFB DCE–in–D_2O, measured at 15 °C. The original turbidity values were 0.99, 3.17 and 3.26 au, and the rate of change of turbidity with time for the plots are –30.2, –11.5 and –6.5 $x10^{-6}$ au s^{-1} for the D_2O–in–DCE, D_2O–in–5 mM LiTPFB DCE and 5 mM LiTPFB DCE–in–D_2O emulsions respectively.

Figure 6.3 shows that the presence of LiTPFB in the DCE phase causes further stabilisation of the emulsion than using D_2O–in–DCE only, by reducing the change in turbidity with time to –11.5 $x10^{-6}$ au s^{-1} from –30.2 $x10^{-6}$ au s^{-1}. This is due to the partitioning of the salt across the interface, hence setting up a Galvani–type potential and reducing the rate of coalescence. This stabilisation however, is not as efficient as that achieved by using 1.5 M sucrose combined with LiTPFB in a DCE–in–D_2O emulsion, giving a change in turbidity with time of –6.5 $x10^{-6}$ au s^{-1}.

The magnitude of the interfacial potential for the water–in–oil emulsion can also be calculated using Equation **6.1**, used in **4.3.4** as Equation **4.13** [74&88], and the value for the D_2O–in–DCE interface will be the same as for the DCE–in–D_2O interface at 15 °C, namely –22 mV.

$$\Delta_O^W\phi = \frac{\Delta_O^W\phi_+^o + \Delta_O^W\phi_-^o}{2} \qquad \textbf{6.1}$$

The Debye–Length will however be different due to the different dielectric permittivity of the DCE. Using Equation **6.2**, the value for $1/\kappa$ is calculated to be 1.5 nm, and because the drop separation distance will not be different for the water–in–oil and oil–in–water emulsions, due to the similar number densities, this value for the Debye–Length shows that the drop interaction distance is much less than the separation distance, 19 μm, supporting the DLVO theory of emulsion stability.

The drop volume and number density were also measured for the emulsion stabilised using LiTPFB, following the procedure in **2.6**, and the results are compared, in Table **6.3**, with those for a D_2O–in–DCE system and, from Table **4.12** in **4.3.3**, emulsions composed of DCE–in–1.5 M sucrose D_2O, and 5 mM LiTPFB DCE–in–1.5 M sucrose D_2O. The average drop diameter, in μm, has also been calculated and this is presented in brackets below the value for the drop volume in cm^3.

From Table **6.3**, it can be seen that there is no significant difference in the drop volume or diameter between the stabilised and unstabilised water–in–oil or oil–in–water emulsions. There is a slight increase however, in the number density for the D_2O–in–DCE emulsion stabilised using LiTPFB and this corresponds to an increase in the weight percent present as emulsion drops. This was also seen for the oil–in–

water emulsion stabilised using LiTPFB and sucrose, and is thought to be due to the potential–determining salt decreasing the surface tension between the oil and water, and hence increasing the solubility of the two phases in each other. The sucrose may also act in this way due to the weight percent of solution present as emulsion drops being greater for the emulsion containing oil–in–water stabilised with salts and sucrose (0.51 ±0.14 DCE wt %), compared with the emulsion containing water–in–oil stabilised with salts only (0.41 ±0.03 D_2O wt %).

Emulsion System	**Drop Volume /μm^3**	**Number Density /x10^6 drops cm^{-3}**	**Weight Percent Emulsion Drops**
D_2O–in–DCE	22 ±3 (3.5 ±0.06 μm)	150 ±15	0.34 ±0.05
D_2O–in–DCE (+ LiTPFB)	20 ±1 (3.4 ±0.04 μm)	200 ±14	0.41 ±0.03
DCE–in–D_2O (+ sucrose)	25 ±5 (3.6 ±0.2 μm)	140 ±12	0.35 ±0.06
DCE–in–D_2O (+ LiTPFB and sucrose)	25 ±6 (3.6 ±0.2 μm)	200 ±24	0.51 ±0.14

Table 6.3: Comparing the measured drop volume, number density and calculated weight percent of emulsion drops for a D_2O–in–5 mM LiTPFB DCE with values from Table **6.2**, for an emulsion containing D_2O–in–DCE only, and from **3.2.1**, for a DCE–in–1.5 M sucrose D_2O system and a 5 mM LiTPFB DCE–in–1.5 M sucrose D_2O emulsion. The value in brackets below that of the drop volume in cm^3 corresponds to the average drop diameter in μm.

6.4 Temperature Effects on the Water–in–Oil Emulsion

Due to condensation method used to create the emulsion, the drop volume is sensitive to changes in temperature. This was seen in **3.3.3**, for a DCE–in–D_2O emulsion, and it was assumed that a similar trend would be followed by a D_2O–in–DCE system. Two emulsions were created, following the procedure in **2.4**, composed of 10 cm^3 DCE and 1 cm^3 D_2O, and 5 mM LiTPFB DCE and 1 cm^3 D_2O respectively. These were heated to 65 °C for 1 hour and subsequently cooled to 15 °C for 30 mins and then a sample was taken for analysis using optical microscopy. This was placed in a cavity slide on the microscope temperature controller, as outlined in **2.6**, maintained at 15 °C. Once the measurement had been taken the temperature, of the water bath and microscope temperature controller, were increased to 20 °C and a second sample was taken for analysis. This was repeated in 5 °C increments until 30 °C and the results can be seen in Figure **6.4**. This was the highest temperature that could be measured accurately before the emulsion destabilised from the DCE evaporating out of the flask. Also this method of heating the bulk emulsion using the water bath was used, instead of that in **3.3.3** using the microscope temperature controller, because of the volatile nature of the DCE and the length of time of the experiment. When this method was attempted, the sample evaporated from the slide on the temperature controller after one measurement, approx 2 minutes, making it impossible to accurately measure the drop volume for more than one temperature using this technique.

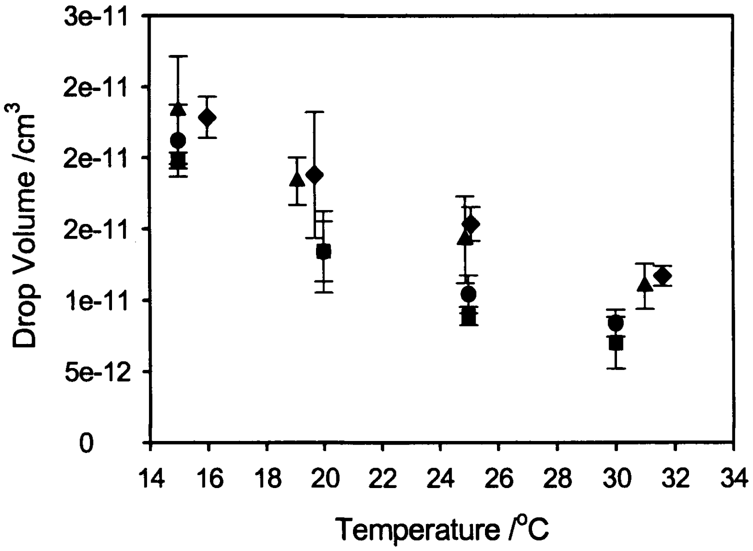

Figure 6.4: Emulsion drop volume vs. temperature for emulsions containing: (•) D_2O–in–DCE only and (■) D_2O–in–5 mM LiTPFB DCE. Also included is the data from Figure **4.14** in **4.3** for emulsions containing (♦) DCE–in–D_2O only and (▲) 5 mM LiTPFB DCE–in–D_2O. 1.5 M sucrose was included in these oil–in–water emulsions to improve stability.

Figure **6.4** shows that the volume of the D_2O drops is inversely proportional to the temperature, as expected, for the water–in–oil emulsions. When the results are compared with those for DCE–in–1.5 M sucrose D_2O and 5 mM LiTPFB DCE–in–1.5 M sucrose D_2O from Figure **4.14** in **4.4**, it can be seen that the water–in–oil emulsions follow a slightly different trend than the oil–in–water systems. This shows that as the temperature is increased, the drop volume for a water–in–oil emulsion is smaller than that for an oil–in–water system. This may be because of the different solubilities of water–in–DCE and DCE–in–water but is likely to be due to the method in which the readings were taken and the problems caused by the volatile nature of the DCE. To better compare the data with the literature solubility in Figure **6.1**, the weight percent of the D_2O emulsion drops was calculated using the initial number density of 150 ±15 $\times 10^6$ drops cm^{-3} for the D_2O–in–DCE only emulsion and

200 ±14 x10^6 drops cm^{-3} for the D_2O–in–5 mM LiTPFB DCE system, and these are shown in Figure **6.5**.

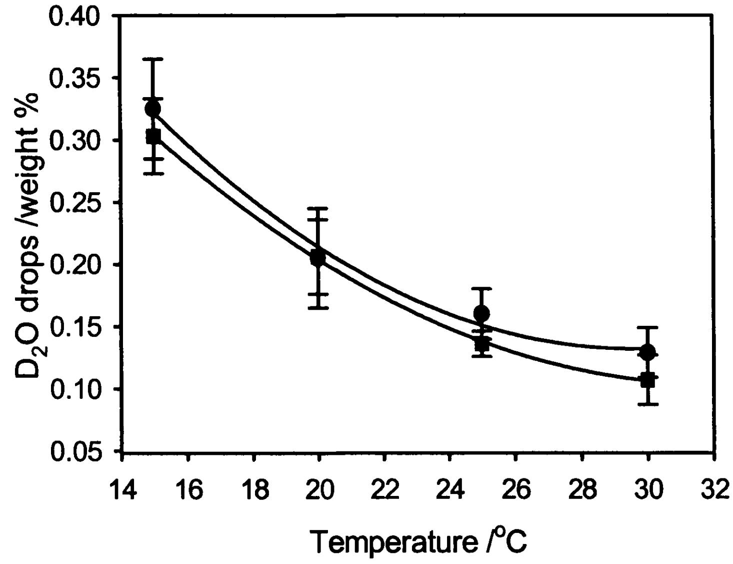

Figure 6.5: Graph showing the weight percent of D_2O as emulsion drops vs. the temperature of the system. For emulsions containing: (●) D_2O–in–DCE only and (■) D_2O–in–5 mM LiTPFB DCE. The solid lines are the regression fits using the equations: y=0.1+2.3$\exp^{-0.2x}$ for D_2O–in–DCE only, and y=0.05+1.2$\exp^{-0.1x}$ for the emulsion stabilised using LiTPFB.

From looking at Figure **6.5**, it can be seen that the two systems follow a similar trend and that this is similar to that for the literature solubility of water in DCE, in Figure **6.1**. This indicates that the change in drop volume with temperature follows the same trend as the solubility of water in DCE, as expected. This is also similar to the exponential trend observed in Figure **4.14** for emulsions containing DCE–in–1.5 M sucrose D_2O and 5 mM LiTPFB DCE–in–1.5 M sucrose D_2O, and for the literature solubility of DCE in water.

6.5 Electrodeposition at the Emulsion Interface

The interfacial potential, set–up by the potential–determining salts, can be utilised to electrodeposit metal at the liquid–liquid interface, as described in **1.1.3**, and experiments were carried out to electrodeposit palladium at both the oil–in–water and water–in–oil interfaces, following the redox reaction in Equation **6.2** [110].

$$(NH_4)_2PdCl_{4(aq)} + 2DmFc_{(org)} \rightarrow (NH_4)_2Cl_4{}^{2-}{}_{(aq)} + 2DmFc^+{}_{(org)} + Pd^0{}_{(m)} \qquad \textbf{6.2}$$

Where $(NH_4)_2PdCl_{4(aq)}$ is ammonium tetrachloropalladate (II) dissolved in the aqueous phase and DmFc corresponds to dimethylferrocene dissolved in the DCE phase. Due to the Condensation method used to produce the emulsion, one of the redox reagents had to be added after the emulsion had formed; otherwise the electrodeposition would occur during emulsion formation. For the DCE–in–D_2O emulsion, this was the $(NH_4)_2PdCl_4$ and, for the D_2O–in–DCE system, the DmFc was added last. The Galvani peak potential for the electrochemical reduction of $(NH_4)_2PdCl_4$ at the DCE–water interface has been determined to be $\Delta_O^W\phi_p = 273$ mV [110] and therefore the interfacial potential for the emulsion would need to be of a similar or greater value to drive the electron transfer reaction.

Emulsions with 0.5 mM DmFc DCE–in–D_2O only and 0.5 mM DmFc 5 mM LiTPFB DCE–in–D_2O were created as described in **2.4**. 1.5 M sucrose, 50 mM lithium chloride (LiCl) and 50 mM lithium sulphate (Li_2SO_4) were also included in the D_2O for stabilisation and to 'salt–out' the solution, preventing the DmFc oxidising during emulsion formation and before the $(NH_4)_2PdCl_4$ was added. Once the emulsions had formed and cooled at 15 °C for 30 mins, 3 cm^3 samples were taken and to these, 1 $x10^{-2}$ cm^3 $(NH_4)_2PdCl_4$ in D_2O were added to make a concentration of 2.5 mM in the sample. This was because, from Equation **6.2**, a 2:1 ratio of moles of DmFc to $(NH_4)_2PdCl_4$ were needed for the maximum amount of electrodeposition to occur. The samples were then mixed gently and left to stand for 5 mins. It was difficult to discern if deposition had occurred, due to the palladate destabilising the emulsion slightly as it was added, hence causing dilution of the sample also described in **4.6**, and the brown colour of the palladate solution masking any obvious colour change of the DmFc from yellow to green in the emulsion. The sample containing LiTPFB, however, did appear to change to a darker colour, when compared with the sample that contained no salts. The samples could not be left to phase separate to determine if deposition had occurred because deposition would occur slowly, even when there was no interfacial potential. This was seen when the samples were left to stand overnight because, not only was there the appearance of a brown/grey deposit in the sample containing 5 mM LiTPFB, there was also a trace of brown/grey deposit in the sample containing no salts, although these were not measured quantitatively.

Similar observations were made when the DmFc concentration was increased from 0.5 mM to 5 mM and 20 mM. For this experiment, the emulsions were created as in **2.4**, containing 5 m M LiTPFB in the DCE, and the concentration of $(NH_4)_2PdCl_4$ added was increased according to the concentration of DmFc used. In particular, the sample containing 20 mM DmFc appeared to deposit palladium spontaneously as the $(NH_4)_2PdCl_4$ was added, with the emulsion going a very dark brown colour. The amount of palladium deposited was also seen to increase, with increasing DmFc concentration, however the quantities could not be measured. Some of the deposit was extracted, however, from the sample containing 20 mM DmFc and analysed using Electron Microscopy (SEM) with X–Ray diffraction (EDAX) as described in

2.8. The sample was mounted onto a conducting self–adhesive tab on an aluminium stub and the SEM showed particles of μm size, identified as palladium using the EDAX. A typical image and analysis spectrum are shown as Figures **6.6a** and **b**.

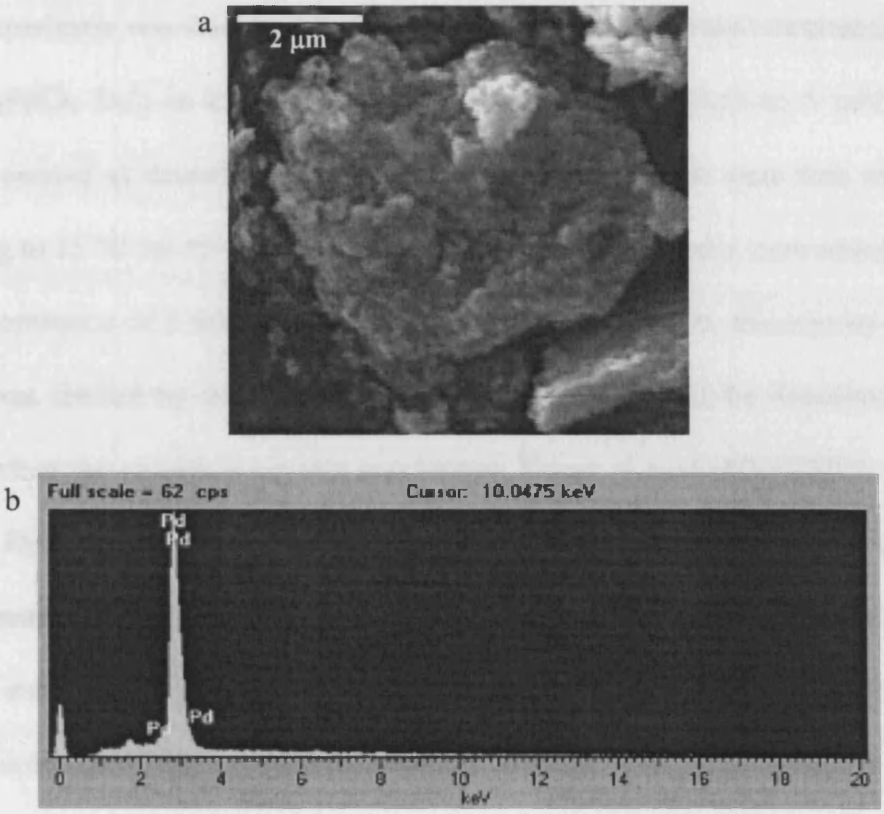

Figure 6.6: Typical SEM image of an electrodeposited particle (a) and an EDAX spectrum identifying the particle as palladium metal (b).

From Figure **6.6a** it can be seen that the palladium particle is not perfectly spherical and smooth, and instead appears to have a bumpy surface. This may be due to the emulsion drops destabilising, and hence changing in volume, as the deposition was occurring. The experiments were also carried out using THpABr but again, as for the emulsion without salts, no deposition was observed.

Because deposition was only seen when LiTPFB was used, it suggests that the interfacial potential for this emulsion is much higher than –22 mV due to the salts being able to drive the redox reaction. This indicates that the calculated potential is incorrect and supports the experimental evidence suggesting that the potential for single-salt emulsions are in fact >400 mV (compared with the calculated potentials for an emulsion stabilised with $TBuA^+$).

The experiment was then repeated using water–in–oil emulsions composed of 1 mM $(NH_4)_2PdCl_4$ D_2O–in–DCE only and 1 mM $(NH_4)_2PdCl_4$ D_2O–in–5 mM LiTPFB DCE, created as described in **2.4**. Samples of the emulsion were then taken after cooling to 15 °C for 30 mins and to these, 1 $\times 10^{-2}$ cm^3 of DmFc were added to make a concentration of 2 mM in the sample. In these experiments, the amount of DmFc used was limited by the amount of $(NH_4)_2PdCl_4$ that could be dissolved into the DCE when the emulsion mixture was heated. When 10 mM $(NH_4)_2PdCl_4$ was used in the D_2O, as used for the oil–in–water emulsion, precipitates were seen to form upon heating. After the DmFc had been added to the samples, this was mixed in gently and then the samples were observed. There was an obvious colour change in the sample containing LiTPFB from yellow to green corresponding to the oxidation of DmFc to $DmFc^+$ although there was no visible sign of deposition. There was no colour change, however, in the sample composed of $(NH_4)_2PdCl_4$ D_2O–in–DCE only. To determine if palladium was present in either sample, the samples were analysed using SEM with EDAX and Electron Microscopy X–Ray Analysis (EMXA). Because there was no obvious sign of deposition, the liquid sample was evaporated onto pure carbon stubs; this was possible because there was no sucrose, LiCl or Li_2SO_4 in the sample which would mask the palladium when analysed. There did seem to be some deposition or precipitate, when the samples were analysed using SEM, but no palladium was identified using the EDAX. Palladium was found using EMXA but the quantities were very low and more indicative of palladium precipitates than an electrodeposited particle. This suggested that the

DmFc had oxidised in the DCE solution before it reached the oil–water interface and therefore no electrodeposition had taken place. This only occurred in the sample containing LiTPFB and therefore verified that the salt acted as a catalyst for the redox reaction. It also highlighted the importance of the LiCl and Li_2SO_4 in the aqueous phase of the emulsion to prevent the DmFc oxidising with something other than the $(NH_4)_2PdCl_4$ at the interface.

A possible way to control the deposition would be to use the two–salt stabilising system. This is because the interfacial potential could be changed, simply by changing the emulsion drop volume, and hence the concentration of salt in the drops, of the system. This would be achieved by forming the emulsion and then merely increasing the temperature. Therefore, by controlling the interfacial potential, a "window" similar to that used in conventional electrochemistry with a Potentiostat, could be created where the limits were either side of the electron transfer potential for $Pd^{2+} \rightarrow Pd^0$ ($\Delta_O^W\phi_p = 273$ mV).

6.6 Conclusions

A D_2O–in–DCE emulsion was successfully created in **6.2** using a condensation method and was seen to be more stable than an emulsion containing DCE–in–D_2O; -30.2×10^{-6} au s^{-1} compared with -172.6×10^{-6} au s^{-1} for D_2O–in–DCE and DCE–in–D_2O respectively. This was due to the different viscosities of the DCE and D_2O and because this restricted the motion of the D_2O drops in DCE when compared with DCE drops in D_2O.

The water–in–oil emulsion was then characterised using optical microscopy and UV–Vis spectrophotometry and was found to have an initial number density of 150 ±15 x10^6 drops cm^{-3} and an initial average drop volume of 22 ±3 μm^3. These were comparable to those determined for the DCE–in–D_2O emulsion, 140 ±12 x10^6 drops cm^{-3} and 25 ±5 μm^3, respectively, and show that the weight percent of the condensed emulsion drops was similar for both systems, irrespective of their differing solubilities.

The emulsion was then successfully stabilised in **6.3** by dissolving the potential–determining salt, LiTPFB, in the DCE phase to set–up a Galvani–type potential across the water/oil interface. This reduced the effect of coalescence and improved the rate of change of turbidity with time from -30.2×10^{-6} au s^{-1} to -11.5×10^{-6} au s^{-1}, but this was still less stable than an emulsion of DCE–in–D_2O stabilised with LiTPFB and sucrose; -6.5×10^{-6} au s^{-1}.

The drop volume and number density were then measured, 20 ±1 μm^3 and 200 ±14 x10^6 drops cm^{-3}, for the water–in–oil emulsion stabilised using LiTPFB and the drop volume was found to be similar to those measured for the unstabilised emulsion (22 ±3 μm^3 and 150 ±15 x10^6 drops cm^{-3}) and also to those measured for the oil–in–water systems (DCE–in–1.5 M sucrose D_2O: 25 ±5 μm^3 and 140 ±12 x10^6 drops cm^{-3}, 5 mM LiTPFB DCE–in–1.5M sucrose D_2O: 25 ±6 μm^3 and 200 ±24 x10^6 drops cm^{-3}). The number density was significantly higher for both the emulsions stabilised using LiTPFB and this was believed to be due to the salts lowering the surface tension between the two phases, hence increasing the solubility of the water in oil and the oil in water. It was thought that the sucrose may also affect the solubility and surface tension between the two phases due to the difference in the weight percent of the emulsion drops being higher for the emulsion containing 5 mM LiTPFB DCE–in–1.5 M sucrose D_2O (0.51 ±0.14 wt %) compared to that for the emulsion D_2O–in–5 mM LiTPFB DCE (0.41 ±0.03 wt %).

The magnitude of the interfacial potential for the D_2O–in–5 mM LiTPFB DCE emulsion was also determined in **6.3**, and was found to follow the same equation as that for the 5 mM LiTPFB DCE–in–1.5 M sucrose D_2O emulsion. The calculated potential was therefore found to be –22 mV.

In **6.4**, the effect of temperature changes was investigated and the weight percent of D_2O emulsion drops was found to follow the same trend with temperature as the solubility of water in DCE, as expected. This was the same trend as that followed by the solubility of DCE in water and the weight percent of DCE emulsion drops with temperature.

A possible application of the LiTPFB stabilised water–in–oil and oil–in–water emulsions was then investigated in **6.5**. This utilised the interfacial potential established by LiTPFB to drive the electrodeposition of palladium at the liquid–liquid interface with promising results.

Chapter 7: Concluding Remarks

7.1 Conclusions

7.1.1 Creation, Characterisation and Stabilisation of Oil–in–Water and Water–in–Oil Emulsions

In Chapter **3**, a method was devised to reproducibly create DCE–in–water emulsions without the use of surfactants. This used a condensation technique where the mixture of the two liquids was heated to 65 °C for 1 hour with stirring, and then subsequently cooled rapidly to a recorded temperature for 30 mins; 15 °C for most experiments. This technique could be used for both oil–in–water and water–in–oil emulsions because it depended only on the solubility of the drop phase in the continuous phase, with respect to temperature.

The turbidity with time for both systems was measured in Chapters **3** and **6** using UV–Vis spectrophotometry, and it was seen that the emulsion composed of D_2O–in–DCE was more stable relative to an emulsion containing DCE–in–D_2O; -30.2×10^{-6} au s^{-1} compared with -172.6×10^{-6} au s^{-1} for D_2O–in–DCE and DCE–in–D_2O respectively. This was due to the different viscosities of the DCE and D_2O and because this restricted the motion of the D_2O drops in DCE when compared with DCE drops in D_2O. Both systems still destabilised rapidly over time, however, and in particular, the emulsion containing DCE–in–D_2O was seen to double in drop volume after 7 hours in a sealed container. The emulsion drops were also found to be very sensitive to external shear and this was shown when using conventional light scattering and electrochemical techniques.

The destabilisation effects of sedimentation and coalescence were reduced for the DCE–in–water and water–in–DCE emulsions in Chapters **4** and **6** respectively. For the oil–in–water system, 1.5 M sucrose was dissolved in the aqueous phase and this was found to successfully reduce the sedimentation of the DCE drops by matching the densities of the two emulsion phases. The inclusion of sucrose reduced the rate of change in turbidity with time from –172.6 x10^{-6} au s^{-1} to –23.5 x10^{-6} au s^{-1}. This rate was reduced further by limiting the rate of coalescence of the drops and was done by setting–up a Galvani–type potential across the liquid–liquid interface. Two systems were investigated; a single partitioning salt soluble in both phases i.e. $LiTPFB_{(aq/org)}$ and $THpABr_{(aq/org)}$, and a two–salt system with different concentrations of a 'common ion' in both liquids, i.e. $TEACl_{(aq)}$ and $TEATPB_{(org)}$, or $TBuACl_{(aq)}$ and $TBuATPB_{(org)}$.

It was found that LiTPFB gave the best stabilisation to the DCE–in–D_2O emulsion in Chapter **4**, reducing the change in turbidity with time to –6.5 x10^{-6} au s^{-1}, and effectively causing insignificant changes to the emulsion drop volume over the first two hours when used in conjunction with sucrose. This salt was also seen to successfully stabilise the D_2O–in–DCE emulsion in Chapter **6**, giving a change in turbidity with time of –11.5 x10^{-6} au s^{-1} compared to –30.2 x10^{-6} au s^{-1} for the emulsion containing D_2O–in–DCE only. The reason for this increase in stabilisation was uncertain due to the magnitude of the interfacial–potential set–up by the single–salt system being much less than that calculated for the two–salt system; –22 mV for both the LiTPFB stabilised DCE–in–D_2O and D_2O–in–DCE emulsions compared with 205 ±17 and –474 ±19 mV for systems containing TEA^+ and $TBuA^+$ at 15 °C respectively. The potential calculated for the THpABr stabilised emulsion was also unexpectedly low, –106 mV, and it was therefore suggested that the literature equation used in the calculation was not suitable for this type of distribution potential. The potentials for the two–salt system were calculated using UV–Vis spectroscopy in Chapter **4**, to determine the concentration of ions in the emulsion oil drops. It was suggested that the increased stability from the single–salt emulsions may be due to their action of lowering the interfacial tension, as seen from the calculated drop weight percent, but it was unlikely that this would cause such a large increase in the stability.

Both DCE–in–water and water–in–DCE emulsions were characterised in Chapters **3**, **4** and **6**, using optical microscopy to measure the drop volume and number density, and both emulsions were found to have an initial average drop volume of 24 ±5 μm^3 (3.6 ±0.2 μm diameter), irrespective of stabilising system used, and the initial number density was determined to be 141 ±17 $x10^6$ drops per cm^3 for the emulsions composed of DCE–in–D_2O (with sucrose only and TEA^+ or $TBuA^+$) and D_2O–in–DCE. For the emulsion stabilised using THpABr, the number density increased to 170 ±19 $x10^6$ drops per cm^3 for the oil–in–water system, and for LiTPFB this increased further to 200 ±16 $x10^6$ drops per cm^3 for both emulsions containing oil–in–water and water–in–oil. It was thought that the number density was significantly higher for both the emulsions stabilised using LiTPFB due to the salts lowering the surface tension between the two phases, hence increasing the solubility of the water in oil or the oil in water. It was thought that the sucrose may also affect the solubility and surface tension between the two phases due to the difference in the weight percent of the emulsion drops being higher for the emulsion containing 5 mM LiTPFB DCE–in–1.5 M sucrose D_2O (0.51 ±0.14 wt %) compared to that for the emulsion D_2O–in–5 mM LiTPFB DCE (0.41 ±0.03 wt %). The weight percent of the condensed emulsion drops in the other emulsion systems investigated was calculated to be 0.36 ±0.08 wt %, irrespective of the differing solubilities of DCE in water and water in DCE.

Overall both DCE–in–water and water–in–DCE emulsions were reproducibly created using a condensation technique and characterised using optical microscopy and UV–Vis spectrophotometry. These emulsions were then successfully stabilised using 5 mM LiTPFB in the DCE phase to reduce coalescence and, for the oil–in–water system, 1.5 M sucrose to reduce sedimentation. The stabilisation was effective over the first two hours, enabling the emulsion to be studied using SANS, and a possible application of the LiTPFB stabilised water–in–oil and oil–in–water emulsions was investigated in Chapter **6**, utilising the interfacial potential established by the LiTPFB to drive the electrodeposition of palladium at the liquid–liquid interface.

7.1.2 The Effect of Temperature on the Oil–in–Water and Water–in–Oil Emulsions

Due to the dependence of the drop volume on the phase solubility, the emulsions were seen to be sensitive to changes in temperature, with the drop volume being inversely proportional to an increase in temperature, irrespective of the inclusion of stabilising sucrose or salts. This phenomenon was shown to be reversible and that the drop volume could be controlled using temperature changes. This was only dependent on the temperature being changed by 1–2 °C per minute, rather than 1–2 °C per second, because if the temperature change occurred too quickly, a secondary emulsion would start to nucleate and grow from the DCE dissolved in the aqueous phase, rather than this adding volume to the original emulsion drops. The sensitivity of the drop volume to temperature was also seen to be the same for both the DCE–in–D_2O and the D_2O–in–DCE systems, and these in turn followed the same trend as the literature solubilities for the two liquids.

Although it has been shown that the stabilising salts LiTPFB and THpABr affect the solubility of DCE in water and water in DCE, this is only a significant effect in the formation of the emulsion and affects the bulk emulsion density. For the experiments investigating the change in drop volume with temperature, any effect of the salts on the solubility of the phases was too small to be detected due to the small temperature changes and experimental errors.

7.1.3 Investigations of Bovine Serum Albumin Adsorption at the DCE–Water Interface

The emulsion containing BSA was characterised using optical microscopy with and without the potential–determining salt LiTPFB in Chapter **5**, and the addition of protein was shown to give greater stability to the emulsion, irrespective of the presence of salt. BSA was seen, however, from D11 SANS data, to also form a secondary microemulsion with an average drop volume of 0.006 μm^3 and an average number density of 3000000 x10^6 drops cm^{-3} (compared with 17 μm^3 and 200 x10^6 drops cm^{-3} for the primary emulsion). This secondary microemulsion had a measured volume fraction of 0.13 ±0.02 %v and accounted for the discrepancy between the calculated weight percent of drops in the emulsions with and without BSA.

From the SANS experiments using D11 at the ILL, it was seen that the inclusion of potential–determining salts had an effect on an interfacial adsorbed layer of BSA, and both systems with and without salts, were seen to be comparable in thickness to that determined in the literature; 40.3 Å for the emulsion containing salts compared with 40 Å, while the layer for the emulsion without salts, was slightly larger at 47.9 Å. This was believed to be due to there being solvated water in the BSA layer; 20 % water and 80 % protein, whereas when salts were used, this protein layer contained no water. The salts may also have increased the amount of adsorbed protein, hence creating a complete monolayer, whereas for the emulsion without salts, the protein may have been adsorbed as islands with a more defined globular structure.

Sans data obtained from D22 at the ILL and LOQ at ISIS were used for qualitative comparison due to experimental errors preventing quantitative analysis of the data. The results confirmed an effect of salts on the adsorbed protein layer and also showed that the salts caused a change in the scattering from the 'clean' interface. Overall it was seen that the most analysable data was obtained from D11 at the ILL, due to the lower *Q*–range accessible caused by the longer sample–detector distance, and that this was able to give structural information regarding the adsorption of BSA at the DCE–water interface.

7.2 Future Work

7.2.1 Emulsion Characterisation and Stabilisation

There is still a lot of work to be done regarding the characterisation of both the oil–in–water and water–in–oil emulsion; in particular the size distribution needs to be measured. Fitted results from D11 gave a value for the emulsion polydispersity to be 0.3 ±0.005, consistent with a small size distribution, but this was for the microemulsion formed when using BSA and so cannot be accurately applied to the 'larger' emulsion drops observed with optical microscopy.

Another important measurement would be that of the interfacial tension between the DCE and water, with and without THpABr and LiTPFB. It would be interesting to investigate how this change in surface tension changes the solubility of the oil in water and affects the emulsion stability, and also whether using $TPFB^-$ as the 'common ion' in a two–salt emulsion causes further stabilisation. This is because, even though the standard ion–transfer potential for this potential–determining ion is unknown, it is thought to have a very high Gibbs energy of transfer and is commonly used as a background electrolyte to create a potential window in electrochemistry experiments.

Other experiments that could be carried out to characterise the emulsion, would include measuring the drop volume and number density at different cooling temperatures. From looking at the literature on nucleation, it can be seen that once the supersaturation limit is reached and then the emulsion is cooled rapidly, a finite number of nucleation sites form in a period of time depending on how far the concentration is above the critical amount. This theory could be confirmed by heating the emulsions to 65 °C for 1 hour and then cooling to different forming temperatures, i.e. 25, 35, 45 and 55 °C, and comparing the measured volume and number density for each cooling temperature. It should be seen that the number density is always constant and that the volume changes according to the solubility of oil in water at the lower temperature. Also the rate of cooling could be investigated due to this being the driving force behind the initial nucleation.

Another set of experiments that need to be undertaken is to determine the Coulomb interactions in the DLVO calculations. For these the zeta-potential needs to be determined but another approach would be to add an aqueous electrolyte to the emulsion to change the Debye–Length of the solution and then see how this affects the emulsion stability.

7.2.2 Investigating the Emulsion Interface using SANS

Once the emulsion has been characterised at different forming temperatures, this knowledge could be used in future SANS experiments. This is because there is currently no diffractometer that can go to $Q = 0.00015$ Å^{-1} and therefore to observe the emulsion drops in their entirety, a smaller drop size would need to be used. This could be achieved by forming the emulsion at a higher temperature than 15 °C and this would then enable the investigation of the 'clean' emulsion liquid–liquid interface.

There are also many other experiments that could be done using SANS with the surfactantless emulsion, e.g. investigating other proteins, such as Thermolysin which is very temperature resistant and has a rigid shape. The data from this could then be compared with that obtained for the flexible protein BSA and differences in the adsorbed layer could be examined. For these experiments to be successful, it is imperative that a more refined analysis model is developed that can distinguish between a diffuse protein layer and a fixed uniform slab. This would be important for analysis of the 'clean' interface and might help to confirm whether the DCE–water interface is molecularly sharp or a diffuse mixing region.

7.2.3 Electrodeposition at the Emulsion Interface

Finally another interesting application of the surfactantless emulsion would be its use in electrodeless electrodeposition. Current work is being carried out in the Caruana research group by J. Sanchez, to electrodeposit palladium at the emulsion interface. This has been primarily using perchlorate as the potential–determining ion in a two–salt stabilised water–in–DCE emulsion, with promising results showing conclusive images of 4 μm diameter palladium spheres under SEM.

Future work concerning this would then be to control the deposition using temperature to manipulate the drop size and hence the interfacial potential. This would, therefore be dependent on the salt–system used and also the metal deposited.

7.3 Summary

Overall, a lot of progress has been made regarding the stabilisation and characterisation of both the DCE–in–water and water–in–DCE surfactantless emulsions, and also in understanding how they are formed and affected by shear and temperature, but there is a lot of information still to be obtained. There is a lot of interesting work yet to be done utilising the surfactantless emulsion; not only as a model for structural characterisation of the liquid–liquid interface with and without proteins, but also as an 'organic' potentiostat that can be used in the electrodeposition of palladium.

Chapter 8: References

[1] M.A. Leich, G.L. Richmond; *Faraday Discuss.*; **129** (2005) 1.

[2] I. Benjamin; *J. Phys. Chem. B.*; **109** (2005) 13711.

[3] I. Benjamin; *Prog. React. Kinet. Mech.*; **27** (2002) 87.

[4] D. Michael, I. Benjamin; *J. Chem. Phys.*; **114** (2001) 2817.

[5] I. Benjamin; *Annu. Rev. Phys. Chem.*; **48** (1997) 401.

[6] I. Benjamin; *Acc. Chem. Res.*; **28** (1995) 233.

[7] I. Benjamin; *J. Chem. Phys.*; **97** (1992) 1432.

[8] P. Jedlovszky, Á. Keresztúri, G. Horvai; *Faraday Discuss.*; **129** (2005) 35.

[9] P. Jedlovszky, A. Vincze, G. Horvai; *Phys. Chem. Chem. Phys.*; **6** (2004) 1874.

[10] P. Jedlovszky, A. Vincze, G. Horvai; *J. Mol. Liq.*; **109** (2004) 99.

[11] B. Su, N. Eugster, H.H. Girault; *J. Electroanal. Chem.*; **577** (2005) 187.

[12] Z. Samec, N. Eugster, D.J. Fermin, H.H. Girault; *J. Electroanal. Chem.*; **577** (2005) 323.

[13] K.E. Wardle, D.J. Henderson, R.L. Rowley; *Fluid Phase Equilib.*; **233** (2005) 96.

[14] H.B. Wang, E. Carlson, D. Henderson, R.L. Rowley; *Mol. Simulat.*; **29** (2003) 777.

[15] J.B. Buhn, P.A. Bopp, M.J. Hampe; *Fluid Phase Equilib.*; **224** (2004) 221.

[16] J.P. Nicolas, N.R. de Souza; *J. Chem. Phys.*; **120** (2004) 2464.

[17] S. Frank, W. Schmickler; *J. Electroanal. Chem.*; **564** (2004) 239.

[18] C.F. Lopez, S.O. Nielson, M.L. Klein, P.B. Moore; *J. Phys. Chem. B*; **108** (2004) 6603.

[19] B. Schnell, R. Schurhammer, G. Wipff; *J. Phys. Chem. B*; **108** (2004) 2285.

[20] P.Jedlovsky, A. Vincze, G. Horvai; *J. Chem. Phys.*; **117** (2002) 2271.

[21] H.H. Girault, D.J. Schiffrin, in: A.J. Bard (Ed.); *Electroanalytical Chemistry*; (1989) Dekker: New York, 1.

[22] W.H. Steel, C.L. Beildeck, R.A. Walker; *J. Phys. Chem. B*; **108** (2004) 16107.

[23] W.H. Steel, R.A. Walker; *Nature*; **424** (2003) 296.

[24] H.J. Paul, R.M. Corn; *J. Phys. Chem. B*; **101** (1997) 4494.

[25] D.A. Higgins, R.M. Corn; *J. Phys. Chem.*; **97** (1993) 489

[26] T. Uchida, A. Yamaguchi, T. Ina, N. Teramae; *J. Phys. Chem. B*; **104** (2000) 12091.

[27] X. Chen, M.L. Clarke, J. Wang, Z. Chen; *Int. J. Mod. Phys. B*; **19** (2005) 691.

[28] L.F. Scatena, G.L. Richmond; *J. Phys. Chem. B*; **108** (2004) 12518.

[29] D.S. Walker, M.G. Brown, C.L. McFearin, G.L. Richmond; *J. Phys. Chem. B*; **108** (2004) 2111.

[30] M.M. Knock, G.R. Bell, E.K. Hill, H.J. Turner, C.D. Bain; *J. Phys. Chem. B*; **107** (2003) 10801.

[31] V.Rampon, C. Genot, A. Riaublanc, A. Anton, M.A.V. Axelos, D.J. McClements; *J. Agr. Food Chem.*; **51** (2003) 2490.

[32] Y. Moriya, S. Nakata, H. Morimoto, N. Ogawa; *Anal. Sci.*; **20** (2004) 1533.

[33] Y. Moriya, T. Hasegawa, K. Hayashi, M. Maruyama, S. Nakata, N. Ogawa; *Anal. Bioanal. Chem.*; **376** (2003) 374.

[34] B.G. Dzikovski, V.A. Livshits; *Phys. Chem. Chem. Phys.*; **5** (2003) 5271.

[35] S. Ishizaka, S. Kinoshita, Y. Nishijima, N. Kitamura; *Anal Chem.*; **75** (2005) 6035.

[36] S. Ishizaka, H–B. Kim, N. Kitamura; *Anal. Chem.*; **73** (2001) 2241.

[37] T. Yamashita, T. Uchida, T. Fukushima, N. Termae; *J. Phys. Chem. B*; **107** (2003) 4786.

[38] K. Nochi, A. Yamaguchi, T. Hayashita, T. Uchida, N. Teramae; *J. Phys. Chem. B*; **106** (2002) 9906.

[39] T. Kakiuchi, K. Ono, Y. Takasu; *Anal. Chem.*; **70** (1998) 4152.

[40] J.W. Benjamins, K. Thuresson, T. Nylander; *Langmuir*; **21** (2005) 149.

[41] B.P. Binks, J.H. Clint, A.K.F. Dyab, P.D.I. Fletcher, M. Kirkland, C.P. Whitby; *Langmuir*; **19** (2003) 8888.

[42] S. Uredat, G.H. Findenegg; *Langmuir*; **15** (1999)1108.

[43] Z. Samec, A. Trojánek, P. Krtil; *Faraday Discuss.*; **129** (2005) 301.

[44] H. Yui, Y. Ikezoe, T. Sawada; *Anal. Sci.*; **20** (2004) 1501.

[45] Y. Uchiyama, H. Yui, T. Sawada; *Anal. Sci.*; **20** (2004) 1537.

[46] Z.H. Cheng, F. Ping, F.L. Yuan, J.T. Ke, Y.W. Hui; *Anal. Chim. Acta*; **538** (2005) 337.

[47] B.P. Xiao, Z.H. Cheng; *J. Pharmaceut. Biomed. Anal.*; **35** (2004) 185.

[48] M.L. Schlossman; *Phyisca B*; **357** (2005) 98.

[49] L. Guangming, S. Malkova, S. Venkatesh Pingali, D.G. Schultz, B. Lin, M. Meron, T.J. Graber, J. Gebhardt, P. Vanysek, M.L. Schlossman; *Faraday Discuss.*; **129** (2005) 23.

[50] S. Venkatesh Pingali, T. Takiue, G. Luo, A.M. Tikhonov, N. Ikeda, M. Aratono, M.L. Schlossman; *J. Phys. Chem. B*; **109** (2005) 1210.

[51] M. Li, A.M. Tikhonov, M.L. Schlossman; *Europhys. Lett.*; **58** (2002) 80.

[52] S. Streit, M. Sprung, C. Gutt, M. Tolan; *Physica B*; **357** (2005) 110.

[53] M. Adachi, Y. Murata, K. Sago, K. Nakagawa; *Langmuir*; **20** (2004) 5965.

[54] A. Zarbakhsh, A. Querol, J. Bowers, J.R.P. Webster; *Faraday Discuss.*; **129** (2005) 155.

[55] J. Penfold, R.M. Richardson, A. Zarbakhsh, J.R.P. Webster, D.G. Bucknall, A.R. Rennie, R.A.L. Jones, T. Cosgrove, R.K. Thomas, J.S. Higgins, P.D.I. Fletcher, E. Dickinson, S.J. Roser, I.A. McLure, A.R. Hillman, R.W. Richards, E.J. Staples, A.N. Burgess, E.A. Simister, J.W. White; *J. Chem. Soc. Faraday Trans.*; **93** (1997) 3899.

[56] A. Bumajdad, J. Eastoe, S. Nave, D.C. Steytler, R.K. Heenan, I. Grillo; *Langmuir*; **19** (2003) 2560.

[57] E. Alami, S. Abrahmsén–Alami, J. Eastoe, R.K. Heenan; *Langmuir*; **19** (2003) 18.

[58] A. Bumajdad, J. Eastoe, R.K. Heenan; *Langmuir*; **19** (2003) 7219.

[59] R.K. Heenan, J. Eastoe; *J. Appl. Cryst.*; **33** (2000) 749.

[60] T. Riley, C.R. Heald, S. Stolnik, M.C. Garnett, L. Illum, S.S. Davis, S.M. King, R.K. Heenan, S.C. Purkiss, R.J. Barlow, P.R. Gellert, C. Washington; *Langmuir*; **19** (2003) 8428.

[61] D.J. Barlow, M.J. Lawrence, T. Zubert, S. Zuberi, R.K. Heenan; *Langmuir*; **16** (2000) 10398.

[62] G. Ma, D.J. Barlow, M.J. Lawrence, R.K. Heenan, P. Timmins; *J. Phys. Chem. B*; **104** (2000) 9081.

[63] T.P. O'Sullivan, M.E. Vickers, R.K. Heenan; *J. Appl. Cryst.*; **24** (1991) 732.

[64] J. Bowers, A. Zarbakhsh, J.R.P. Webster, L.R. Hutchings, R.W. Richards; *Langmuir*; **17** (2001) 140.

[65] J. Strutwolf, A.L. Barker, M. Gonsalves, D.J. Caruana, P.R. Unwin, D.E. Williams, J.R.P. Webster; *J. Electroanal. Chem.*; **483** (2000) 163.

[66] E. Staples, J. Penfold, I. Tucker; *J. Phys. Chem. B*; **104** (2000) 606.

[67] G. Salamat, R. de Vries, E.W. Kaler, S. Satija, L. Sung; *Langmuir*; **16** (2000) 102.

[68] V. Beni, M. Ghita, D.W.M. Arrigan; *Biosens. Bioelectron.*; **20** (2005) 2097.

[69] A. Sherburn, D.W.M. Arrigan, R.A.W. Dryfe, N.M. Boag; *Electroanal.*; **16** (2004) 1227.

[70] T. Laaksonen, P. Ahonen, K. Kontturi, L. Murtomäki; *J. Electroanal. Chem.*; **575** (2005) 75.

[71] A. Juarez, A.M. Baruzzi, L.M. Yudi; *J. Electroanal. Chem.*; **577** (2005) 281.

[72] F. Quentel, V. Mirceski, M. L'Her; *Anal. Chem.*; **77** (2005) 1940.

[73] V.J. Cunnane, D.J. Schiffrin, C. Beltran, G. Geblewicz, T. Solomon; *J. Electroanal. Chem.*; **247** (1988) 203.

[74] A.G. Volkov, D.W. Deamer, D.L. Tanelian, V.S. Markin; *Liquid Interfaces in Chemistry and Biology*; (1998) Wiley Interscience: New York, 136.

[75] T. Kakiuchi, in: A.G. Volkov, D.W. Deamer (Eds.); *Liquid–Liquid Interfaces, Theory and Methods*; (1996) CRC Press: Florida, 1.

[76] Electrochemical Database, École Polytechnique Fédérale de Lausanne; dcwww.epfl.ch/cgi–bin/LE/DB/InterrDB.pl (2005)

[77] A. Sabela, V. Mareček, Z. Samec, R. Fuoco; *Electrochimica Acta*; **37** (1992) 231.

[78] J. Czapkiewicz, B. Czapkiewicz–Tutaj; *J. Chem. Soc Faraday Trans. 1.*, **76** (1980) 1663.

[79] M.H. Abraham, A.F. Danil de Namor; *J. Chem. Soc. Faraday. Trans. 1*; **72** (1976) 955.

[80] P. Vanýsek; *Biomembrane Electrochemistry: Advances in Chemistry Series 235*; **4** (1994) 55.

[81] R.M. Allen, D.E. Williams; *Faraday Discuss.*; **104** (1996) 281.

[82] A.A. Stewart, Y. Shao, C.M. Pereira, H.H. Girault; *J. Electroanal. Chem.*; **305** (1991) 135.

[83] Y. Shao, H.H. Girault; *J. Electroanal. Chem.*; **282** (1990) 59.

[84] A–K. Kontturi, K. Kontturi, L. Murtomäki; *J. Chem. Soc. Faraday Trans.*; **86** (1990) 819.

[85] I. Zagórska, Z. Koczorowski, I. Paleska; *J. Electroanal. Chem.*; **282** (1990) 51.

[86] Z. Samec, V. Mareček, M.P. Colombini; *J. Electroanal. Chem.*; **257** (1988) 147.

[87] (a) L.Q. Hung; *J. Electroanal. Chem.*; **115** (1980) 159.
(b) L.Q. Hung; *J. Electroanal. Chem.*; **149** (1983) 1.

[88] V.S. Markin, A.G. Volkov; *J. Phys. Chem. B*; **108** (2004) 13807.

[89] R.M. Fuoss, K.–L. Hsia; *Proc. Nat. Acad. Sci.*; **57** (1967) 1550.

[90] D.R. Crow; *Principles and Applications of Electrochemistry*: 4th Edition (1994) T.J. Press: Cornwall

[91] P.W. Atkins; *Physical Chemistry*: 6th Edition (1998) Oxford University Press: Oxford

[92] M. Platt, R.A.W. Dryfe; *Phys. Chem. Chem. Phys.*; **7** (2005) 1807.

[93] M. Platt, R.A.W. Dryfe, E.P.L. Roberts; *Electrochim. Acta*; **49** (2004) 3937.

[94] R.A.W. Dryfe, A.O. Simm, B. Kralj; *J. Am. Chem. Soc.*; **125** (2003) 13014.

[95] A. Swami, A. Kumar, M. D'Costa, R. Pasricha, M. Sastry; *J. Mater. Chem.*; **14** (2004) 2696.

[96] R. Knake, A.W. Fahmi, S.A.M. Tofail, J. Clohessy, M. Mihov, V.J. Cunnane; *Langmuir*; **21** (2005) 1001.

[97] I. Turyan, M. Etienne, D. Mandler, W. Schuhmann; *Electroanal.*; **17** (2005) 538.

[98] F. Scholz, U. Hasse; *Electrochem. Comm.*; **7** (2005) 541.

[99] H. Gu, Z. Yang, J. Gao, C.K. Chang, B. Xu; *J. Am. Chem. Soc.*; **127** (2005) 34.

[100] L.Zheng, J. Li; *J. Phys. Chem. B*; **109** (2005) 1108.

[101] L.L. Dai, R. Sharma, C.–Y. Wu; *Langmuir*; **21** (2005) 2641.

[102] O. Balmes, J.–O. Bovin, J.–O. Malm, H. Xu; *Vibr. Spect.*; **37** (2005) 189.

[103] B. Su, J.–P. Abid, D.J. Fermín, H.H. Girault, H. Hoffmannová, P. Krtil, Z. Samec; *J. Am. Chem. Soc.*; **126** (2004) 915.

[104] J. Guo, T. Tokimoto, R.Othman, P.R. Unwin; *Electrochem. Comm.*; **5** (2003) 1005.

[105] A.M. Collins, C. Spickermann, S. Mann; *J. Mater. Chem.*; **13** (2003) 1112.

[106] J. Solla–Gullón, A. Rodes, V. Montiel, A. Aldaz, J. Clavilier; *J. Electroanal. Chem.*; **554–555** (2003) 273.

[107] C. Johans, K. Kontturi, D.J. Schiffrin; *J. Electroanal. Chem.*; **526** (2002) 29.

[108] C. Johans, P. Liljeroth, K. Kontturi; *Phys. Chem. Chem. Phys.*; **4** (2002) 1067.

[109] C. Johans, J. Clohessy, S. Fantini, K. Kontturi, V.J. Cunnane; *Electrochem. Comm.*; **4** (2002) 227.

[110] C. Johans, R. Lahtinen, K. Kontturi, D.J. Schiffrin; *J. Electroanal. Chem.*; **488** (2000) 99.

[111] Y. Cheng, D.J. Schiffrin; *J. Chem. Soc. Faraday Trans.*; **92** (1996) 3865.

[112] D.H. Everett; *Basic Principles of Colloid Science*; (1998) Royal Society of Chemistry Paperbacks: London.

[113] M. Shields, R. Ellis, B.R. Saunders; *Colloid Surface A*; **178** (2001) 265.

[114] M.M. Robins; *Curr. Opin. Colloid Int. Sci.*; **5** (2000) 265.

[115] E. Dickinson, C. Ritzoulis; *J. Colloid Int. Sci.*; **224** (2000) 148.

[116] E. Dickinson, M. Golding, M.J.W. Povey; *J. Colloid Int. Sci.*; **185** (1997) 515.

[117] R. Aveyard, B.P. Binks, J. Esquena, P.D.I. Fletcher; *Langmuir*; **15** (1999) 970.

[118] T. Sakai, K. Kamogawa, F. Harusawa, N. Momozawa, H. Sakai, M. Abe; *Langmuir*; **17** (2001) 255.

[119] T. Sakai, K. Kamogawa, F. Harusawa, N. Momozawa, H. Sakai, M. Abe; *The International Conference on Colloid and Surface Science: Studies in Surface Science and Catalysis*; **132** (2001) 157.

[120] I.B. Ivanov, K.D. Danov, P.A. Kralchevsky; *Colloid Surface A*; **152** (1999) 161.

[121] S. Peach; *Macromolecules*; **31** (1998) 3372

[122] G. Narsimhan, P. Goel; *J. Colloid Int. Sci.*; **238** (2001) 420.

[123] G.A. van Aken, F.D. Zoet; *Langmuir*; **16** (2000) 7131.

[124] J. Bibette, F. Leal Calderon, P. Poulin; *Rep. Prog. Phys.*; **62** (1999) 969.

[125] J. Weiss, D. McClements; *Langmuir*; **16** (2000) 2145.

[126] T. Sakai, K. Kamogawa, K. Nishiyama, H. Sakai, M. Abe; *Langmuir*; **18** (2002) 1985.

[127] A.S. Kabalnov, A.V. Pertzov, E.D. Shchukin; *J. Colloid. Interface. Sci.*; **118** (1987) 590.

[128] B.P. Binks, W–G. Cho, P.D.I. Fletcher, D.N. Petsev; *Langmuir*; **16** (2000) 1025.

[129] M.B.J. Meinders, T. van Vilet; *Adv. Colloid Int. Sci.*; **108–9** (2004) 119.

[130] P. Taylor; *Adv. Colloid Int. Sci.*; **75** (1998) 107.

[131] P. Neogi, G. Narsimhan; *Chem. Eng. Sci.*; **56** (2001) 4225.

[132] M.Y. Koroleva, E.V. Yurtov; *Colloid Journal*; **65** (2003) 40.

[133] E. Dickinson, C. Ritzoulis, Y. Yamamoto, H. Logan; *Colloid Surfaces B*; **12** (1999) 139.

[134] J. Jiao, D.J. Burgess; *J. Colloid Int. Sci.*; **264** (2003) 509.

[135] K.G. Marinova, R.G. Alargova, N.D. Denkov, O.D. Velev, D.N. Petsev, I.B. Ivanov, R.P. Borwankar; *Langmuir*; **12** (1996) 2045.

[136] J. Merikanto, H. Vehkamäki, E. Zapadinsky; *J. Chem. Phys.*; **121** (2004) 914.

[137] M. Hermansson; *Colloid Surface B*; **14** (1999) 105.

[138] M. Salou, B. Siffert, A. Jada; *Colloid Surface A*; **142** (1998) 9.

[139] A.W. Adamson; *Physical Chemistry of Surfaces 5th Edition*; (1990) John Wiley & Sons: USA.

[140] I.D. Charlton, A.P. Doherty; *J. Phys. Chem. B*; **103** (1999) 5081.

[141] R. Xu; *Langmuir*; **14** (1998) 2593.

[142] T.J. Su, Z.F. Cui, R.K. Thomas, R.K. Heenan; *Langmuir*; **14** (1998) 5517.

[143] K. Kamogawa, N. Kuwayama, T. Katagiri, H. Akatsuka, T. Sakai, H. Sakai, M. Abe; *Langmuir*; **19** (2003) 4063.

[144] T. Sakai, Y. Takeda, F. Mafuné, M. Abe, T. Kondow; *J. Phys. Chem. B*; **107** (2003) 2921.

[145] T. Sakai, K. Kamogawa, K.O. Kwon, H. Sakai, M.Abe; *Colloid Polym. Sci.*; **280** (2002) 99.

[146] K. Kamogawa, H. Akatsuka, M. Matsumoto, S. Yokoyama, T. Sakai, H. Sakai, M. Abe; *Colloid. Surf. A*; **180** (2001) 41.

[147] K. Kamogawa, M. Matsumoto, T. Kobayashi, T. Sakai, H. Sakai, M. Abe; *Langmuir*; **15** (1999) 1913.

[148] K. Kamogawa, T. Sakai, N. Momozawa, M. Shimazaki, M. Enomura, H. Sakai, M. Abe; *J. Jpn. Oil. Chem. Soc.*; **47** (1998) 159.

[149] M.J. Francis, R.M. Pashley; *Colloid Surface A*; **260** (2005) 7.

[150] N. Maeda, K.J. Rosenburg, J.N. Israelachvili, R.M. Pashley; *Langmuir*; **20** (2004) 3129.

[151] R.M. Pashley; *J. Phys. Chem. B*; **107** (2003) 1714.

[152] G.R. Burnett, R. Atkin, S. Hicks, J. Eastoe; *Langmuir*; **20** (2004) 5673.

[153] J.K. Beattie, A.M. Djerdjev; *Angew. Chem.*; **43** (2004) 3568.

[154] L. Stryer; *Biochemistry 4th Edition*; (1995) W.H. Freeman & Company: New York.

[155] T. Peters Jr.; *All About Albumin: Biochemistry, Genetics and Medical Applications*; (1996) Academic Press: London.

[156] B.X. Huang, H.–Y. Kim; *Am. Soc. Mass Spectrom.*; **15** (2004) 1237.

[157] X.M. He, D.C. Carter; *Nature*; **358** (1992) 209.

[158] S. Sugio, A. Kashima, S. Mochizuki, M. Noda, K. Kobayashi; *Prot. Eng.*; **12** (1999) 439.

[159] M.L. Ferrer, R. Duchowicz, B. Carrasco, J.G. de la Torre, A.U. Acuña; *Biophysical Journal*; **80** (2001) 2422.

[160] J.R. Lu; *Annu. Rep. Prog. Chem., Sect. C*; **95** (1999) 3.

[161] Y.C. Sasaki, Y. Suzuki, T. Ishibashi; *Science*; **263** (1994) 62.

[162] T.J. Lenk, B.D. Ratner, R.M. Gendreau, K.K. Chittur; *J. Biomed. Mat. Res.*; **23** (1989) 549.

[163] A. Hickel, C.J. Radke, H.W. Blanch; *J. Mol. Cat. B*; **5** (1998) 349.

[164] P.Wilde, A. Mackie, F. Husband, P. Gunning, V. Morris; *Adv. Colloid Int. Sci.*; **108–109** (2004) 63.

[165] V. Rampon, C. Brossard, N. Mouhous–Riou, B. Bosseau, G. Llamas, C. Genot; *Adv. Colloid Int. Sci.*; **108–109** (2004) 87.

[166] G.A. van Aken; *Colloid Surface A*; **213** (2003) 209.

[167] É. Kiss, R. Borbàs; *Colloid Surface B*; **31** (2003) 169.

[168] K.I. Al–Malah, M.O.J. Azzam, R.M. Omari; *Food Hydrocolloids*; **14** (2000) 485.

[169] E. Dickinson; *J. Chem. Soc. Faraday Trans.*; **94** (1998) 1657.

[170] D.G. Dalgleish; *Trends Food Sci. Tech.*; **8** (1997) 1.

[171] D.C. Clark, A.R. Mackie, P.J. Wilde, D.R. Wilson; *Faraday Discuss.*; **98** (1994) 253.

[172] E. Dickinson; *J. Chem. Soc. Faraday Trans.*; **88** (1992) 2973.

[173] E. Dickinson, M.G. Semenova; *J. Chem. Soc. Faraday Trans.*; **88** (1992) 849.

[174] H. Bagger–Jörgensen, U. Olsson, K. Mortensen; *Langmuir*; **13** (1997) 1413.

[175] T.J. Su, J.R. Lu, Z.F. Cui, R.K. Thomas; *J. Membrane Sci.*; **173** (2000) 167.

[176] O. Vidal, M.C. Roberts, F. Boué; *J. Cryst. Growth*; **192** (1998) 271.

[177] R.K. Heenan, J. Penfold, S.M. King; *J. Appl. Cryst.* **30** (1997) 1140.

[178] http://www.isis.rl.ac.uk/largescale/loq/loq.htm

[179] http://www.ill.fr/YellowBook

[180] R.K. Heenan; *The "FISH" Data Fitting program manual*; (1989) Rutherford Appleton Laboratory Report, RAL–89–129.

[181] www.avantilipids.com/Extruder.html

[182] J.W. Lovick, A.A. Mouza, S.V. Paras, G.J. Lye, P. Angeli; *J. Chem. Tech. Biotech.*; **80** (2005) 545.

[183] M.J.H. Simmons, S.H. Zaidi, B.J. Azzopardi; *Opt. Eng.*; **39** (2000) 505.

[184] H. Stephen, T. Stephen; *Solubilities of Inorganic and Organic Compounds Vol. 1*; (1963) Pergamon Press: Oxford.

[185] R.C. MacDonald, R.I. MacDonald, B.Ph.M. Menco, K. Takeshita, N.K. Subbarao, L.–R. Hu; *Biochim. Biophys. Acta*; **1061** (1991) 297.

[186] D.R. Lide; *The CRC Handbook of Chemistry and Physics 81st Edition*; (2000) CRC Press LLC: Florida.

[187] H.–S. Kim; *Bull. Korean Chem. Soc.* **19** (1998) 1347.

[188] R.A. Robinson, R.H. Stokes; *Electrolyte Solutions* (1959) Pitman Press: Bath.

[189] Y. Marcus; *Ion Solvation* (1985) Wiley: Chichester.

[190] J. Wyman, E.N Ingalls; *J. Am. Chem. Soc.* **60** (1938) 1182.

[191] Z.–B. Li, Y.–G. Li, J.–F. Lu; *Ind. Eng. Chem. Res.*; **38** (1999) 1133.

[192] S.M. King, in: R.A. Pethrick, J.V. Dawkins (Eds.); *Modern Techniques for Polymer Characterisation*; (1999) Wiley and Sons Ltd.: Chichester 171.

[193] M. Kotlarchyk, S.H. Chen; *J. Chem. Phys.*; **79** (1983) 2461.

Appendix A: Defined Parameters for the FISH Microemulsion Model used in the SANS Data Analysis

The Microemulsion program, used in FISH to analyse the SANS data, is shown in Figure **A1** and some of the parameters, in bold text, are explained to the right of the model.

```
T  2 P 45 S  3 C 15 N  5
W  1 K  1 IP 0 MS 1 IY 1    0    0 XB 0    0  149  164    7
 2/8/5 solv contrast modified for D11 expt 4/8/5 new slds
 Caruana microemulsion   core(50/50),shell(CM), drop
 1 88  1 SET 1 core     0.000000E+00    0.0
 2 10  1 A              1.822100E+00   -1.0
 3 10  2 R1             1.999305E+04   -2.0   R1 =the radius of the
 4 10  1 B              0.000000E+00   -1.0   drop core.
 5 10  2 R1+R3          1.999405E+04   -1.0
 6 10  1 G (zero)       1.250005E-02   -1.0
 7 10  2 R1+R3+R4       2.002917E+04   -1.0
 8  3 11 BKG SET 1      1.136004E+00    1.0
 9 88  2 SET 2 shell    0.000000E+00    0.0
10 10  1 A              1.822100E+00   -1.0
11 10  2 R1             1.999305E+04   -2.0
12 10  1 F              0.000000E+00   -1.0
13 10  2 R1+R3          1.999405E+04   -1.0   R1+R3 =the radius of
14 10  1 E             -1.836800E+00   -1.0   the core + 1 shell.
15 10  2 R1+R3+R4       2.002917E+04   -1.0
16  3 11 BKG SET 2      8.884135E-01    1.0
17 88  3 SET 3 drop     0.000000E+00    0.0
18 10  1 C             -1.186100E+00   -1.0
19 10  2 R1             2.169491E+03   -2.0
20 10  1 D              0.000000E+00   -1.0
21 10  2 R1+R3          2.170491E+03   -1.0
22 10  1 E             -2.264800E+00   -1.0
23 10  2 R1+R3+R4       2.205611E+03   -1.0   R1+R3+R4 =the radius
24  3 11 BKG SET 3      8.715028E-01    1.0   of the core + 2 shells.
25 88  0 ALL SETS       0.000000E+00    0.0
26  2  1 x CORE/TAIL    0.000000E+00    0.0 } Extent of penetration of
27  2  1 y SOLV/HEAD    0.000000E+00    0.0 } solvents into shells.
28  2  1 R3 TAIL        1.000000E+00    0.0 } Shell thicknesses either
29  2  1 R4 HEAD        3.511931E+01    1.0 } side of the interface.
30  2  1 core (H)sld    1.313900E+00    0.0 } DCE scattering length
31  2  1 core (D) "     4.322100E+00    0.0 } densities.
32  2  1 tail(inner)    2.500000E+00    0.0 } BSA SLD in water and
33  2  1 head(outer)    2.500000E+00    0.0 } DCE.
34  2  1 solv 50/50     2.487500E+00    0.0 }
35  2  1 solv CM        4.336800E+00    0.0 } Aqueous phase SLD.
36  2  1 solv D         4.764800E+00    0.0 }
37  6 11 SCH SCALE      1.104065E-07    1.0   1 x10^-4 times the total
                                              DCE volume fraction.
38  6 12       RBAR     2.169491E+03    1.0   The average core radius.
39  6 13     R-SHIFT    0.000000E+00    0.0
40  6 14 SIG/(RB-R0)    2.982222E-01    1.0   The drop polydispersity.
41 22  1 HS S(Q) VOL    0.000000E+00    0.0
42 22  2 SPH RADIUS     3.000000E+03    0.0
43 15  1 SMEAR          0.000000E+00    0.0
44 15  2 NSIMP          2.100000E+01    0.0
```

```
 45 99  1 SCALE         1.000000E+00     0.0
  1  1 core          CALC 4 BKG 0 POL 7  SSE= 1.066E+03
  2  2 shell         CALC 5 BKG 0 POL 8  SSE= 1.173E+02
  3  3 drop          CALC 6 BKG 0 POL 9  SSE= 2.080E+03
 12   2  26  31  32
1.000E+04 1.104E-07 2.982E-01 2.000E+01 2.000E+04
```

Figure A1: Listing the Microemulsion model parameters used in FISH to analyse the SANS data in Chapter **5**. Some of the parameters, in bold text, have been defined to the right of the model.

The nature of the FISH program meant that different values for the parameters could be entered into the model, and the effect of these could be observed on the data fitting. For the fitting of the D11 SANS data, the values for the SLD of the aqueous and organic phases were calculated and entered manually. These were then set to these values, as were the SLD of the BSA layers either side of the interface. The thickness of the BSA_{DCE} shell was also entered manually and set at 1 Å. This was to reduce the number of unknown parameters being fit when the program was run; i.e. the thickness of the BSA_{aq} shell, the Shultz scale, the drop radius and the drop polydispersity.